Doctoral Dissertation

Galaxy Spectral Energy Distribution Model with the Evolution of Dust Consistent with the Chemical Evolution

ダスト化学進化を取り入れた 銀河スペクトルエネルギー分布モデル

Kazuki Y. NISHIDA
(西田　和樹)

Graduate School of Science,
Nagoya University

Supervisor: Tsutomu T. TAKEUCHI

February 22, 2021

Acknowledgments

I would like to express my gratitude to my supervisor, Tsutomu T. Takeuchi for providing considerable effort. Although I do not know anything about galaxy evolution because I am converted from experimental X-ray astronomy, you lead me toward very interested and suited topics. I greatly enjoyed the research life in Nagoya University.

I want to thank my collaborators, Ryosuke S. Asano and Takuma Nagata. The existence of this thesis is thanks to your establishing the base of this work, and your heritages are helpful for my works. I also thank Akio K. Inoue, your advice and codes are very helpful for solving radiative transfer.

I am deeply grateful to my previous supervisor, Toru Tamagawa. Your teaching how to solve the problem and how to thought the solution become one of my fundamental components.

I would like to thank the colleagues of lab, Chikako Nishihara, Moe Yoda, Kai Kono, Sayaka K. Nagasaki, Shuntaro A. Yoshida, Kiyoaki C. Omori, Suchetha Cooray, Hibiki Shimoyama, Chihiro Kondo, Shi-Wen Yuichi B. Yoshioka, Tae Hojo, and neighbors for discussions in my work and the small talk, which is very important thing for taking my mind off.

In the end, I would like to express the deepest appreciation to my family and wife for helping me for a lot of years and from now on.

Contents

List of Figures

List of Tables

Part I

General Introduction

Chapter 1

Brief review on galaxies and their spectral energy distribution model

A galaxy is a system that consists of stars, gas, dust, and dark matter. In the present-day Universe, more than 2×10^{12} (Conselice et al., 2016) galaxies exist, and the most distant observed galaxy is at the cosmic age of 0.4 billion years (redshift[1] $z = 11.1$: Oesch et al. 2016). The age of the Universe is estimated via observations of the cosmic microwave background, and currently favored value is 13.8 billion years (Alves et al., 2016). Therefore, the galaxies exist almost all over the lifetime of the Universe, so they are a fundamental component to understand the history of the Universe.

A number of physical properties are derived from galaxies. For example, as for the mass, there are total mass (including dark matter), baryon mass, stellar mass, gas mass, metal mass, dust mass, and so on. We can also observe the rotation velocity of a galaxy, which is one of the evidence of the existence of the dark matter (e.g., Rubin et al., 1980). Dark matter is supposed to be a massive particle that does not or only weakly interacts through the electromagnetic force. It is thought to have an important influence on galaxy formation by gravitationally binding stars and gas, but the direct detection of the dark matter particles has not been succeeded yet.

The components of the galaxy, except dark matter, emit photon at various wavelengths, by different physical processes. The distribution of emitted energy per wavelength (or frequency) is called spectral energy distribution (SED). Stars mainly emit photons at the wavelength range from ultraviolet (UV) to near-infrared (NIR). Then, the emission from stars is attenuated by dust grains before reaching us. Dust is a tiny particle with a typical size of 0.1 μm or less in the interstellar medium (ISM), and contains hydrogen, carbon, and silicon as main ingredients. Gas emits a characteristic line spectrum produced from quantum mechanical processes, as well as continuum (e.g., Diaz et al., 1987; Kaufman et al.,

[1] We astronomers use redshift for representing the Universe age and distance. It is defined as $1 + z \equiv \frac{\lambda_1}{\lambda_0}$, where λ_0 is the intrinsic wavelength and λ_1 is the observed wavelength. This effect came from the Universe expansion. When $z = 1$, observed wavelength becomes twice as long.

1999). Dust grains absorb and scatter photons from stars and finally re-emit the energy at a wavelength range from mid-infrared (MIR) to far-infrared (FIR). Another important role of dust is related to the molecular formation. Hirashita & Ferrara (2002) suggested that hydrogen molecules efficiently form on the surface of the grains working as a catalyst. Hydrogen molecules are one of the important ingredients of star formation. Thus, dust grains promote star formation. Furthermore, the collision of dust grain and gas in high-density regions of the ISM greatly contributes to the cooling of gas and also leads to the activation of star formation.

Dust grains are produced in stellar outflows (Draine & Salpeter, 1977). The main sources of dust grains are asymptotic giant branch (AGB) stars and Type II supernovae (SNe II) (e.g., Gehrz, 1989; Nozawa et al., 2003, 2007; Bianchi & Schneider, 2007; Zhukovska et al., 2008). SNe not only produce new dust grains, but also destroy dust grains in the ISM by shocks (Jones et al., 1994, 1996; Nozawa et al., 2003, 2006; Zhukovska et al., 2008; Yamasawa et al., 2011). The grain destruction has also been confirmed by several supernova remnants (SNR) observation (e.g., Borkowski et al., 2006; Arendt et al., 2010). The mass and size distribution of dust grains evolves in ISM due to metal accretion (Zhukovska et al., 2008; Michałowski et al., 2010b; Hirashita & Kuo, 2011; Asano et al., 2013a) and collision between dust grains (Yan et al., 2004; Jones et al., 1996; Hirashita & Yan, 2009; Kuo & Hirashita, 2012). Which process controls the mass of dust varies greatly depending on the age and the environment of the galaxy. In particular, since dust consists of metals, dust evolution is strongly affected by the metallicity of the ISM in a galaxy (Inoue, 2003; Asano et al., 2013a). For example, the SNe II dominates the dust supply in young galaxies, because SNe II has a shorter lifetime (typically 10^6–10^7 yr) than AGB stars (typically 10^8–10^9 yr) (Morgan & Edmunds, 2003; Marchenko, 2006; Dwek et al., 2007; Valiante et al., 2009). In addition, metal accretion process depends on the total surface area of dust grains. Therefore, in order to consider the evolution of dust, it is necessary to consider not only the total mass but also the size distribution. Although dust mass/size evolution have important role in galaxy evolution, some previous SED models (e.g., Silva et al., 1998; Fioc & Rocca-Volmerange, 2019; Boquien et al., 2019) used an empirical recipe of dust based on observations of nearby galaxies. It has been suggested that distant galaxies tend to have a flatter attenuation curve than nearby galaxies (e.g., Maiolino et al., 2004; Gallerani et al., 2010; Hjorth et al., 2013). These flat attenuation curves suggest that the dust mass distribution is dominated by the SNe II of massive star rather than by dust evolution, unlike in nearby galaxies (e.g., Maiolino et al., 2004; Hiraki & Hirak, 2008). On the other hand, recently, some galaxies with a huge mass of dust ($M_{\rm dust} > 10^6 M_\odot$) have been observed in the distant Universe (redshift $z > 6$) (e.g, Watson et al., 2015; Laporte et al., 2017; Tamura et al., 2019). Michałowski et al. (2010a) investigated whether stars supply would be sufficient for dust mass detected in a distant ($5 < z < 6.5$) dust-rich quasi-stellar objects (QSOs). Then a naive application of the currently used models for galaxies with a different dust distribution than nearby galaxies might lead to erroneous results. Notably, since the calculation of distant galaxy SED would be misled by the previous models, an SED model based on the theory of dust evolution is definitely required now, after the advent of ALMA.

Asano et al. (2013a,b, 2014) and Nozawa et al. (2015) constructed a dust evolution model which calculates the chemical evolution and the grain size distribution with galaxy evolution. Galaxy evolution means that the above physical properties evolve with the age of the Universe. There is a cycle in which stars birth in the gas cloud, stars form heavier elements and produce that into the ISM and reforming stars are promoted by increasing metallicity in the ISM. In this cycle, the chemical composition evolves with the age of a galaxy: this is referred to as the chemical evolution. The dust model indicated that there is a well-defined moment at which the dust-to-gas mass ratio suddenly rises. It implies that if we use such an empirical dust mass distribution model for calculating distant galaxy SED, the prediction might be an overestimate for the dust mass.

In our SED model, the emission from the stars is calculated by stellar population synthesis (SPS) method with a simple stellar population (SSP). An SSP represents the time variation of the SED of a single contemporaneous stellar population with a single metallicity and abundance pattern. Stellar emission can be obtained by weighting the SED obtained by SSP with the star formation rate (SFR) and the metallicity evolution. We adopted PÉGASE (Fioc & Rocca-Volmerange, 1997), which uses an SPS method for calculating the emission of stellar component. In our model, dust attenuation is calculated using radiative transfer, which assumes a one-dimensional plain-parallel disk-like galaxy with mega-grain approximation (MGA: Varosi & Dwek 1999; Inoue 2005). In order to speed up the calculation, MGA treats the region with high dust density as one huge dust grain (mega-grain). We use the dust size distribution calculated by considering the dust evolution consistent with chemical evolution proposed by Asano et al. (2013a,b, 2014); Nozawa et al. (2015). This is the most substantial feature in our model. Emission from dust grain is calculated taking into account the stochastic heating of grains. Large size dust grains (radius of $a > 200$ Å) are in temperature equilibrium with the radiation field in the galaxy, and they emit FIR by gray body radiation. On the other hand, very small size dust grains (VSGs; 10 Å$< a < 200$ Å) cannot be in equilibrium with the ambient radiation field, due to its low heat capacity (Desert et al., 1990; Dwek et al., 1997; Draine & Li, 2001). The temperature probability distribution of VSGs is very broad, and they emit photons with a wide range of energy. To calculate their temperature probability distribution, we adopted a Monte Carlo simulation. Then, the radiation is calculated from the distribution considering the energy balance. The final SED is constructed by superposing the above emission from stars, dust attenuation, and dust radiation. Wavelength range of our model is 912 Å–99.2 cm, and we do not include the synchrotron radiation and free-free emission at radio wavelengths. This model can predict the amount and emission of dust in a theoretical manner, not only in nearby galaxies but also in distant galaxies.

This thesis is organized as follows. Chapter 2 introduces the basic properties of each component of a galaxy (star, gas, dust) and its effect on galaxy evolution. In Chapter 3, we explain what kind of radiation each component emits by what kind of physical process. Then we give an overview of the present SED models. Chapter 4 gives a detailed explanation of the dust evolution used in our model. Chapter 5 describes the construction of our SED model by dividing it into the

components of star, dust attenuation, and dust emission. In Chapter 6, we show the results of our SED model. Chapter 7 shows the effect of each ingredient for our model and comparison our result with GRASIL and observation data. Finally, Chapter 8 is devoted to the conclusion and summary of this thesis.

Chapter 2

Components in a galaxy

A galaxy is an astronomical object which contains stars, gas, dust and dark matter which are bound by gravitation. The term "galaxy evolution" means that a galaxy changes its mass, shape, color, etc. over time. Since the timescale of the galaxy evolution is very long (> 100 Myr), it is impossible to observe galaxy evolution by continuing to observe individual galaxies. However, since galaxies exist everywhere in place and time in the Universe, it is possible to assume the evolution of galaxies by observing a large number of galaxies. After the Big Bang, the Universe was very homogeneous and contained a large amount of hydrogen (H: 75 %), helium (^{4}He: 25 %), and dark matter, and a tiny amount of lithium (^{7}Li), deuterium (^{2}D), ^{3}He, and other metals (e.g., Mo et al., 2010). Most of the heavy metals were synthesized in the stars. It is considered that the galaxy was formed by the growth of initial fluctuations of the Universe, where gas was condensed together with dark matter. Because each element of a galaxy evolves with interaction of each component, it is necessary to consider the evolution of each component at the same time in order to consider the global galaxy evolution. In this Chapter, we introduce the evolution of each component of a galaxy.

2.1 Star formation in galaxy

Star formation depends on the galaxy morphology[1] and evolutionary stages of the galaxy. It has been suggested that radiative cooling of hydrogen molecules plays an important role in the formation of the first star (Omukai & Nishi, 1998; Abel et al., 2002; Yoshida et al., 2008), called Population III (Pop III) stars. According to theoretical studies, these Pop III stars were very heavy, having 100 $M_\odot$ or more (Bromm et al., 1999, 2002; Abel et al., 2002; Yoshida et al., 2008; Ohkubo et al., 2009), while nearby galaxies have the initial mass functions (IMFs) with a peak of 0.3 $M_\odot$ (Kroupa, 2001; Bastian et al., 2010). Pop III is formed in a low metallicity environment where only the elements created by the Big Bang are present, so it cannot be cooled by metals as the star formation in the nearby galaxies. Pop III

[1]Since the galaxies are thought to have the different properties of each morphology, they are often classified by morphology. There are several classification methods, for example, Hubble sequence(Hubble, 1926), de Vaucouleurs system(de Vaucouleurs, 1959) and so on.

star is predicted by theory, but it has not been directly observed yet. The metals synthesized inside Pop III stars are distributed by supernova (SN) explosions into interstellar medium (ISM), and the next generation of stars (called population II stars: Pop II stars) will be formed (Nomoto et al., 2006). Pop II star is a metal-poor star and contains more alpha elements, which is formed by alpha process (O, Si Ne, and so on), than iron (Wolfe et al., 2005). This is because the alpha elements are produced by Type II supernovae (SNe II), which is common in the times when pop II stars are formed. The distribution of these first star-dusts by the explosion of Pop III stars change the tendency of star formation from dominated by massive stars to dominated by stars with masses $\sim M_{\odot}$(Schneider et al., 2003, 2006).

The explosions of Pop III stars also provide the first dust. The presence of dust grain dramatically enhances the formation of hydrogen molecules (see §2.4). Another important effect of dust is cooling due to collision between dust grain and gas (Ostriker & Silk, 1973; Hollenbach & Tielens, 1999; Omukai et al., 2010). This cooling effect is noticeable in environments where dust and gas collision frequently. When there is no external background radiation, the cooling rate by dust is expressed as $\Lambda_{\rm dust} \propto Z n_{\rm H} T^{3/2}$ (Hollenbach & McKee, 1979; Omukai et al., 2010). Where Z is the metallicity, $n_{\rm H}$ is the mean hydrogen density, and T is the temperature. On the other hand, compression heating due to collapse is proportional to $n_{\rm H}^{1/2} T$, so cooling becomes dominant as the density increases (Omukai et al., 2010). Such dust grain cooling cause to fragmentation of the star forming clouds and leads to the formation of low-mass stars in low-metallicity environment (Whitworth et al., 1998; Omukai et al., 2010; Schneider et al., 2012). This effect has a significant importance on the PopIII/II transition.

Stars like asymptotic giant branch (AGB) produce metals, and release the metals and dust grains into ISM by stellar winds. After the death of stars, dust grains and metals are also released by SNe (e.g., Todini & Ferrara, 2001; Nozawa et al., 2003, 2007; Schneider et al., 2004). Dust is also destroyed by SN shocks (Jones et al., 1994, 1996; McKee, 1989a; Nozawa et al., 2007). The main production source of dust is thought to be AGB stars and SNe II. Metals and dust grains in the ISM are also captured into next-generation stars as star-forming materials. Furthermore, the number, mass, and metallicity of the stars formed are strongly dependent on the abundance of dust and metals in the ISM. In other words, understanding star formation leads to understanding the evolution of galaxies.

2.1.1 Star formation rate

The number of stars formed in the mass interval m, $m + {\rm d}m$ and in the time interval t, $t + {\rm d}t$ is called the birthrate function

$$B(m, t) = \phi(m) {\rm SFR}(t) \, {\rm d}m {\rm d}t. \tag{2.1}$$

This function is separated in two independent part: the initial mass function (IMF) $\phi(M)$ and the star formation rate (SFR) SFR(t). The precision of IMF is introduced in §2.1.2. The SFR is an important physical property in the galaxy. This represents the rate of formed star per year (unit in $M_{\odot}\,{\rm yr}^{-1}$). The SFR

takes various values depending on the morphology of the galaxy, the surrounding environment, and the location in the galaxy. The SFR is particularly strongly dependent on the amount of cold molecular gas. Schmidt (1959) suggests that SFR is proportional to gas density to a power n. This relation called the Schmidt law and Kennicutt (1998) confirmed it by compiling observational data of several galaxies (shown in Figure 2.1). The power n is calculated by Kennicutt (1998)

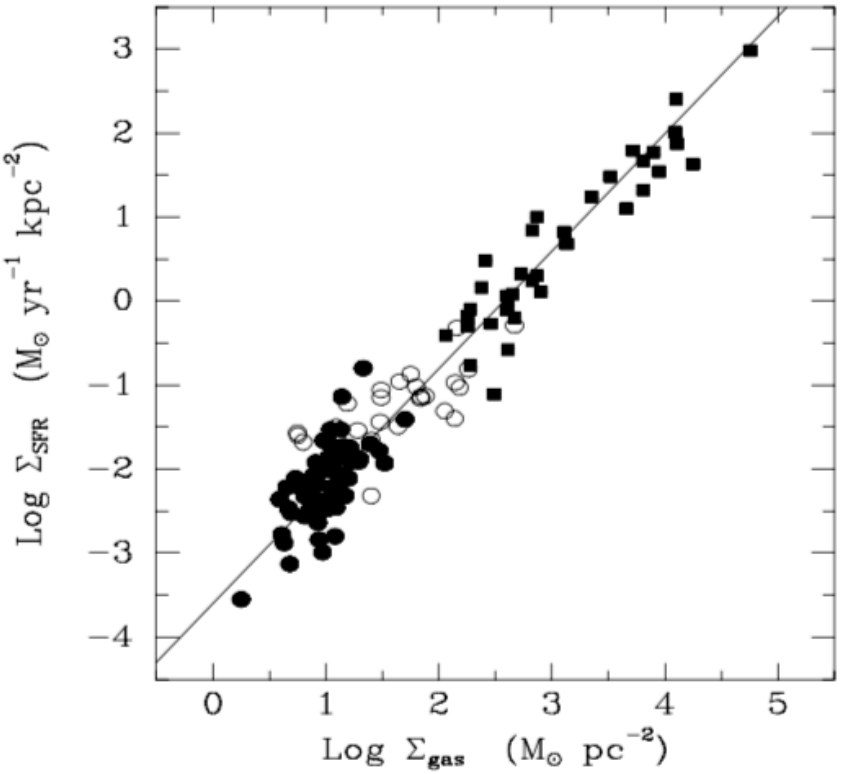

Figure 2.1: The relation between average molecule gas surface density to average star formation rate surface density in galaxies. This relation is called Schmidt low. Credit: Kennicutt (1998)

.

as 1.4. When $n = 1$, it means that star formation is dominated by gravitational instability, and $n = 2$ means that SFR is proportional to the square of gas number density, that is, gas cloud collision forms stars. The Kennicutt (1998) result ($n = 1.4$) lies just in the middle of 1 and 2. Owning to Schmidt low, we can derive the SFR by observation of gas density.

2.1.2 Initial mass function

The IMF $\phi(m)$ is the empirical function expressing how many stars are born in each mass bin. The number of stars formed in the mass interval m, $m + \mathrm{d}m$ is defined as

$$N_M \, \mathrm{d}m = \Delta S \phi(m) \, \mathrm{d}m. \tag{2.2}$$

Where ΔS is the total mass of converted from molecular gas to star. The IMF is normalized by

$$\int_{m_{\rm min}}^{m_{\rm max}} \phi(m) m \, {\rm d}m = 1 M_{\odot}, \tag{2.3}$$

where $m_{\rm max}$ and $m_{\rm min}$ is the maximum and minimum cut-off stellar mass, respectively. There are a lot of works that formulate the IMF for decades (e.g., Salpeter, 1955; Miller & Scalo, 1979; Scalo, 1986, 1998; Kroupa, 2001; Chabrier, 2001). In generally, IMF is represented as a power-law:

$$\phi(m) = A m^{-(1+x)}. \tag{2.4}$$

Salpeter (1955) derived first IMF by fitting in the observation data which range in stellar mass 0.3–15 $M_{\odot}$,

$$\phi(m) \propto m^{-2.35}. \tag{2.5}$$

Thanks to the advance in observation technology, it is understood that piece-wise power laws could express the IMF well. For example, Kroupa (2001) suggested

$$\phi(m) \propto m^{-2.3} \ (0.5 \ M_{\odot} < m < 100 \ M_{\odot}), \tag{2.6}$$
$$\phi(m) \propto m^{-1.3} \ (0.1 \ M_{\odot} < m < 0.5 \ M_{\odot}). \tag{2.7}$$

Figure 2.2 shows a comparison of several IMFs (Baldry & Glazebrook, 2003). It is known from nearby galaxy observation that different molecular cloud have the same IMF, in spite of the difference of physical properties and composition of each molecular cloud (Scalo, 1986, 1998; Kroupa, 2001; Chabrier, 2003). This problem is still debated.

2.2 Stellar evolution

Through the galaxy evolution, star formation is the fundamental process, and stars are the most dominated source of energy in galaxy SED. From ultraviolet (UV) to near-infrared (NIR) wavelength range photons are mainly emitted by stars. This wavelength range is strong affected from absorption and scattering by dust grains in ISM. Dust grains are formed by AGB stars, SNe, red supergiants, novae, Wolf-Rayet stars, and so on (Gehrz, 1989). AGB stars and SNe II, the evolutionary stages of the star (see 2.2.5), are the main production source of dust grain and heaver element. In young galaxies, SNe is considered to be a particularly important source of dust (Morgan & Edmunds, 2003; Maiolino et al., 2004; Dwek et al., 2007). This is noticeable when it takes 1 Gyr to evolve into an AGB star, but the age of the universe is shorter than that (Valiante et al., 2009). As mentioned above, to understand the evolution of dust, we need to understand the evolution of stars.

2.2.1 Molecular cloud

Molecular cloud (MC) is a cold ($\sim$ 10 K) and high density ($n[{\rm H_2}] > 10^2$–10^3 cm^{-3}) astronomical the object. It contains a lot of dust and attenuates background

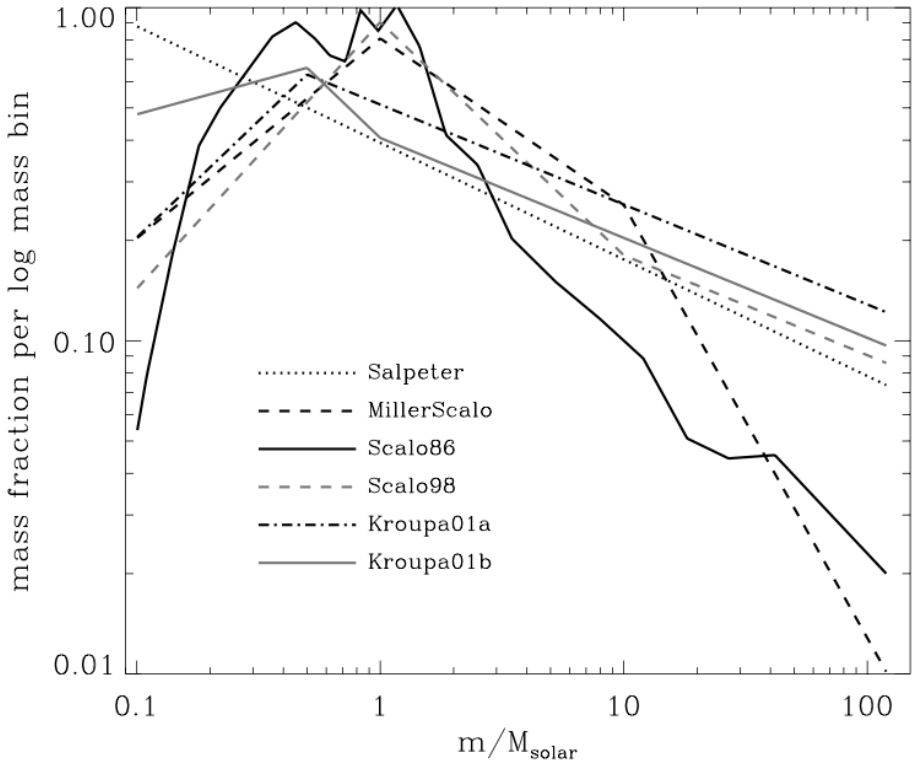

Figure 2.2: The comparison of IMF. Mass fraction versus mass for the Salpeter (1955) IMF, the Miller & Scalo (1979) IMF, the Scalo (1986, 1998) IMFs, the Kroupa (2001) IMFs. All IMFs assume to be valid from 0.1 to 120 $M_{\odot}$. Credit: Baldry & Glazebrook (2003)

.

UV and optical. The main component of MC is hydrogen molecules (H_2), so it dose not have electric dipole moment, thus it can not radiate the rotational line spectrum. Therefore, it is usually used for observing MC the rotational line of carbon monoxide molecules (CO) because CO is the second large amount following H_2. MC is occupied 99 % by gas and the rest is dust grains. Most of hydrogen in MC exists in the molecular (H_2) state and it is thought that all star formation takes place in this region. In our Galaxy, MC is mainly in the spiral arm (Dame et al., 1987).

The high density region in MC is called 'clump' and more denser region (n[$H_2 >$ 10^4–10^6 cm^{-3}]) is called 'molecular cloud core' (e.g., Fukui & Kawamura, 2010). Clumps often include molecular cloud cores. It is thought that the stars are formed by the molecular cloud core. The dense region such as the molecular cloud core is collapsed by self-gravitation. Considering isothermal and the uniform density ρ_0 sphere cloud. When a particle with mass m is located on radius r, the equation of motion of free fall is represented as

$$m\frac{\mathrm{d}^2 r}{\mathrm{d}t^2} = -G\frac{M_{\mathrm{R}}m}{r^2}, \tag{2.8}$$

where G is gravitational constant, and $M_{\rm R}$ is the sphere mass with radius R:

$$M_{\rm R} = \frac{4}{3}\pi R^3 \rho_0. \tag{2.9}$$

Multiply the both side of Equation (2.8) by $\frac{\mathrm{d}r}{\mathrm{d}t}$ and integrate by time t,

$$\int_0^t \frac{\mathrm{d}r}{\mathrm{d}t}\left(\frac{\mathrm{d}r}{\mathrm{d}t}\right)' \mathrm{d}t = -\frac{4}{3}\pi\rho_0 G R^3 \int_0^t \frac{1}{r^2}\mathrm{d}r, \tag{2.10}$$

using initial condition $r = R$ and $\frac{\mathrm{d}r}{\mathrm{d}t} = 0$ at $t = 0$,

$$\left[\frac{1}{2}\left(\frac{\mathrm{d}r}{\mathrm{d}t}\right)^2\right]_0^t = -\frac{4}{3}\pi\rho_0 G R^3 \left[-\frac{1}{r}\right]_{R(t=0)}^{r(t=t)}, \tag{2.11}$$

$$\frac{1}{2}\left(\frac{\mathrm{d}r}{\mathrm{d}t}\right)^2 |_{t=t} = \frac{4}{3}\pi\rho_0 G R^2 \left(\frac{R}{r} - 1\right). \tag{2.12}$$

When considering the contraction, the right hand side of Equation (2.12) takes a positive value. Thus, Equation (2.12) becomes

$$\frac{\mathrm{d}r}{\mathrm{d}t} = \sqrt{\frac{8}{3}\pi G\rho_0 R^2 \left(\frac{R}{r} - 1\right)}. \tag{2.13}$$

Apply $\frac{r}{R} = \cos^2\beta$ to the left hand side of Equation (2.13),

$$\frac{\mathrm{d}r}{\mathrm{d}t} = R \cdot 2\cos\beta\sin\beta \cdot \frac{\mathrm{d}\beta}{\mathrm{d}t}, \tag{2.14}$$

the right hand side of Equation (2.13) is calculated

$$\sqrt{\frac{8}{3}\pi G\rho_0 R^2 \left(\frac{R}{r} - 1\right)} = \sqrt{\frac{8}{3}\pi G\rho_0} R\tan\beta. \tag{2.15}$$

From combining Equation (2.14) with (2.15),

$$\int (\cos 2\beta + 1)\mathrm{d}\beta = \int \sqrt{\frac{8\pi G\rho_0}{3}}\mathrm{d}t, \tag{2.16}$$

$$\frac{1}{2}\sin 2\beta + \beta = \sqrt{\frac{8\pi G\rho_0}{3}} \cdot t + C. \tag{2.17}$$

Where C is the constant of integration. Because of the initial condition $r = R$ at $t = 0$, $C = 0$, Equation (2.17) becomes

$$\frac{1}{2}\sin 2\beta + \beta = \sqrt{\frac{8\pi G\rho_0}{3}} \cdot t. \tag{2.18}$$

When gas cloud collapsed, the particle with mass m reach to $r = 0$ and it correspond to $\beta = 1/2$. Thus, the free-fall time $t_{\rm ff}$ is obtained substituting $\beta = \pi/2$ for Equation (2.18),

$$t_{\rm ff} = \sqrt{\frac{3\pi}{32 G\rho_0}}. \tag{2.19}$$

Equation (2.19) shows that free-fall time does not depend on an initial radius R (Ward-Thompson & Whitworth, 2011). When initial number density $\rho_0 = 100\,\mathrm{cm}^{-3}$, free-fall time is $t_{\rm ff} \simeq 3.6 \times 10^6\,\mathrm{yr}$.

2.2.2 Protostar formation

Density fluctuation in the cloud cause to be collapsed by self-gravitation. When the density of core increase to 10^{11} cm^{-3} by collapse, the cooling efficiency of gas is decreased. The gases become an optically thick state, and the temperature rapidly increases. This state of the core is called the first core. When the first core is constructed, the mass of the first core is very small ($\approx 10^{-2}\ M_{\odot}$) and then the gas surrounding cloud is fall to the first core. The first core temperature is 1,000 K and the radius is about 1 AU. When the temperature becomes more than 2,000 K, hydrogen molecules begin ionizing and then continues to collapse with decreasing pressure. As collapsed continues, hydrogen is fully ionized, this state is called the second core or the protostar. The core temperature of protostar is 4,000 K, the number density is 10^{16} cm^{-3}, the radius is 0.01 AU and the mass is 0.01 $M_{\odot}$.

The gas accretion to the protostar is continues until the mass increase to about 1 $M_{\odot}$. The mechanism of that accretion stoping is discussing.

2.2.3 Pre-main sequence star

After mass accretion, stars begin releasing gravitational energy. This contraction keeps thermodynamic equilibrium and it is called pre-main sequence contraction. When the stellar radius decrease until 1 $M_{\odot}$, the core temperature increase to 1.5×10^7 K, hydrogen-burning is start.

We show the evolutionary tacks of pre-main sequence in Figure 2.3. This figure is called the Hertzsprung-Russell diagram (HR diagram; Russell, 1914). In small star about 1 $M_{\odot}$, the evolutionary tracks have two different slopes. The first slope is along Hayashi track (Hayashi, 1961, 1966), in this phase, energy is transported by convection. After contraction, radiation dominates the transport of energy, this phase is shown in the second slope, it is parallel to the horizontal axis and it is called Henyey track (Henyey et al., 1955). The stars, larger than 2 $M_{\odot}$, do not pass Hayashi track, and its reach to the main sequence with keeping radiative equilibrium.

2.2.4 Main sequence

The main sequence indicates the stars which are burning hydrogen in the core. Stars stay almost all lifetime in the main sequence. Figure 2.4 shows the HR diagram of main sequence. From this figure, the process of burning hydrogen is different from each progenitor mass of star. The process that the core of less than 1.5 $M_{\odot}$ stars are called proton-proton chain (p–p chain) and CNO cycle occurs in the core of more heavy stars.

proton-proton chain

The first step, two protons (p) form a deuterium (d) and emit a positron (e^+) and a neutrino (ν_e),

$$p + p \rightarrow d + e^+ + \nu_e. \tag{2.20}$$

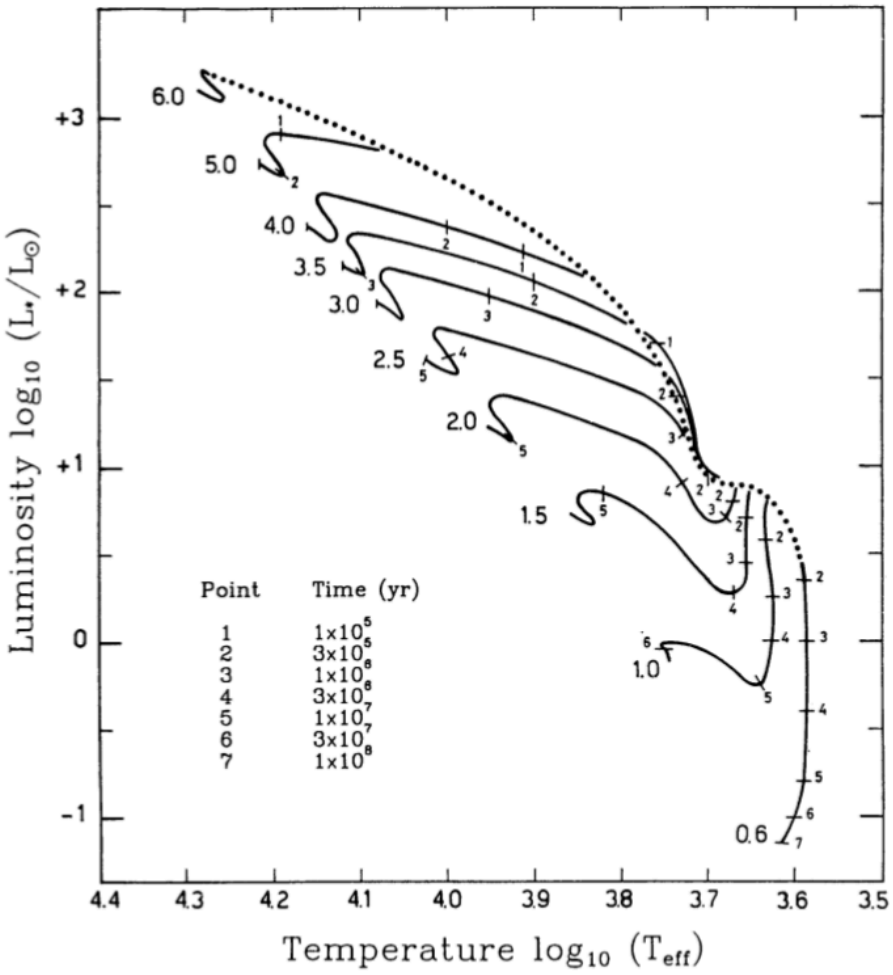

Figure 2.3: The evolutionary tracks of pre-main sequence in the H-R diagram from 0.6 $M_\odot$ to 6.0 $M_\odot$. The label of each track indicates the corresponding mass in solar units. Tick marks represent the evolutionary time as given in the table. The start point is theoretically assuming the birth line (dotted curve). The endpoint of solid lines corresponds to the zero-age main sequence (ZAMS), where the first equilibrium point of hydrogen burning energy and radiation. Credit:Palla & Stahler (1993)

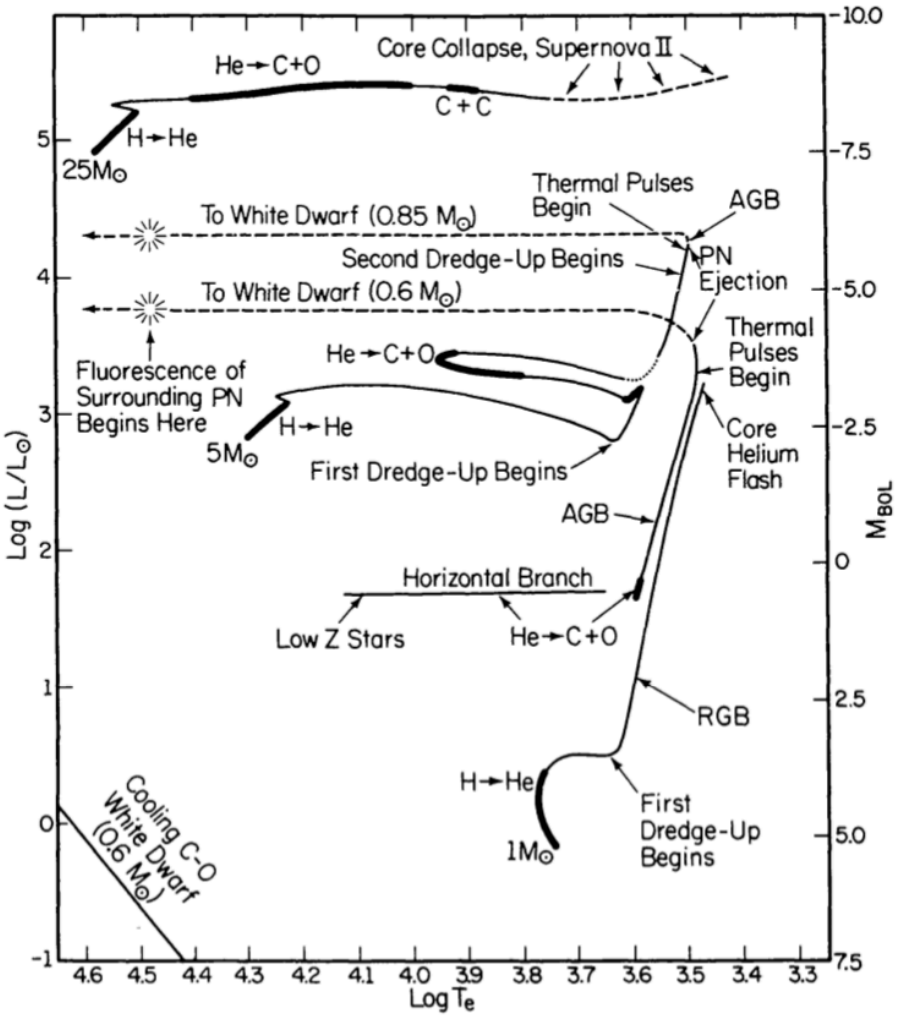

Figure 2.4: A theoretical HR diagram after the main sequence. Credit:Iben (1985)

This step proceeds very slowly, and thus it limits the speed of the p-p chain. The deuterium produced by Equation (2.20) is combined with proton,

$$\mathrm{d} + \mathrm{p} \rightarrow {}^{3}_{2}\mathrm{He} + \gamma. \tag{2.21}$$

The processes in which helium atoms ${}^{4}_{2}\mathrm{He}$ are formed from hydrogen atoms, are three different routes. Its are called p–p I, p–p II, p–p III branch, respectively. The p–p I branch is

$${}^{3}_{2}\mathrm{He} + {}^{3}_{2}\mathrm{He} \rightarrow {}^{4}_{2}\mathrm{He} + \mathrm{p} + \mathrm{p}. \tag{2.22}$$

This process is the main reaction of hydrogen burning in the stellar core. The p–p I branch dominates in the low-temperature environment (8×10^{6}–10^{7} K). In more high temperature (1.4–2.3 $\times 10^{7}$ K) region, the p–p II branch tends to occur and it is represented as

$${}^{3}_{2}\mathrm{He} + {}^{4}_{2}\mathrm{He} \rightarrow {}^{7}_{4}\mathrm{Be} + \gamma, \tag{2.23}$$

$${}^{7}_{4}\mathrm{Be} + \mathrm{e}^{-} \rightarrow {}^{7}_{3}\mathrm{Li} + \nu_{\mathrm{e}}, \tag{2.24}$$

$${}^{7}_{3}\mathrm{Li} + \mathrm{p} \rightarrow 2{}^{4}_{2}\mathrm{He}, \tag{2.25}$$

and even more high temperature ($< 2.3 \times 10^{7}$ K) region cause proton chaptered by ${}^{7}_{4}\mathrm{Be}$,

$${}^{3}_{2}\mathrm{He} + {}^{4}_{2}\mathrm{He} \rightarrow {}^{7}_{4}\mathrm{Be} + \gamma, \tag{2.26}$$

$${}^{7}_{4}\mathrm{Be} + \mathrm{p} \rightarrow {}^{8}_{5}\mathrm{B} + \gamma, \tag{2.27}$$

$${}^{8}_{5}\mathrm{B} \rightarrow {}^{8}_{4}\mathrm{Be} + \mathrm{e}^{+} + \nu_{\mathrm{e}}, \tag{2.28}$$

$${}^{8}_{4}\mathrm{Be} \rightarrow 2{}^{4}_{2}\mathrm{He}, \tag{2.29}$$

this is the p–p III branch.

Neutrinos which are emitted in p–p chains have direct information on the stellar core because the reaction rate of neutrino is very low. Thus, observing neutrino is important for inspecting the stellar energy source.

CNO cycle

If stars contain heavy elements like carbon, nitrogen, and oxygen, the reaction which form helium atoms (${}^{4}_{2}\mathrm{He}$) through positron capture and β^{+} decay, could occur with high temperature (1.8×10^{7} K). This reaction cycle is called CNO cycle. In massive stars ($M > 1.5 M_{\odot}$), the CNO cycle is the main reaction for forming helium atoms. The CNO cycle require higher temperature because it concerns heavier elements, and it is represented as

$${}^{12}_{6}\mathrm{C} + \mathrm{p} \rightarrow {}^{13}_{7}\mathrm{N} + \gamma, \tag{2.30}$$

$${}^{13}_{7}\mathrm{N} \rightarrow {}^{13}_{6}\mathrm{C} + \mathrm{e}^{+} + \nu_{\mathrm{e}}, \tag{2.31}$$

$${}^{13}_{6}\mathrm{C} + \mathrm{p} \rightarrow {}^{14}_{7}\mathrm{N} + \gamma, \tag{2.32}$$

$${}^{14}_{7}\mathrm{N} + \mathrm{p} \rightarrow {}^{15}_{8}\mathrm{O} + \gamma, \tag{2.33}$$

$${}^{15}_{8}\mathrm{O} \rightarrow {}^{15}_{7}\mathrm{N} + \mathrm{e}^{+} + \nu_{\mathrm{e}}, \tag{2.34}$$

$${}^{15}_{7}\mathrm{N} + \mathrm{p} \rightarrow {}^{12}_{6}\mathrm{C} + {}^{4}_{2}\mathrm{He}. \tag{2.35}$$

In this cycle, ${}^{12}_{6}\mathrm{C}$ plays only a catalyst, helium atom is formed by four protons. Equation (2.34) is the bottleneck of the CNO cycle. When more higher temperature, Equation (2.35) branches to

$$
\begin{aligned}
{}^{15}_{7}\mathrm{N} + \mathrm{p} &\rightarrow {}^{16}_{8}\mathrm{O} + \gamma, && (2.36)\\
{}^{16}_{8}\mathrm{O} + \mathrm{p} &\rightarrow {}^{17}_{9}\mathrm{F} + \gamma, && (2.37)\\
{}^{17}_{9}\mathrm{F} &\rightarrow {}^{17}_{8}\mathrm{O} + \mathrm{e}^{+} + \nu_{\mathrm{e}}, && (2.38)\\
{}^{17}_{8}\mathrm{O} + \mathrm{p} &\rightarrow {}^{14}_{7}\mathrm{N} + {}^{4}_{2}\mathrm{He}. && (2.39)
\end{aligned}
$$

The ratio of the reactions of the p–p chain and CNO cycle depend on the temperature of stars, the equilibrium states in cores are different from each other. Because the CNO cycle has a strong dependence on temperature, a temperature gradient occurs easily in cores, convective equilibrium is generated. On the other hand, the p–p chain has a weak dependence on temperature, it makes it possible to radiative equilibrium. Above differences of equilibrium cause different stellar evolution.

The lifetime of main sequence stars τ are determined by which how long time stars can burn the hydrogen. It is represented as

$$
\tau = \frac{\epsilon q M c^2}{L}, \tag{2.40}
$$

where M is the total stellar mass, q is the mass ratio of burning hydrogen with total stellar mass (~ 0.1), ϵ is the energy efficiency of burning hydrogen per one hydrogen atom ($\sim 7 \times 10^{-3}$), and L is the luminosity of the star. For the reference, from Figure 2.4, when a star increases mass from 5 $M_{\odot}$ to $25 M_{\odot}$, the luminosity increases three order. Thus, from Equation (2.40), more massive stars have a shorter lifetime. We show the theoretical model in Figure 2.5. As in the figure, the massive stellar has almost constant lifetime due to Eddington limit.

2.2.5 After main sequence

In this subsection, we explain how to evolve the after main sequence stars. We show the theoretical H-R diagram of various mass stars in Figure 2.6. The curve from the upper left to lower right represents main sequence stars. When the hydrogen burning finishes, the star evolves to after main sequence. The evolutionary tracks and the time depart from main sequence are depend on the mass of stars.

$0.1 M_{\odot} < M < 0.8 M_{\odot}$

This small mass range of stars continue burning hydrogen by the p–p chain, and its lifetimes are longer than the age of the Universe so its can not evolve to after main sequence.

$0.8 M_{\odot} < M < 2 M_{\odot}$

This range of stars finally evolve to the white dwarf, and the maximum mass ($2 M_{\odot}$) determines which helium flash occurs or not. In the main sequence phase,

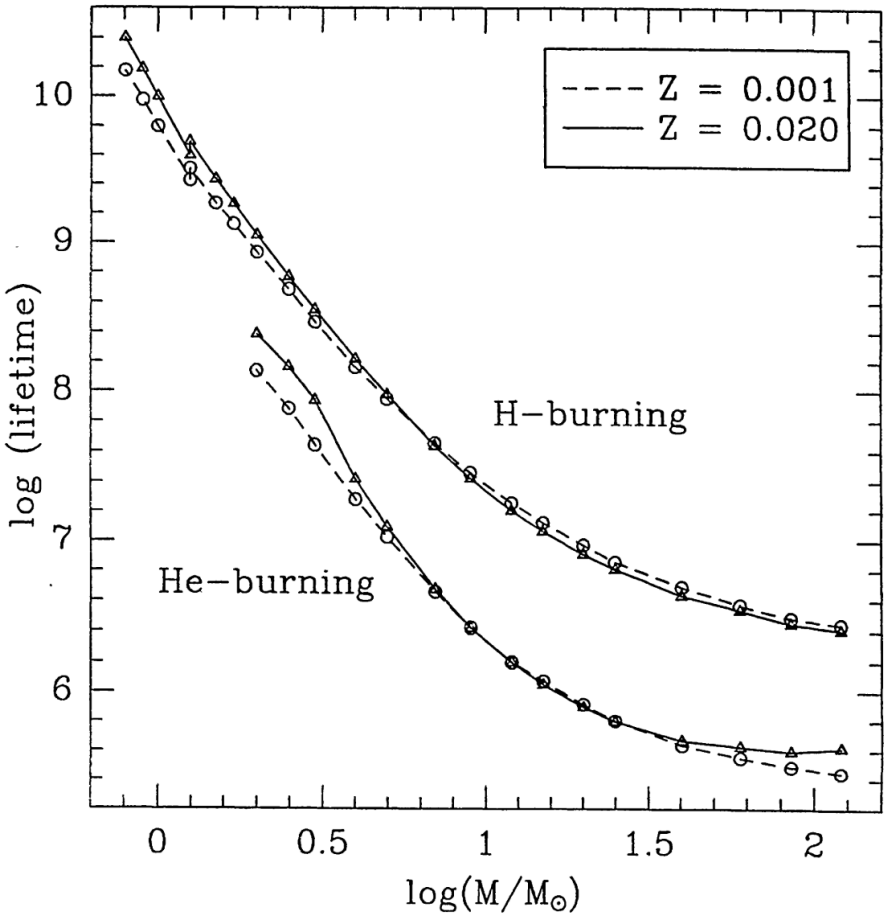

Figure 2.5: The lifetime of main sequence (hydrogen-burning) and helium burning. The solid lines represent metallicity $Z = 0.020$ and dotted lines represent $Z = 0.001$. Credit:Schaller et al. (1992)

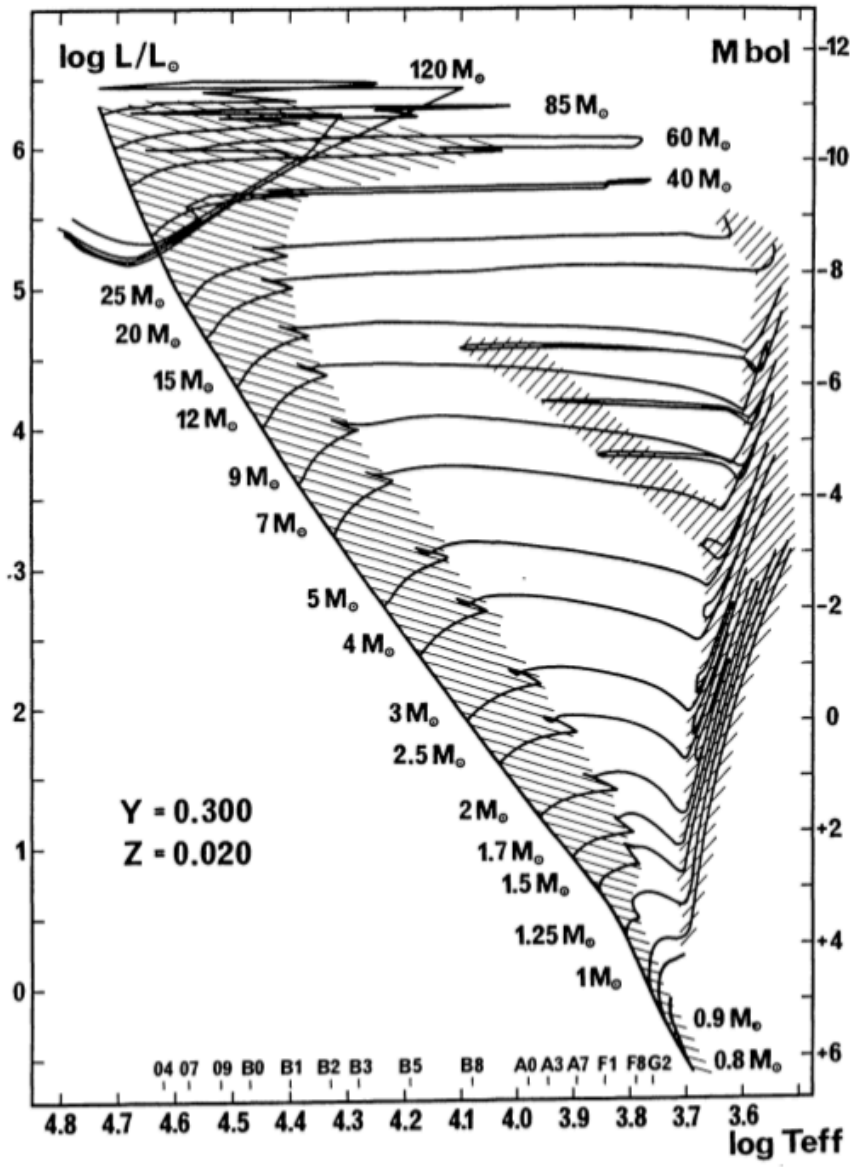

Figure 2.6: The evolutionary tracks of various mass stars in the H-R diagram. The meshed areas represent a lot of stars observed for evolution speeds are slow. The curve from the upper left to lower right is the main sequence.

stars generate the helium core with decreasing hydrogen. The radius of stars are gradually increasing and moves to the right size on the HR diagram. This reason differs from the mechanism of helium burning, the p–p chain or the CNO cycle (see the case $2M_{\odot} < M < 8M_{\odot}$). When the p–p chain occurs in the core, convection does not occur and hydrogen burning gradually occurs from the center of the core. The produced helium core is dense and its pressure is independent of the temperature. Thus, the stars sustain self-gravitation due to the gradient of pressure derived from the gradient of density. This core can regard as the polytrope sphere of index $n = 1.5$, the radius of the core is proportional to the power of 1/3 mass. As a result, hydrogen-burning is more activate, and the outer layer is expanded.

The larger the outer layer, the larger the temperature gradient and the more efficient convection of energy. As a result, the star evolves with increasing luminosity without expansion. This evolutionary phase is called the red giant branch. When the mass of helium core increase to 0.46 $M_{\odot}$, the helium-burning begins in the core, it is called the triple-alpha process. Due to the electron degeneracy of the helium core, the temperature increases with expansion. The temperature of the core increases more and more, causing helium flash. After the helium flash, the helium core expands and the star becomes a stable phase (horizontal branch).

By the helium burning, carbon and oxygen are produced in the stellar core. They have both a helium-burning core and a hydrogen-burning core, and this phase is called the Asymptotic Giant Branch (AGB). The energy of hydrogen burning is accumulated in the helium core, and eventually the burning of the helium shell goes into a runaway state. This state generates convection in the helium shell. The convection mixes carbon and oxygen, and heavier elements are synthesized by the s -process in the helium shell. As a result, the elements are pumped-up to the stellar surface, this process is called third dredge-up. The number of times the third dredge-up occurs depends on the mass of star (e.g., Ferrarotti & Gail, 2006). It is important for our model that the dust grains components depend on this number. AGB stars release a large amount of element into the ISM by stellar winds. Finally, AGB stars blow off the surrounding gas by the radiative pressure, they become planetary nebulae and evolve to the white dwarfs.

$2M_{\odot} < M < 8M_{\odot}$

In the cores of stars in this mass range, hydrogen-burning is caused by the CNO cycle. The CNO cycle generates convection, so all the hydrogen in the core is exhausted by burning. For this reason, the stars can not sustain self-gravitation and begin to collapse. During the collapse, the hydrogen surrounding helium shell begins burning, and the collapse is stoped. In this case, unlike the p–p chain, stars sustain self-gravitation not only by density gradient but also by temperature gradient. After that, the helium core releases energy and becomes unable to sustain self-gravitation. The temperature of the helium core increases by collapse, the outer layer expands by hydrogen shell burning. The temperature of the helium core increases due to collapse, and the outer layer expands due to the burning of the hydrogen shell. The timescale of this evolution is quite short that it is rarely

observed.

Outer layer convection causes efficient expansion and stars rise up on the HR diagram. When the core temperature reaches 10^8 K, the triple-alpha process is triggered. In this case, the helium flash does not occur because the helium core is not in electron degenerate state. The surface temperature of stars increases by helium burning, and stars shit to the left size on the HR diagram. Finally, stars become AGB stars and then evolve into white dwarfs.

$8M_\odot < M < 40M_\odot$

This mass range of stars finally explode as a SN. In this thesis, we assume the maximum mass which can generate core collapsed is $40M_\odot$ (Heger et al., 2003). Convection occurs in the core of the star, and the star collapses after the hydrogen in the core is exhausted by burning. The core temperature increases as the core collapse. The thermal emission by the core transfers the energy to the outer layer. It activates hydrogen shell burning and the stars begin to expand. However, unlike the above cases ($M < 8M_\odot$), the helium-burning begins during the expansion of the stars. The nuclear reaction in the core proceeds until iron is synthesized. The structure of the interior of the star is called 'onion-like structure'. After that, the iron core collapses due to self-gravitation. When the temperature reaches $T > 10^{10}$ K, the star collapses due to the photo-disintegration of iron, which is expressed by the following equation.

$$^{56}\mathrm{Fe} \rightarrow 13\,^4\mathrm{He} + 4\mathrm{n} - 124.4\ \mathrm{MeV}, \tag{2.41}$$

$$^4\mathrm{He} \rightarrow 2\mathrm{p} + 2\mathrm{n} - 28.3\ \mathrm{MeV}. \tag{2.42}$$

where n is the neutron. The timescale of this collapse is ~ 0.1 s. The SN explosions occur due to the rebound of this collapse. Finally, the stars become neutron stars and black holes.

2.3 Gas

ISM is composed of gas, dust, cosmic-ray, and magnetic field. The chemical composition of ISM is a lot of hydrogen H ($\sim 70\%$ by mass) and helium He ($\sim 28\%$), and small amount of heavier elements (e.g., oxygen O, carbon C and nitrogen N) (Ferrière, 2001). It exists in several phases which differ in basic parameters (e.g., Field et al., 1969; McKee & Ostriker, 1977). In this thesis, we treat four phase according to dust evolution: molecular cloud (MC), cold neutral medium (CNM), and warm neutral medium (WNM), and the parameters of each ISM phase is listed in Table 2.1. The typical phase diagram is shown in Figure 2.7. Stars are formed in dense region of MC, and stellar winds and SN explosions re-supply material to ISM. Dust grains grow in CNM and WNM. In our model, we consider that grain-grain collisions occur in MC, CNM and WNM, and acceleration occurs in MC and

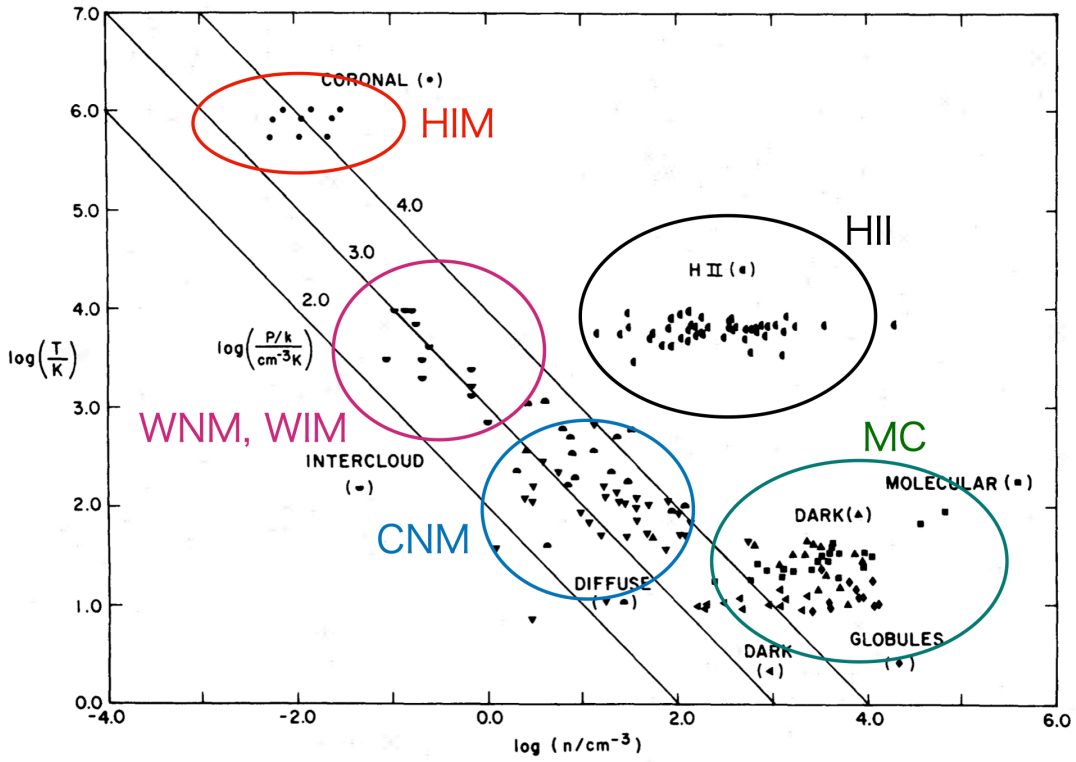

Figure 2.7: Interstellar gas phase diagram, based on seven galactic spectral line surveys. Credit: Myers (1978).

CNM.

Table 2.1: The parameters of each ISM phase.

ISM phase	T^{*}(K)	$n^{\dagger}$(cm^{-3})	$\Sigma_{\odot}{}^{\ddagger}(M_{\odot}$ pc$^{-2})$	$M^{\S}(10^{9}\ M_{\odot})$
MC	10–20	10^{2}–10^{6}	~ 2.5	$\sim 1.3^{\P}2.5^{\pounds}$
CNM	50–100	20–50	~ 3.5	> 6.0
WNM	6,000–10000	0.2–0.5	~ 3.5	> 6.0
WIM	$\sim 8,000$	0.2–0.5	~ 1.4	> 1.6
HIM	$\sim 10^{6}$	~ 0.0065		

* temperature.
† number density of hydrogen nuclei.
‡ the averaged mass density per unit area.
§ the mass contained in the entire Milky Way.
¶ Bronfman et al. (1988).
£ Clemens et al. (1988).

2.4 Cosmic dust

The cosmic dust is a small solid particle with a radius from a few molecules to 0.1 μm. Although the dust occupies a small mass fraction in the ISM component ($\sim$ 1%), it plays a major role in galaxy evolution. Dust grains in the galaxy attenuate by absorbing and scattering, in particular at the UV and optical. Dust grains in the galaxy attenuate UV and optical by absorption and scattering. Therefore, in order to determine the underling stellar population, it is necessary to consider the effects of dust grains that combine absorption and scattering. The IR region is dominated by dust re-radiation at the corresponding temperature. Dust grains could promote the coolant of the ISM by preventing gas heating up from interstellar radiation field. On the surface of dust grains, furthermore, hydrogen atoms easy to form hydrogen molecules (e.g., Cazaux et al., 2005) which are the ingredients of the star formation. The formation of hydrogen molecules from two hydrogen atoms requires the release of binding energy, but the rate of formation of these molecules in the gas phase is very slow because there is no place to release them in the gas phase. In contrast, on the surface of dust grains, the binding energy is absorbed by the dust grains as heat energy, so the reaction rate is fast (Hirashita & Ferrara, 2002). Hirashita & Ferrara (2002) calculated the effect of the dust grains for hydrogen molecular formation (shown in Figure 2.8). From the figure, the fraction of molecules increases more than 100 times due to the presence of dust particles at an age of 7×10^{8} yr.

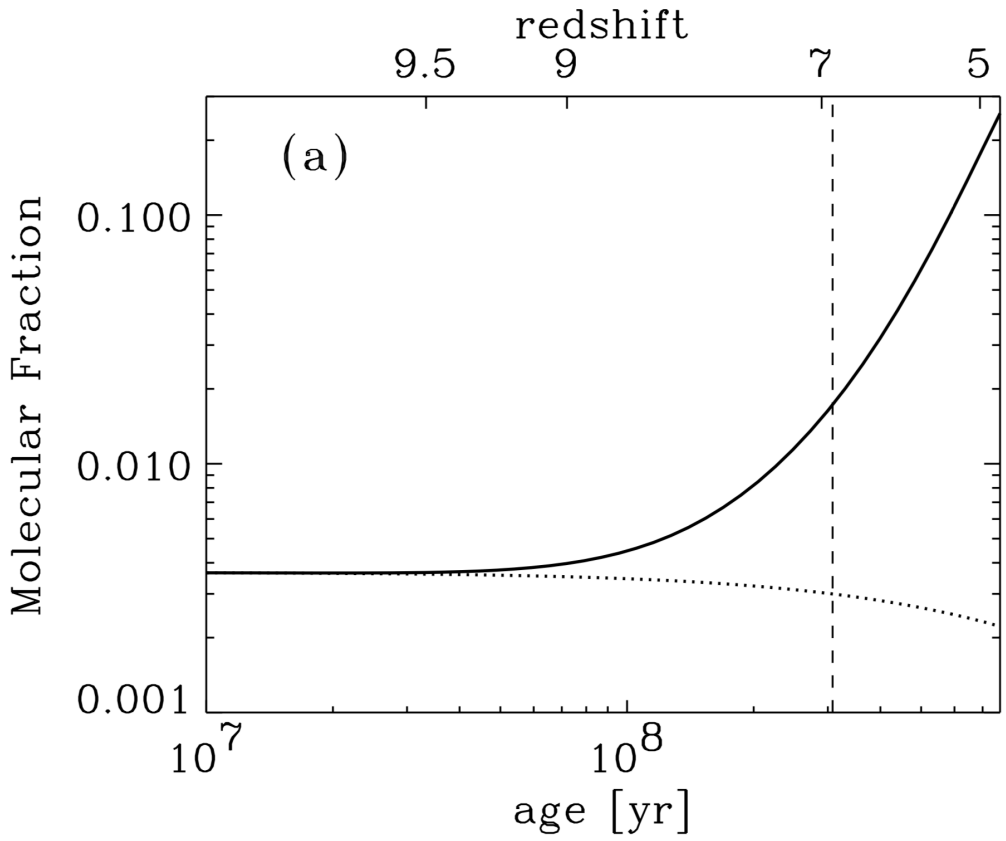

Figure 2.8: The evolution of the molecular fraction. The solid curve shows the case dust grains existent. The dotted curve represents the case that dust grains are not produced in the galaxy.

Chapter 3

Spectral energy distribution of galaxies

The components of galaxies except dark matter emit different wavelength photons by various physical processes. Basically, the higher the temperature of an radiating component, the higher the photon energy (the shorter the wavelength) becomes. Moreover, gas and dust also emit line spectrum. Galaxies are observed at various wavelengths (gamma-ray, X-ray, ultraviolet; UV, optical, infrared; IR and radio), and appear as completely different images at each wavelength. For example, when a proton, one of cosmic-rays, collides with interstellar gas, a neutral pion (π^0) is generated. It immediately decays (mean life time is 8.3×10^{-17} s; Dermer et al., 2013) and emits gamma rays. This gamma-ray is often detected around a supernova remnants (SNRs) because the strong shock wave from the SNR is considered to be one of the sources of cosmic rays (e.g., Ginzburg & Syrovatsky, 1965). Recent observations of SNR W44 by *Fermi* and AGILE provided evidence a π^0 decay features (e.g., Guillet et al., 2011; Cardillo et al., 2014).

For X-rays, galaxies have three kinds of emitting sources: X-ray binaries, spatially resolved compact objects (e.g., SNR, active galactic nucleus; AGN), and hot halo gas. Their contribution depends on the type of a galaxy (Fabbiano, 2006). The X-ray intensity of massive galaxies tends to be dominated by X-ray binaries, while low-mass galaxies such as the dwarf galaxy tend to be dominated by SNR. X-ray binaries and AGNs may have accretion disks formed by gases orbiting around massive central bodies. The accretion disk emits X-rays when the accretion gas releases gravitational energy and angular momentum (Pringle et al., 1973; Shakura & Sunyaev, 1976). The black hole is a very massive object that does not emit light and cannot be observed directly with light, but it is indirectly observed by the radiation from the accretion disk. SNR and high temperature phase (> 1 keV) of hot halo gas radiate Bremsstrahlung (free-free radiation) (Mewe et al., 1986; Hamilton et al., 1983; Borkowski et al., 2001). On the other hand, recombination (free-bound) radiation dominates emission by low temperature phase of halo gas (Mewe et al., 1986). Furthermore, electrons accelerated to a relativistic velocity by the SN shock radiate X-rays by synchrotron radiation (Mckee, 1974).

Radio emission is radiated by Bremsstrahlung from HII regions, which are regions ionized by UV photons from massive young stars, and by synchrotron

radiation by relativistic electrons (e.g., Klein et al., 1988; Carlstrom & Kronberg, 1991). In a normal galaxy, the fraction of the luminosity in radio region is only $< 10^{-4}$ of the overall bolometric galaxy luminosity (Condon, 1992).

As an example, the observed and model SED of NGC 4435 is shown in Figure 3.1. Most of the radiation from FUV to NIR wavelengths is emitted from stars,

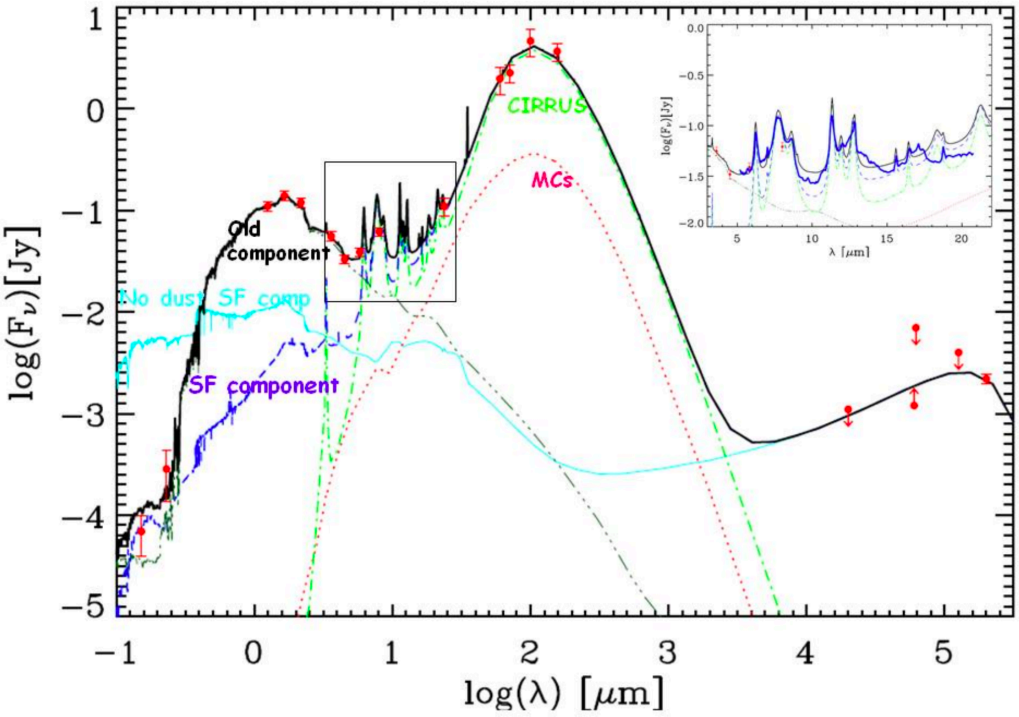

Figure 3.1: The observed SED of NGC4435 from Bressan et al. (2006). Credit: Silva (2009).

and the star formation history (SFH) can be estimated from the intrinsic radiation. However, since the emission of stars is strongly attenuated by dust grains, it is not possible to understand a true SFH only by observed UV emission. The IR radiation is dominated by a thermal emission from dust heated by the absorption of stellar radiation. Therefore, the emission in this region depends not only on the mass, composition and size distribution of the dust, but also on the star-forming activity. In the MIR region, characteristic radiation of PAHs due to vibrations and bands is observed. As described above, the true physical quantity cannot be directly obtained only by observing at a specific wavelength, but various physical quantities can be estimated by simultaneously fitting SEDs in a wide wavelength range. In addition, in order to construct a galaxy SED model, it is necessary to consider each physical process for each component. In this chapter, we introduce the background knowledge of the components of galaxy and effect of its on galaxy evolution.

3.1 Stars

Stellar emission can be approximated to a blackbody radiation. The blackbody is the ideal material that absorbs all incoming photons and radiates any wavelengths photons. The blackbody radiation by unit surface area depends only on the temperature, and the radiative energy is the maximum among objects with the same temperature. The actual radiation of a star deviates from blackbody radiation for several reasons (e.g., high temperature stellar has an absorption line by metals, ions, hydrogen and helium atoms at the wavelength of UV and low temperature) but the radiation from optically thick objects approximately become blackbody. The blackbody radiation with wavelength range $[\lambda, \lambda + \mathrm{d}\lambda]$, $B_\lambda(t)\mathrm{d}\lambda$, at temperature T is expressed as

$$B_\lambda(T)\mathrm{d}\lambda = \frac{2h_\mathrm{p}c^2}{\lambda^5}\frac{\mathrm{d}\lambda}{e^{h_\mathrm{p}c/\lambda k_\mathrm{B}T} - 1}, \tag{3.1}$$

where h_p is the Plank constant, c is the speed of light and k_B is the Boltzmann constant. Assuming that the radiation is blackbody radiation, the temperature obtained by following Stefan-Boltzmann's law is called the effective temperature T_eff:

$$F_\mathrm{bol} = \sigma T_\mathrm{eff}^4, \tag{3.2}$$

where F_bol is the bolometric flux from star, and $\sigma = 2\pi^5 k^4/15c^2h^3$ is the Stefan-Boltzmann constant.

The UV light in SED is dominated by photons from massive stars. Since massive stars have a very short lifetime (typically 10^6–10^7 yr), the SFR of the galaxy at that time can be estimated from UV observations by assuming that they will explode at the moment they are born (e.g., Kennicutt, 1998). On the other hand, low-mass stars that emit NIR have a very long lifetime, so we can estimate the total stellar mass assuming that they will not explode within the age of the Universe (e.g., Zibetti et al., 2009).

3.2 Gas emission

Due to the different ISM phases in galaxies, gases have various temperatures and chemical compositions and radiate various emission lines. Therefore, by observing the emission lines, we can get rich information on the properties of the gas. This section introduces some of the lines emitted by the gas.

21 cm line

This line is emitted by neutral hydrogen atoms. Hydrogen is a useful tracer of gas because it is the most abundant element in the Universe. A hydrogen atom is composed of a proton and an electron. Since both the proton and the electron have a spin quantum number of 1/2, they can have two types of spin angular momentum $\pm 1/2$. Therefore, the hydrogen atom has two different energy states. Since the parallel state has a bit of higher energy than the antiparallel state,

changing the state from parallel to antiparallel radiates the energy of the difference between these states. This energy is equivalent to a 21 cm radio emission. This transition is highly forbidden, and the rate of transition per one atom is very low (2.9×10^{-15} s^{-1}). One may think that the rate is low and the event cannot be detected. However, 21 cm line is very common event in the Universe, because the hydrogen occupy the 80 % of the baryon in the Universe.

CO line

Hydrogen molecules H_2 are dominant composition of the MC. As mentioned in §2.2.1, however, H_2 has no permanent electric dipole moment and have the lowest quadruple rotational transitions. Furthermore, as the MC have low temperature ($\sim$ 10 K), the emissions from vibrational and electron orbital transitions also can be not detected. Instead, the rotational transition emission from CO which is the second dominant molecular in the MC is used for H_2 tracer (Young & Scoville, 1991). In particularly, ^{12}CO(J = 1–0) line rotational transition line (wavelength 2.6 mm) is commonly used for obtaining hydrogen molecular with CO–H_2 conversion factor. Although, this conversion factor is determined by a lot of studies for decades (Young & Scoville, 1991; Wild et al., 1992; Guelin et al., 1995; Tacconi et al., 2008), there is no standard conversion factor. This factor nonlinearly depends on the ISM metallicity, gas density, cosmic-ray density, and UV density (Kaufman et al., 1999).

Lyman alpha line

Lyman alpha (Lyα) is the resonance line emitted from hydrogen atoms when transition between the ground state $1s$ and the excited state $2p$, and that of wavelength is 1216 Å. There is two process of emitting Lyα photons. One is the recombination in the ionized gas of HII regions embedded in MCs. It is used as a tracer of star formation region. The other process is that a free electron which has high energy collide with HI and excite it to $2p$ state. Lyα is easy to be absorbed and scattered by dust grains. In a local galaxy, it is difficult to escape Lyα from HII region, because local galaxy tends to having large amount of dust grains. On the other hand, in high-z ($3 < z$) regions, a lot of the star-forming galaxy called Lyman alpha emitters (LAEs) is detected (e.g., Hu & McMahon, 1996; Pascarelle et al., 1996; Gawiser et al., 2007; Hagen et al., 2014; Ouchi et al., 2018). Thus, the line is frequently used to study of galaxy formation in early Universe.

Gas component in SED model

We assume that the ISM in the galaxy compose of three phases, warm neutral medium (WNM), cold neutral medium (CNM), and molecular cloud (MC). We use the same properties of each the ISM phases as Nozawa et al. (2015) and it is listed in table 3.1. From point of view of the galaxy SED, the contribution of the gas is not significant (Young & Scoville, 1991; Hollenbach & Tielens, 1997). Present our model do not include the lines from gas.

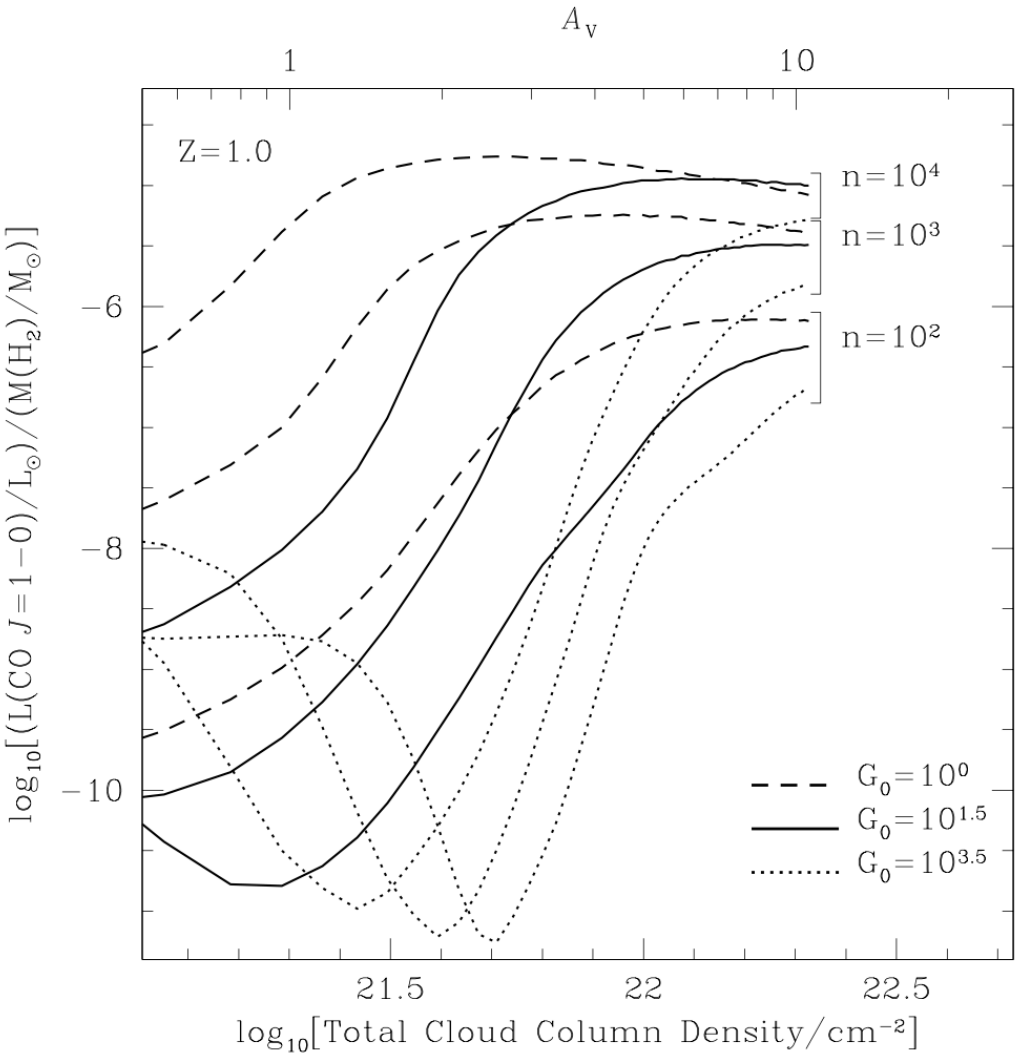

Figure 3.2: The ^{12}CO (J = 1–0) line divided by the mass of hydrogen molecule (H_2) unit in $M_\odot$ (conversion factor) versus the total cloud column density and the attenuation A_V. This figure shows that the condition with the cloud density $n = 10^2, 10^3$ and 10^4 and the FUV intensities $G_0 = 1$ (dashed curves), $10^{1.5}$ (solid curves), and $10^3.5$ (dotted curves). $G_0 = 0$ represent FUV intensity in units of local interstellar value. Metallicity is set to be solar ($Z_\odot$). Credit:Kaufman et al. (1999)

Table 3.1: The physical properties of ISM phases in our model

ISM phase	Temperature (K)	Number density (cm^{-3})
CNM	100	30
WNM	6,000	0.3
MC	25	300

3.3 Dust grains

Figure 3.3 is the emission by the interstellar dust model (Dwek et al., 1997). The

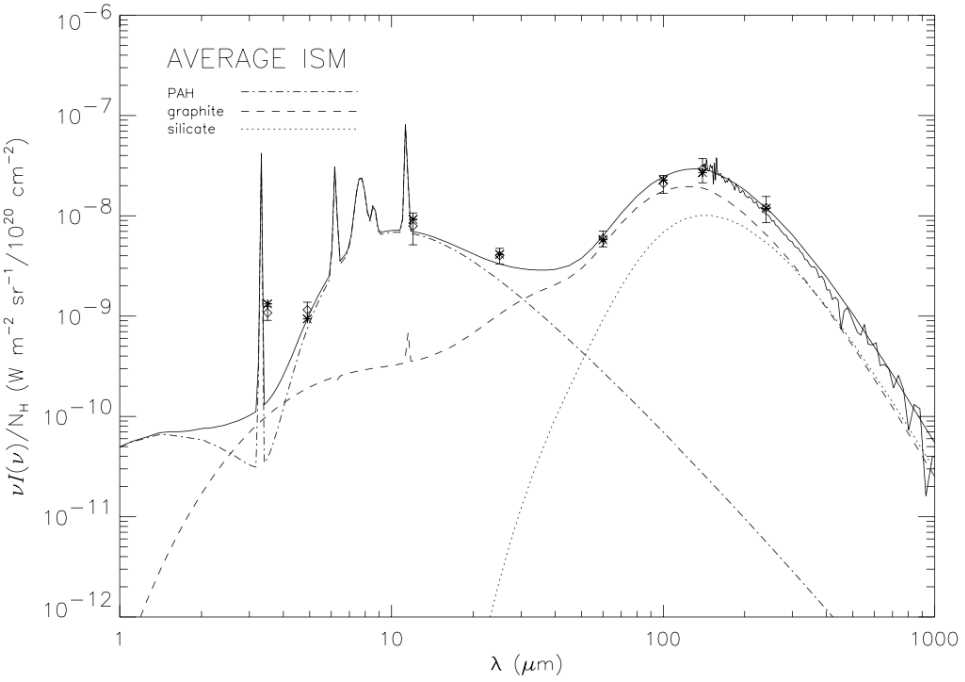

Figure 3.3: The spectrum emitted by average interstellar dust model. The solid, dashed, dotted, and dot-dashed line represents overall, graphite, silicate, and PAH emission, respectively. Credit: Dwek et al. (1997).

chemical component of dusts can be divided into carbonaceous and silicate grains (e.g., Draine, 2003). Large grains (LGs, radius of $a > 200$ Å) are in temperature equilibrium with the UV and optical field emitted by the stars and dominate IR emission above 60 μm. The radiation is approximated by the product of blackbody radiation and the absorption coefficient $Q_{\rm abs}$.

The wavelength range (10 μm $< \lambda <$ 60 μm) is dominated by emission from very small grains (VSGs, radius range in 10 Å $< a <$ 200 Å), they are mainly composed of carbonaceous grains. Since VSG has a small specific heat capacity, it does not equilibrate with the radiation field and has a wide range of temperatures from very high to low (Desert et al., 1990; Dwek et al., 1997; Draine & Li, 2001; Takeuchi et al., 2003, 2005). Therefore, the radiation of VSG spreads continuously.

In shorter wavelength range (3 μm $< \lambda <$ 15 μm), the emissions from ISM are dominated by unidentified infrared emission bands (UIBs), infrared emission features (IEFs) and aromatic infrared bands (AIBs). UIBs are thought to be related polycyclic aromatic hydrocarbons (PAHs). PAHs have various emission line, the intense emission line of PAHs are 3.3, 6.2, 7.7, 8.6, 11.3, and 12.7 μm. The vibrational modes are C-H (3.3 μm) and C-C (6.2 and 7.7 μm) stretching modes, C-H (8.6 μm) in-plane bending mode, C-H (11.3 and 12.7 μm) out-plane bending modes, respectively (Draine, 2003). PAH is observed in almost all ISM environment except occupied strong UV radiation field (Boselli et al., 2004).

3.3.1 Optical properties of dust grains

The optical properties of dust grains depend on the shape of grains. Observations have confirmed that the polarization of starlight is caused by the elongated dust in the ISM absorbing and scattering the light (e.g., Davis & Greenstein, 1951). However, we assume the dust grains to be spherical dielectric particles because we do not consider polarized light considering only the extinction, the grain size distribution, and the grain radiation energy.

Cross section

The absorption and scattering cross-section by single spherical grains is defined as follows. Consider a plane wave with flux F_0 coming toward the grain. When the wave hit the grain, the wave is scattered to angle (θ, ϕ) like Figure 3.4. The flux of scattered light is $F(\theta, \phi)$, and it received at distance r. If r is appropriately large $(r \gg \lambda/2\pi)$, observed flux is proportional to F_0/r^2, and it is written as,

$$F(\theta, \phi) = \frac{F_0}{k^2 r^2} \mathcal{L}(\theta, \phi). \tag{3.3}$$

where k is the wavenumber, $\mathcal{L}(\theta, \phi)$ is the coefficient function of independent from r and F_0.

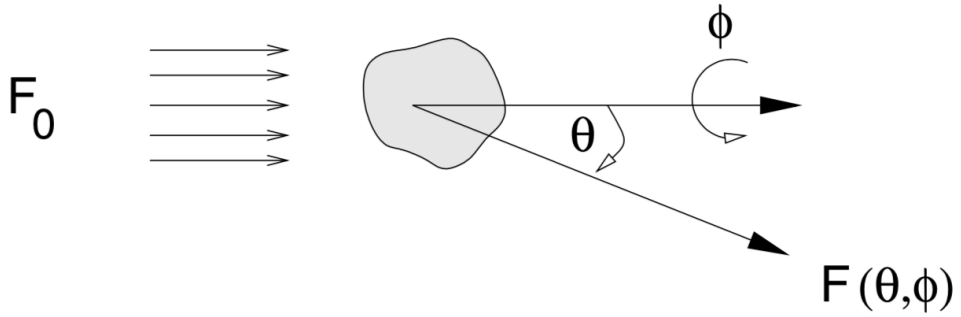

Figure 3.4: Single grain scatters the plane wave with flux F_0. The scattered wave direction is (θ, ϕ) and the flux is $F(\theta, \phi)$. Credit:Krugel (2003)

Considering the scattering cross-section of a grain $C^{\rm sca}(\lambda)$ defined as the geometric grain area, the total energy $F_0 C^{\rm sca}$ equals total scattering energy, integrated $\mathcal{L}(\theta, \phi)/k^2$ by all solid angles and it is represented as,

$$C^{\rm sca} = \frac{1}{k^2} \int_0^{2\pi} {\rm d}\phi \int_0^{\pi} {\rm d}\theta \mathcal{L}(\theta, \phi) \sin\theta \tag{3.4}$$

where $\mathcal{L}(\theta, \phi)/k^2$, normalized by $C^{\rm sca}$,

$$p(\theta, \phi) \equiv \frac{\mathcal{L}(\theta, \phi)/k^2}{C^{\rm sca}} \tag{3.5}$$

is called the phase function (Li, 2009). In the same way, the absorption coefficient of grain is defined. The sum of absorption and scattering coefficient means the extinction coefficient

$$C^{\rm ext}(\lambda) = C^{\rm abs}(\lambda) + C^{\rm sca}(\lambda). \tag{3.6}$$

The average cosine of the scattering angle θ is called the asymmetry parameter g and is defined from Equation (3.5) as,

$$g \equiv \langle \cos\theta \rangle = \int_0^{4\pi} p(\theta, \phi) \cos\theta \mathrm{d}\Omega. \tag{3.7}$$

g can verify the range [-1, 1]. When $g = 0$, the scattering is isotropic. $g = 1$ means pure forward scattering; and $g = -1$ means pure backscattering.

The cross-sections have dependence on the grain radius. On the other hand, the dimensionless coefficients Q are used and defined as,

$$Q^{\mathrm{sca}} = C^{\mathrm{sca}}/\pi a^2 \tag{3.8}$$
$$Q^{\mathrm{abs}} = C^{\mathrm{abs}}/\pi a^2 \tag{3.9}$$
$$Q^{\mathrm{ext}} = C^{\mathrm{ext}}/\pi a^2 \tag{3.10}$$
$$\tag{3.11}$$

The scattering albedo ω is defined as the ratio of the extinction coefficient with the scattering coefficient,

$$\omega = \frac{C^{\mathrm{sca}}}{C^{\mathrm{ext}}} = \frac{Q^{\mathrm{sca}}}{Q^{\mathrm{ext}}}, \tag{3.12}$$

when albedo has high value, a lot of energy is scattered.

3.4 Dust attenuation

Definition of Magnitude

Astronomer frequently use the 'magnitude' for the scale of the stellar brightness. It is defined that when the magnitude increases by 5, the observed flux decreases by a factor of 100, the brightness becomes larger with decreasing of magnitude. Considering the difference of two object 1 and 2 with the magnitude m_1, m_2 and the flux f_1, f_2, respectively, it is represented as

$$m_2 - m_1 = -2.5 \log(F_2/F_1). \tag{3.13}$$

There are two species of magnitude, the apparent magnitude at wavelength λ, m_λ depends on stellar distant D. The object set to 10 pc from the earth, the brightness is absolute magnitude M_λ, and it is expressed with m_λ and D as,

$$m_\lambda - M_\lambda = 5 \log_{10} \left(\frac{D}{\mathrm{pc}} \right) - 5. \tag{3.14}$$

This expression dose not require the intrinsic brightness. When there is dust grains in the path of starlight, add a term A_λ in the right-hand side of Equation (3.14) for effect of dust extinction.

Definition of extinction

In the mentioned above sections, dust grains extinct the emissions. Consider the light with the specific intensity I_λ through the region with the distance ds. The region is distributed the grains with constant number density n, and the extinction coefficient $C^{\rm ext}(\lambda)$. In this condition, the variation of intensity dI is,

$$\mathrm{d}I_\lambda = -I_\lambda n C^{\rm ext}(\lambda)\mathrm{d}s. \tag{3.15}$$

Notably, this region have no emission source. Using the optical depth τ_λ at wavelength λ defined as

$$\mathrm{d}\tau_\lambda = -nC^{\rm ext}(\lambda)\mathrm{d}s, \tag{3.16}$$

the intensity I_λ is represented as integrating Equation (3.15),

$$I_\lambda = I_{0,\lambda}\exp(-\tau_\lambda), \tag{3.17}$$

where $I_{0,\lambda}$ is the intrinsic specific intensity, and

$$\tau_\lambda = C^{\rm ext}(\lambda)\int n\mathrm{d}s \tag{3.18}$$

is the optical depth expression. From equation (3.13), (3.17), the extinction A_λ is defined as the reduction of the magnitudes,

$$A_\lambda \equiv m_{0,\lambda} - m_\lambda = -2.5\log_{10}(e^{-\tau_\lambda}) \simeq 1.086\tau_\lambda. \tag{3.19}$$

It is difficult to calculating the absolute value of interstellar extinction A_λ. Because, it depends on the distance and the amount of dust grains between the star and observer. The relative value of A_λ is estimated by following methods.

Definition of color excess

Consider two stars (represented by i = 1, 2, respectively)with same intrinsic luminosity $L(\lambda)$, distant from observer D_i and optical depth $\tau_i(\lambda)$, the flux $F_i(\lambda)$ is represented as

$$F_i(\lambda) = \frac{L(\lambda)}{4\pi D_i^2}e^{-\tau_i(\lambda)}. \tag{3.20}$$

The difference of apparent magnitude of these stars $\Delta m(\lambda) \equiv m_1(\lambda) - m_2(\lambda)$ is express by Equation (3.13), (3.20) as

$$\begin{aligned}
\Delta m(\lambda) &= m_2(\lambda) - m_1(\lambda) && (3.21)\\
&= -2.5\log_{10}\left[\left(\frac{D_1}{D_2}\right)^2 e^{-[\tau_2(\lambda)-\tau_1(\lambda)]}\right] && (3.22)\\
&= -5\log_{10}\left(\frac{D_1}{D_2}\right) - \frac{2.5}{\ln(10)}[\tau_1(\lambda)-\tau_2(\lambda)] && (3.23)\\
&= -5\log_{10}\left(\frac{D_1}{D_2}\right) - [A_1(\lambda)-A_2(\lambda)]. && (3.24)
\end{aligned}$$

If the distance of star 2 is near to observer and it could not be attenuated by dust, $\tau_2(\lambda) = 0$, the difference between $\Delta m(\lambda)$ and $\Delta m(\lambda')$ is

$$\begin{aligned} E(\lambda, \lambda') &= \Delta m(\lambda) - \Delta m(\lambda') && (3.25) \\ &= [m(\lambda) - m(\lambda')]_{\text{observed}} - [m(\lambda) - m(\lambda')]_{\text{intrinsic}} && (3.26) \\ &= A(\lambda') - A(\lambda), && (3.27) \end{aligned}$$

this equation dose not contain distant D. When $\lambda' = 0.55$ μm (center wavelength of V band), $E(\lambda - V)$ is called the selective extinction and, the color excess between the B (0.44 μm) and the V band,

$$E_{B-V} = E(B, V), \tag{3.28}$$

is called the standard color excess.

Extinction curve

The color excess that selective extinction $E(\lambda, V)$ normalized by standard excess E_{B-V}

$$\text{Ext}(\lambda) = \frac{E(\lambda, V)}{E_{B-V}} = \frac{A_\lambda - A_V}{A_B - A_V} = \frac{\tau_\lambda - \tau_\text{V}}{\tau_\text{B} - \tau_\text{V}}, \tag{3.29}$$

is used for expression of the extinction curve traditionally.

We show the average extinction curve of Milky Way with wavelength range UV to NIR in Figure 3.5. The feature of bump in $\lambda = 2175$ Å$(1/\lambda = 4.6$ $\mu\text{m}^{-1})$ is

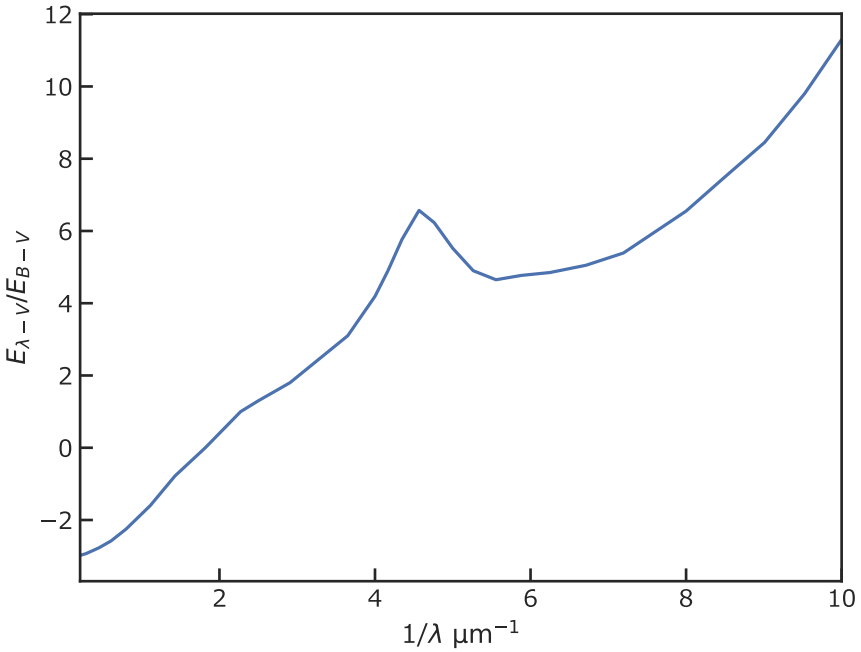

Figure 3.5: The average extinction curve of MW (Whittet, 2003)

explained by the small carbonaceous ($a < 0.01$ μm) dust grains (Weingartner & Draine, 2001, e.g.,). In optical region ($1/\lambda \sim$1–3 mum^{-1}), extinction is proportion to inverse wavelength ($1/\lambda$). The dust extinction of the same size as wavelength makes this feature. Thus, extinction of optical region is dominated by 0.1 μm dust grains. The extinction curve also increase with inverse wavelength in UV region ($1/\lambda > 8\mu\mathrm{m}^{-1}$), we can deduce existence of smaller dust grains ($a < 0.01$ μm). Assuming spherical shape grains, the power low size distribution of grains

$$f(a) \propto a^{-3.5} \tag{3.30}$$

is reproduce UV slope in Figure 3.5. This power low size distribution is well known as MRN distribution (Mathis et al., 1977).

When $\lambda \to \infty$ ($1/\lambda \to 0$), the ratio of total over selective extinction is defined as

$$R_\mathrm{V} = \frac{A_V}{E_{B-V}}. \tag{3.31}$$

This value has various values each directions, and in general interstellar in MW, $R_\mathrm{V} = 3.1$.

$$\frac{E_{\lambda-\mathrm{V}}}{E_{B-V}} = \frac{A_\lambda - A_V}{E_{B-V}} = R_\mathrm{V}\left(\frac{A_\lambda}{A_V} - 1\right). \tag{3.32}$$

Thus, the absolute extinction A_λ/A_V is deduced from E_λ/E_{B-V} and R_V.

The extinction curve is different each galaxies. For example, Small Magellanic Cloud (SMC) generate the steeper UV slope and does not have the 2175 Åbump. Large Magellanic Cloud (LMC) have an intermediate extinction curve between those of MW and SMC. Some studies suggest that these differences are generated by the small metallicity [LMC and SMC have ~ 0.5 and ~ 0.22 $Z_\odot$, respectively (e.g., Larsen et al., 2000)] and difference of dust properties (e.g., Nozawa et al., 2015). In addition, QSO observations in high-z ($z > 4$) galaxies suggest that a flatter attenuation curve tends to be suitable (e.g., Maiolino et al., 2004; Gallerani et al., 2010).

3.5 Currently available SED models

Some codes are used for fitting observed galaxy SEDs. These codes are adopted different assumptions for inferring star formation history (SFH), dust attenuation, dust size distribution, dust properties, dust emission, and galaxy geometry. Well-known and popular models are the Code for Investigating GALaxy Evolution (CIGALE, Burgarella et al., 2005; Noll et al., 2009; Ciesla et al., 2016; Boquien et al., 2019), the Multi-wavelength Analysis of Galaxy PHYSical properties (MAGPHYS, Da Cunha et al., 2008), and the GRAphite-SILicate approach (GRASIL, Silva et al., 1998; Granato et al., 2000).

CIGALE can select three type of SFH: single or double exponentials, delayed SFH. The SFH of single or double exponentials is represented as

$$\mathrm{SFR}(t) \propto \begin{cases} \exp(-t/\tau_0) & \text{if } t < t_0 - t_1 \\ \exp(-t/\tau_0) + k \times \exp(-t/\tau_1) & \text{if } t > t_0 - t_1 \end{cases} \tag{3.33}$$

Where t_0 and t_1 are the galaxy time and star burst starting time relative to t_0, respectively. τ_0 and tau_1 are the e-folding times, and k is the relative amplitude of the second term. The delayed SFH is,

$$\mathrm{SFR}(t) \propto \frac{t}{\tau^2} \times \exp(-t/\tau) \tag{3.34}$$

Where t_0 is the starting time of star formation, and τ is the SFR peak time. This SFH can reproduce early-type (for small τ) and late-type (for large τ) galaxies. The periodic SFH is expressed by combination with exponential, delayed, and rectangular. For the dust attenuation curve, the code uses a modified starburst model based on the Calzetti et al. (2000) and Leitherer et al. (2002). The attenuation curve can be added UV bump modeled as a Lorentzian like Drude profile (Drude, 1900a,b). The attenuation curve is

$$k_\lambda = D_\lambda + k_\lambda^{\mathrm{starburst}} \times (\lambda/550\ \mathrm{nm})^\delta \times \frac{E(B-V)_{\delta=0}}{E(B-V)_\delta} \tag{3.35}$$

Where D_λ is the Drude profile, δ is the slope, and the last term is normalization (Noll et al., 2009; Boquien et al., 2019). Figure 3.6 shows the attenuation curve calculated by CIGALE with various parameters, various attenuation curves can be created by changing these parameters.

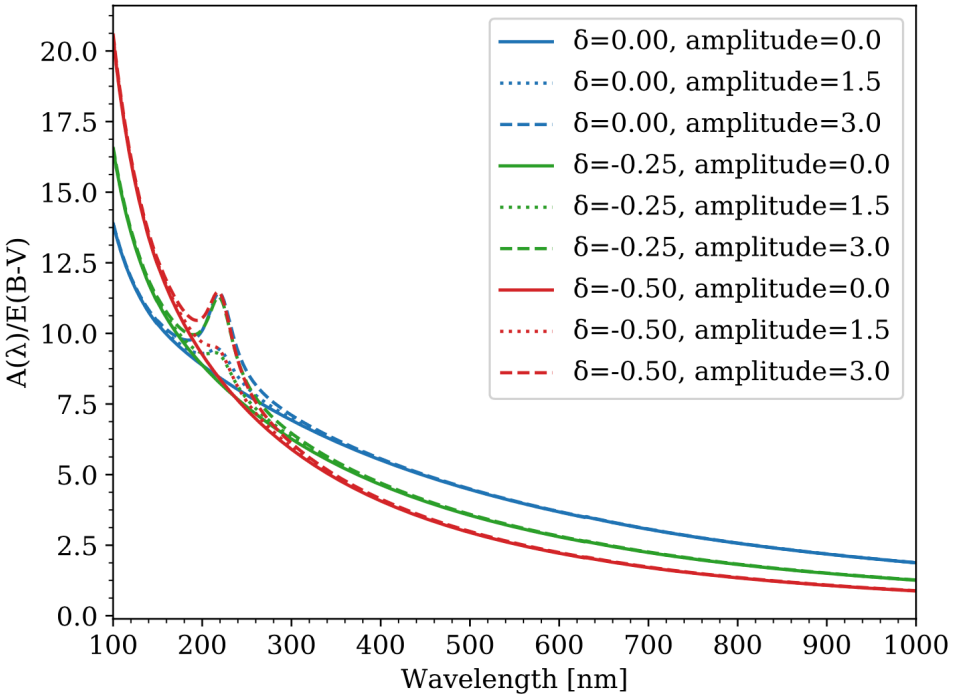

Figure 3.6: The attenuation curve generated by CIGALE. Credit: Boquien et al. (2019)

Dust emission of the code is defined by energy balance between the energy absorbed by dust and re-emitted by dust grain. The dust properties came from

Draine & Li (2007); Draine et al. (2014), and dust mass distribution is represented as Equation (23) of Draine & Li (2007)

$$\frac{\mathrm{d}M_{\mathrm{dust}}}{\mathrm{d}U} = (1-\gamma)M_{\mathrm{dust}}\delta(U-U_{\mathrm{min}}) + \gamma M_{\mathrm{dust}}\frac{(\alpha-1)}{U_{\mathrm{min}}^{1-\alpha}-U_{\mathrm{max}}^{1-\alpha}}U^{-\alpha} \tag{3.36}$$

where γ is the fraction of the dust mass that is exposed to intensity of star forming region. U is the starlight intensity, U_{min} and $_{\mathrm{max}}$ are minimum and maximum starlight intensity, respectively. α is the power low index and it is set to -2 in the default of CIGALE.

MAGPHYS applies the superposition of following exponentially declining SFR model as SFH,

$$\mathrm{SFR}(t) \propto \exp(-\gamma t). \tag{3.37}$$

The dust attenuation is the two-phase model (Charlot & Fall, 2000). The one is the phase that the light emitted by young star (< 10 Myr)is absorbed by molecular cloud. Another is the ambient ISM which absorb only the light emitted by stars older than 10 Myr. The optical depth of the stars in the two-phase are represented as

$$\tau_\lambda^{\mathrm{MC}} = (1-\mu)\tau_V(\lambda/550\ \mathrm{nm})^{-1.3} \tag{3.38}$$

$$\tau_\lambda^{\mathrm{ISM}} = \mu\tau_V(\lambda/550\ \mathrm{nm})^{-0.7} \tag{3.39}$$

where τ^{MC} is the optical depth of molecular cloud, τ^{ISM} is the optical depth of ISM, τ_V is the total effective V-band absorption optical depth, and μ is the fraction of dust mass in diffuse phase ISM.

GRASIL assumes a variant of Schmidt-type law for the SFR,

$$\mathrm{SFR}(t) = \nu M_{\mathrm{gal}}(t)^k + f(t) \tag{3.40}$$

where ν is the times scale of star formation, $M_{\mathrm{gal}}(t)$ is the galaxy mass at time t, k is the constant value, and $f(t)$ is the optional function (e.g., for starburst). The SFH of the code is selected from 49 types for the spheroidal galaxies, and 20 types for the disk galaxies, and includes infall model. The code relies on a geometry of the galaxy which is selected by user, and the geometry is selected from two types, spheroidal and disk (shown in Figure 3.7).

In the case of spheroidal galaxy, they apply King profile (King, 1972)

$$\rho(r) = \rho_0\left[1+\left(\frac{r}{r_{\mathrm{c}}}\right)^2\right]^{-\gamma}. \tag{3.41}$$

where rho is star and dust density at distance from center r, ρ_0 is the central density, r_{c} is the critical radius, and γ is the set to 3/2 for stellar component. On the other hand, in the case of a disk galaxy, the following formula is adopted as the geometry,

$$\rho(R,z) = \rho_0 \exp\left(\frac{-R}{R_{\mathrm{d}}}\right)\exp\left(\frac{-|z|}{z_{\mathrm{d}}}\right) \tag{3.42}$$

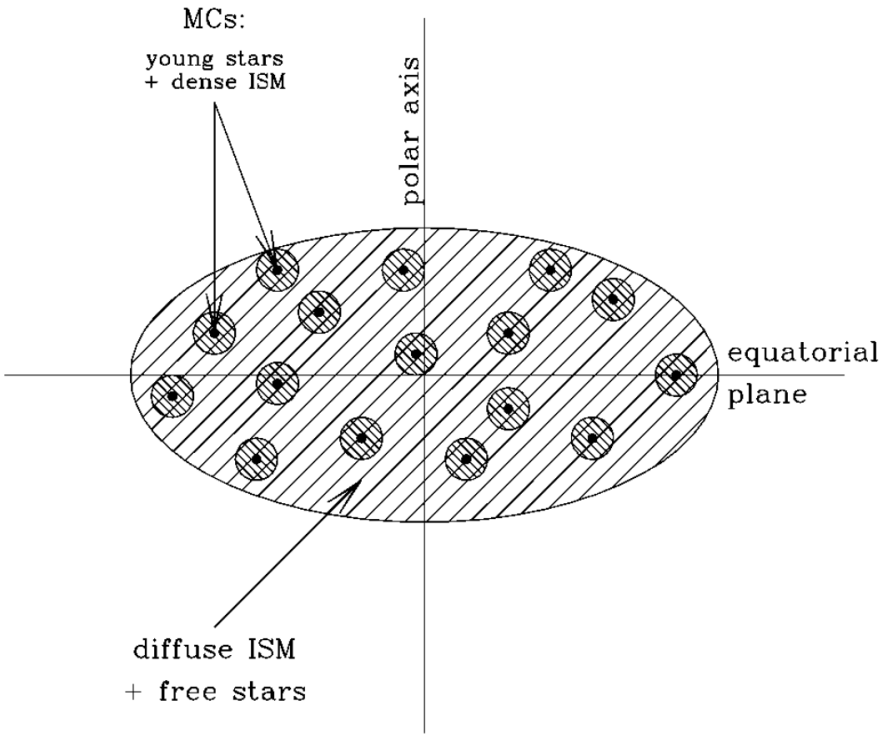

Figure 3.7: The schematic of geometry of GRASIL. Credit: Silva et al. (1998)

where R and z is the radial and vertical distance from center of the galaxy, $R_{\rm d}$ and $z_{\rm d}$ is the radial and vertical scale lengths of dust. The $r_{\rm c}$, $R_{\rm d}$, and $z_{\rm d}$ are independent free parameters in the code. The attenuation is calculated by radiative transfer, and grain opacities are from Laor & Draine (1993). The dust size distribution of graphite is consider as

$$\frac{{\rm d}n}{{\rm d}a} = \begin{cases} An_{\rm H}a^{\beta_1} & \text{if } a_b < a < a_{\rm max} \\ An_{\rm H}a_b^{\beta_1-\beta_2}a^{\beta_2} & \text{if } a_{\rm min} < a < a_b \end{cases} \tag{3.43}$$

with $a_{\rm min} = 8$ Å, $a_{\rm max} = 0.25$ μm, $a_b = 50$ Å, $\beta_1 = -3.5$, $\beta_2 = -4.0$, and $A = 10^{-25.22}$ cm$^{2.5}$H^{-1}. For silicate grains, they use the distribution same as Draine & Lee (1984), based on MRN (Mathis et al., 1977), a single power law with $a_{\rm min} = 50$ Å, $a_{\rm max} = 0.25$ μm, $\beta = -3.5$, and $A = 10^{-25.11}$ cm$^{2.5}$H^{-1}.

The confidence of that of ability is confirmed by several studies (e.g., Hayward & Smith, 2015; Pappalardo et al., 2016; Hunt et al., 2019). For example, MAGPHYS is compared with the SED which is generated from hydrodynamical simulations of an isolated disc galaxy and a major galaxy merger (Hayward & Smith, 2015). It shows that MAGPHYS generally able to recover physical parameters. However, when the true dust attenuation curve differs from nearby galaxies which are assumed by MAGPHYS, the code might have difficulty to infer physical parameters. Figure 3.8 shows the sample of SED fitting for simulated SED in Hayward & Smith (2015). The simulated SED is made assuming MW type atten-

uation, while the MAGPHYS fitting assumes SMC type dust. MAGPHYS fitting

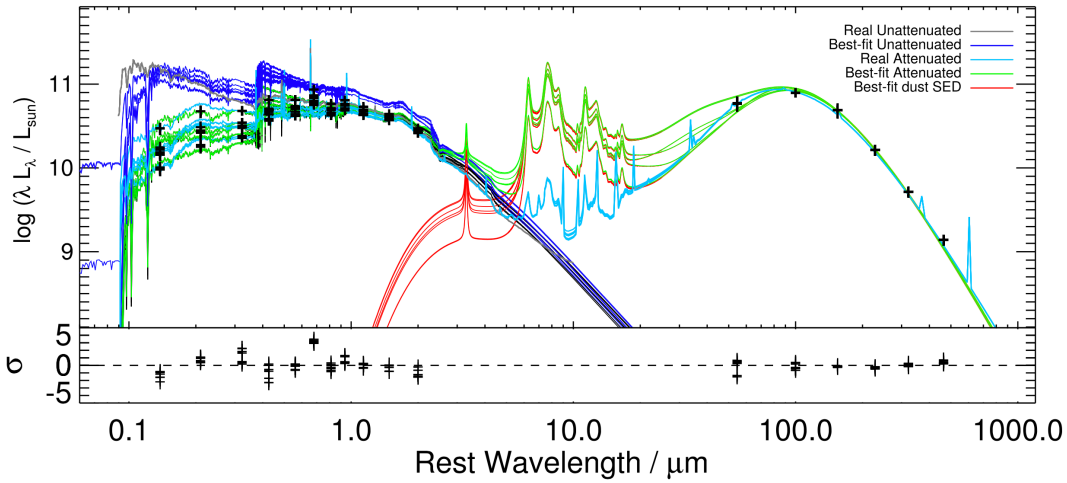

Figure 3.8: The sample of SED fit for $t - t(\mathrm{SFR_max}) = -1.47$ Gyr in Hayward & Smith (2015). The gray line shows true intrinsic (unattenuated) SED, and the cyan lines show the true observed SEDs for each of the seven inclination angles with the MW-type attenuation curve. The blue, green, and red lines show the best-fitting result of intrinsic, attenuated, and dust emission by MAGPHYS assuming the SMC-type attenuation curve, respectively. The bottom panel shows the residuals between true and MAGPHYS fitting result. Credit: Hayward & Smith (2015)

result of intrinsic (unattenuated) SEDs (blue lines) is differ from the true intrinsic SED (gray line), especially in the short wavelength range. This means that the difference of assuming dust attenuation from true one cause the misunderstanding of galaxy physical properties.

Hunt et al. (2019) fit the updated SEDs (Dale et al., 2017) from the UV to sub-millimeter of 61 sample galaxies from the Key Insight on Nearby Galaxies: A Far-Infrared Survey with *Herschel* (KINGFISH: Kennicutt et al., 2011) for comparing three dust models: CIGALE, GRASIL, and MAGPHYS. The codes generally reproduce roughly the same SEDs and consistent physical properties from observed galaxy SEDs. However, MIR wavelength region, which is dominated by the PAH emission, might show very different shape and derived different parameters. In particular, the codes infer very different SFR from a low specific SFR galaxy (Figure 3.9), and tend to overestimate the attenuation at UV emission.

3.5.1 Summary of present SED models

In the above, we introduced the outline of the three SED models of CIGALE, MAGPHYS, and GARASIL, and introduced the comparison of the models. As mentioned above, there are various SED models, each assuming different SFH, geometry, dust attenuation, and dust emission. Note that this is just an example, and most models have the flexibility to change inputs such as SFH. Any model

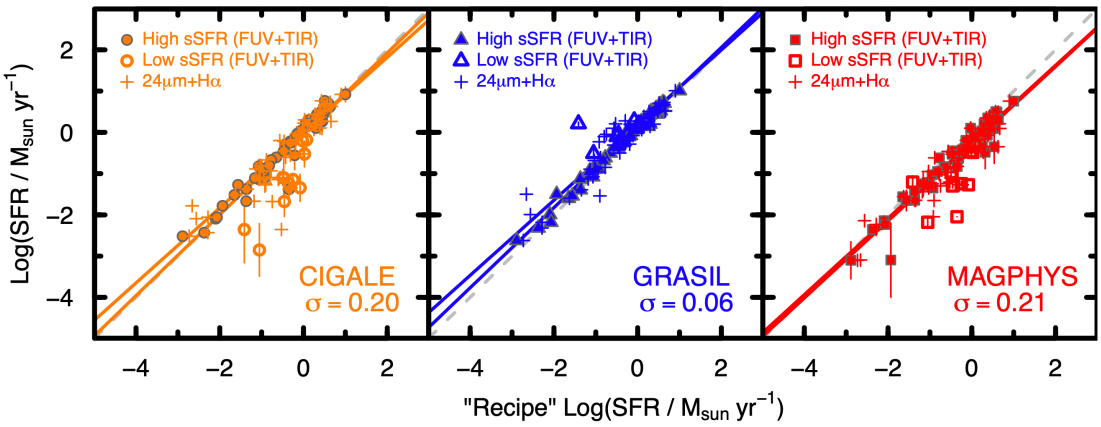

Figure 3.9: The SFR derived by SED fitting vs. the recipe SFR derived by different method. Dark-orange circles, bleu triangles, and red squares show the result by CIGALE, GRASIL, and MAGPHYS, respectively. Filled symbols represent high specific SFR ($\log(\mathrm{sSFR/yr^{-1}}) > -10.6$)) and open symbols represent low specific SFR ($\log(\mathrm{sSFR/yr^{-1}}) < -10.6$). Credit: Hunt et al. (2019).

can be applied to a wide range of galaxies and can reproduce the observed SED well. However, each model may estimate different properties, and in particular, the dust mass estimation often gives different values. It is considered that the cause is that only GRASIL among the three models considers radiative transfer in realistic geometry.

Most models use a empirical model in which the dust size distribution is represented by a power low of radius, such as the MRN distribution $\mathrm{d}n/\mathrm{da} \propto a^{-3.5}$ and Calzetti low Calzetti et al. (1994), which is designed to reproduce the attenuation curve from observations of nearby galaxies. However, there is a suggestion that a steeper attenuation curve is more suitable than the Calzetti low, the attenuation curve of MW-type, and Magellanic Cloud-types even in a normal disk galaxies (e.g., Inoue, 2005). Inoue (2005) says that the attenuation curve of the Calzetti low is reproduced when changing to a high gas density like a starburst galaxy. Furthermore, it has been suggested that distant galaxies have a flatter attenuation curve than neighboring galaxies (e.g., Maiolino et al., 2004; Gallerani et al., 2010; Hjorth et al., 2013; Asano et al., 2014). The flat attenuation curves of these high red shift galaxies are provided by SNe II of the massive, short-lived stars, rather than dust evolution (e.g., Maiolino et al., 2004; Hirashita et al., 2008). Therefore, in order to consider a realistic dust attenuation curve and dust size distribution, it is necessary to consider produce and growth with theory. In our model, we constructed a galaxy SED model that includes dust chemistry evolution (Asano et al., 2013a,b, 2014).

Part II

Construction of spectral energy distribution model

Chapter 4

Dust evolution model based on the chemical evolution

Our dust evolution model is based on the chemical evolution approach by Asano et al. (2013a,b, 2014) and Nozawa et al. (2015). We consider eight dust evolution processes: dust production by the AGB and SNe II stars, dust destruction by SN shocks, dust grain growth by metal accretion in the cold neutral medium (CNM) and molecular cloud (MC), and two type grain-grain collisions (they are called coagulation and shattering) in the warm neutral medium (WNM), CNM and MC. In this thesis, ISM phase fractions are fixed to $\eta_{\rm WNM} = 0.5$, $\eta_{\rm CNM} = 0.3$, and $\eta_{\rm MC} = 0.2$ except for §7.1.3. These values are chosen to reproduce the MW attenuation curve by Nozawa et al. (2015).

In this model, we treat nine species of dust (C, Si, SiO_2, Fe, FeS, Al_2O_3, MgO, $MgSiO_3$, and Mg_2SiO_4) (Nozawa et al., 2007; Zhukovska et al., 2008). However, when we consider of grain growth and grain-grain collisions, we do not fully treat all of the species but divide them into into two families (astronomical silicate and carbonaceous grains). This is because those processes require physical properties of dust grains, but other species of cases are not fully understood. After these processes, we re-distribute separately dust species weighted by previous distribution. We regard graphite as carbonaceous grains. We use the same physical parameters as Hirashita & Yan (2009); Kuo & Hirashita (2012), and are listed in Table 4.1. The dust size is considered by dividing the radius 3.16 Å–7.94 μm into 45 equal parts with a logarithmic bin.

4.1 Equations of galaxy evolution with dust

In this section, we show an equation for the amount of change of stars, gases (ISM), metal, and dust grains with galaxy age. We assume a one-zone model that treat only with the global physical quantities of the entire galaxy. We do not consider the outflow in our model for simplicity. Outflow is the effect that ISM being blown out of the galaxy, reducing the total mass of the galaxy (e.g., Tumlinson et al., 2017). It affects star formation by adjusting the metallicity in the galaxy, often reducing the star formation rate. We absorb this effect by star formation timescale

Table 4.1: The physical properties of dust grains in model

	X*	$g_{\rm X}$†	$m_{\rm X}$ (amu)‡	ρ (g cm^{-3})§	γ (erg cm^{-2})¶	E (dyn cm^{-2})‖
Gra	C	1.0	12	2.26	75	1.0×10^{11}
Sil	Si	0.166	28.1	2.7	25	5.4×10^{11}

* The key elememnt of dust species.
† The mass fraction of the key element X. We assume $Mg_{1.1}Fe_{0.9}SiO_4$ for the composition of silicate (Draine & Lee, 1984).
‡ The atomic mass of X.
§ The bulk density of dust grain (graphite: Draine & Lee (1984) and silicate: Draine & Li (2001)).
¶ The surface energy per unit area of grains (Chokshi et al., 1993).
‖ The Young's moduleus (Chokshi et al., 1993).

$\tau_{\rm SF}$.

The time evolution of the total stellar mass $M_*(t)$, the ISM mass $M_{\rm ISM}(t)$, the metal mass $M_Z(t)$, and the dust mass $M_{\rm d}(t)$ at an age of t are represented as following (Lisenfeld & Ferrara, 1998; Asano et al., 2013a)

$$\frac{{\rm d}M_*(t)}{{\rm d}t} = {\rm SFR}(t) - R(t), \tag{4.1}$$

$$\frac{{\rm d}M_{\rm ISM}(t)}{{\rm d}t} = -{\rm SFR}(t) + R(t) + \frac{{\rm d}M_{\rm infall}(t)}{{\rm d}t}, \tag{4.2}$$

$$\frac{{\rm d}M_Z(t)}{{\rm d}t} = -Z(t){\rm SFR}(t) + R_Z(t) + Y_Z(t), \tag{4.3}$$

$$\frac{{\rm d}M_{\rm d}(t)}{{\rm d}t} = -D(t){\rm SFR}(t) + Y_{\rm d}(t) - \frac{M_{\rm d}(t)}{\tau_{\rm SN}} + \eta\frac{M_{\rm d}(t)(1-\delta)}{\tau_{\rm acc}}, \tag{4.4}$$

where ${\rm SFR}(t)$ is the star formation rate, and $R(t)$ and $R_Z(t)$ are the total and metal mass returned by stars into ISM per unit time, respectively. ${\rm d}M_{\rm infall}/{\rm d}t$ is the infall gas rate, $Z(t) \equiv M_Z/M_{\rm ISM}$ is the metallicity, $D(t) \equiv M_{\rm d}/M_Z$ is the mass fraction of dust to metal. $Y_Z(t)$ and $Y_{\rm d}(t)$ are the metal and dust mass newly produced in the star among the ejectors of the star per unit time, respectively. η is the fraction of cold dust where the accretion process occurs, and $\tau_{\rm acc}$ and $\tau_{\rm SN}$ are the timescale of accretion and dust destruction by SN, respectively.

In this thesis, Schmidt's law (Schmidt, 1959), with a power of 1 for simplicity, is applied as SFR:

$${\rm SFR}(t) = \frac{M_{\rm ISM}(t)}{\tau_{\rm SF}}, \tag{4.5}$$

where $\tau_{\rm SF}$ is the star formation timescale. Infall rate uses zero (closed-box model) or the following equation (infall model), and it is assumed that all gases with zero metallicity fall into galaxy (Inoue, 2011):

$$\frac{{\rm d}M_{\rm infall}}{{\rm d}t} = \frac{M_{\rm infall}}{\tau_{\rm infall}}\exp\left(-\frac{t}{\tau_{\rm infall}}\right) \tag{4.6}$$

where $\tau_{\rm infall}$ is the timescale of infall, and $M_{\rm infall}$ is the total mass that flows into the galaxy by infall at $t \to \infty$. When applying the closed-box model, it is assumed

that the infall gas is zero and that all galaxy masses exist as a gas with zero metallicity (primordial gas). On the other hand, when applying the infall model, the initial gas mass is set to zero and it is assumed that all gas flows into the galaxy by infall.

$R(t)$, $R_Z(t)$, $Y_Z(t)$, and $Y_{\rm d}(t)$ are represented as

$$R(t) = \int_{m_{\rm min}(t)}^{100\ M_\odot} [m - \omega(m, Z(t-\tau_m))]\phi(m){\rm SFR}(t-\tau_m)\,{\rm d}m, \tag{4.7}$$

$$R_Z(t) = \int_{m_{\rm min}(t)}^{100\ M_\odot} [m - \omega(m, Z(t-\tau_m))]\phi(m){\rm SFR}(t-\tau_m)Z(t-\tau_m)\,{\rm d}m, \tag{4.8}$$

$$Y_Z(t) = \int_{m_{\rm min}(t)}^{100\ M_\odot} M_Z(m, Z(t-\tau_m))\phi(m){\rm SFR}(t-\tau_m)\,{\rm d}m, \tag{4.9}$$

$$Y_{\rm d}(t) = \int_{m_{\rm min}(t)}^{100\ M_\odot} m_{\rm d}(m, Z(t-\tau_m))\phi(m){\rm SFR}(t-\tau_m)\,{\rm d}m, \tag{4.10}$$

where $\phi(t)$ is the initial mass function (IMF), and we use Salpeter's IMF of Equation (2.5) with stellar mass range 0.1–100 $M_\odot$. $\omega(m, Z(t))$, $M_Z(m, Z(t))$, and $m_{\rm d}(m, Z(t))$ are the remnant mass which remains after a star explodes, and the metal mass and the dust mass newly produced by a star of mass m and metallicity $Z(t-\tau_m)$.

τ_m is the life time of star with mass m and we use following equation (Raiteri et al., 1996)

$$\log \tau_m = a_0(Z) + a_1(Z)\log m + a_2(Z)(\log m)^2, \tag{4.11}$$

$$a_0(Z) = 10.13 + 0.07547\log Z - 0.008084(\log Z)^2, \tag{4.12}$$

$$a_1(Z) = -4.424 - 0.7939\log Z - 0.1187(\log Z)^2, \tag{4.13}$$

$$a_2(Z) = 1.262 + 0.3385\log Z + 0.05417(\log Z)^2. \tag{4.14}$$

This equation was obtained by fitting the calculation results of stars with stellar mass range 0.6–120 $M_\odot$ and metallicity range 0.0004–0.05 by Padova group (Alongi et al., 1993; Bressan et al., 1993; Bertelli et al., 1994).

4.2 Dust production by stars

Dust production by AGB stars

The asymptotic giant branches (AGBs) are the after the main-sequence phase of small mass stars ($M < 8M_\odot$), they contain carbon and oxygen in the core and occur the helium and the hydrogen burning. The AGB stars produce heavier elements in ISM. The size distribution of dust grains is suggested by Winters et al. (1997), they represent the distribution as log-normal with a peak at $\sim 0.1\,\mu$m according to fitting to observed SED. Furthermore, Yasuda & Kozasa (2012) calculate dust formation with the hydrodynamical model including SiC production by AGB stars. They say that the mass distribution per unit log-size bin $a^4 f(a)$ are log-normal with a peak at 0.2–0.3 μm (see Figure 4.1). We assume that the size

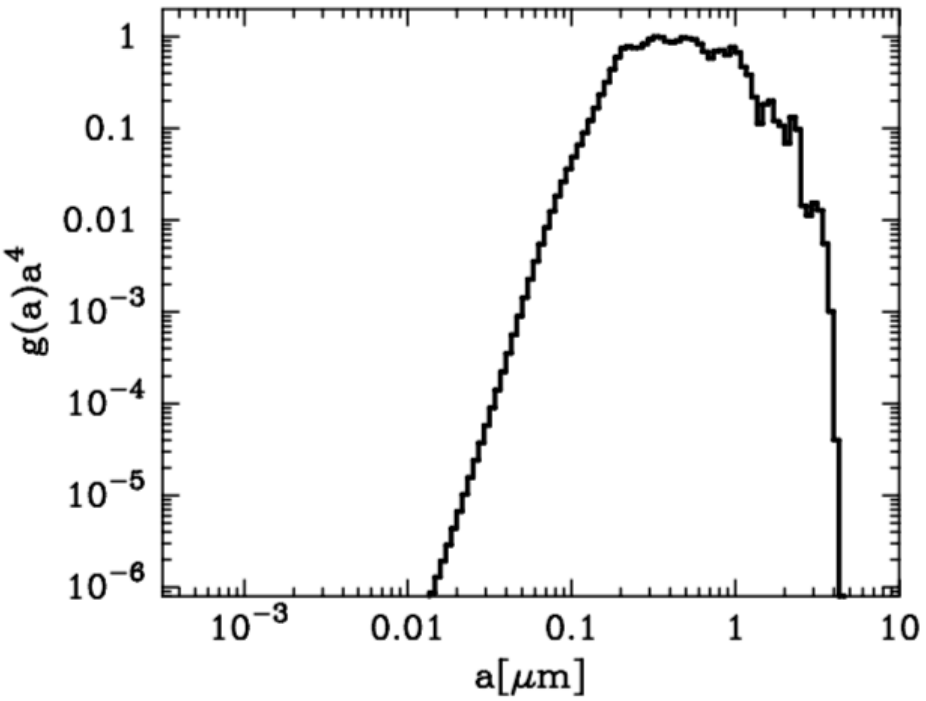

Figure 4.1: The size distribution of the SiC grains calculated by Yasuda & Kozasa (2012). The perpendicular axis represents the dust mass per logarithmic grain radius. Credit: Yasuda & Kozasa (2012)

distribution of dust grains produced by AGB stars are represented as log-normal with a peak at 0.1 μm with a standard deviation of $\sigma = 0.47$. This shape is made to reproduce Figure 4.1.

The dust mass produced by AGB stars used in this thesis is based on Zhukovska et al. (2008). They simply assume that AGB stars eject only C, Si, SiC, and Fe, and other species of dust grains are not produced by AGB stars with mass 1–7 $M_\odot$ and metallicity $Z = (0.05, 0.1, 0.3, 0.4, 0.75, 1.0)\ Z_\odot$. The remnant mass $\omega(m, Z)$ and metal mass $M_Z(m, Z)$ from AGB at stellar mass range m = 1–6 $M_\odot$ and metallicity $Z = (0.005, 0.2, 0.4, 1.0)\ Z_\odot$ are quoted from Karakas (2010). We used those data interpolated and extrapolated to the required data range.

Dust production by SNe II

The ejecta of supernova (SNe) is the region where dust grains form and be destroyed. This formation depends on the temperature of the eject, and the composition of dust grains is determined elemental synthesis in stars and the mechanism of the explosion (Nozawa et al., 2003). Furthermore, the reverse shock which is the shock reversed by high-density gas shell occurs after the SN explosion, and it destroys dust grains by sputtering (Bianchi & Schneider, 2007; Nozawa et al., 2007). The grains size distributions of several dust species before destroyed and after destroyed is shown in Figure 4.2. The figure shows that small size grains are easy to destroy, and the peak of grain size after destroyed is biased to large

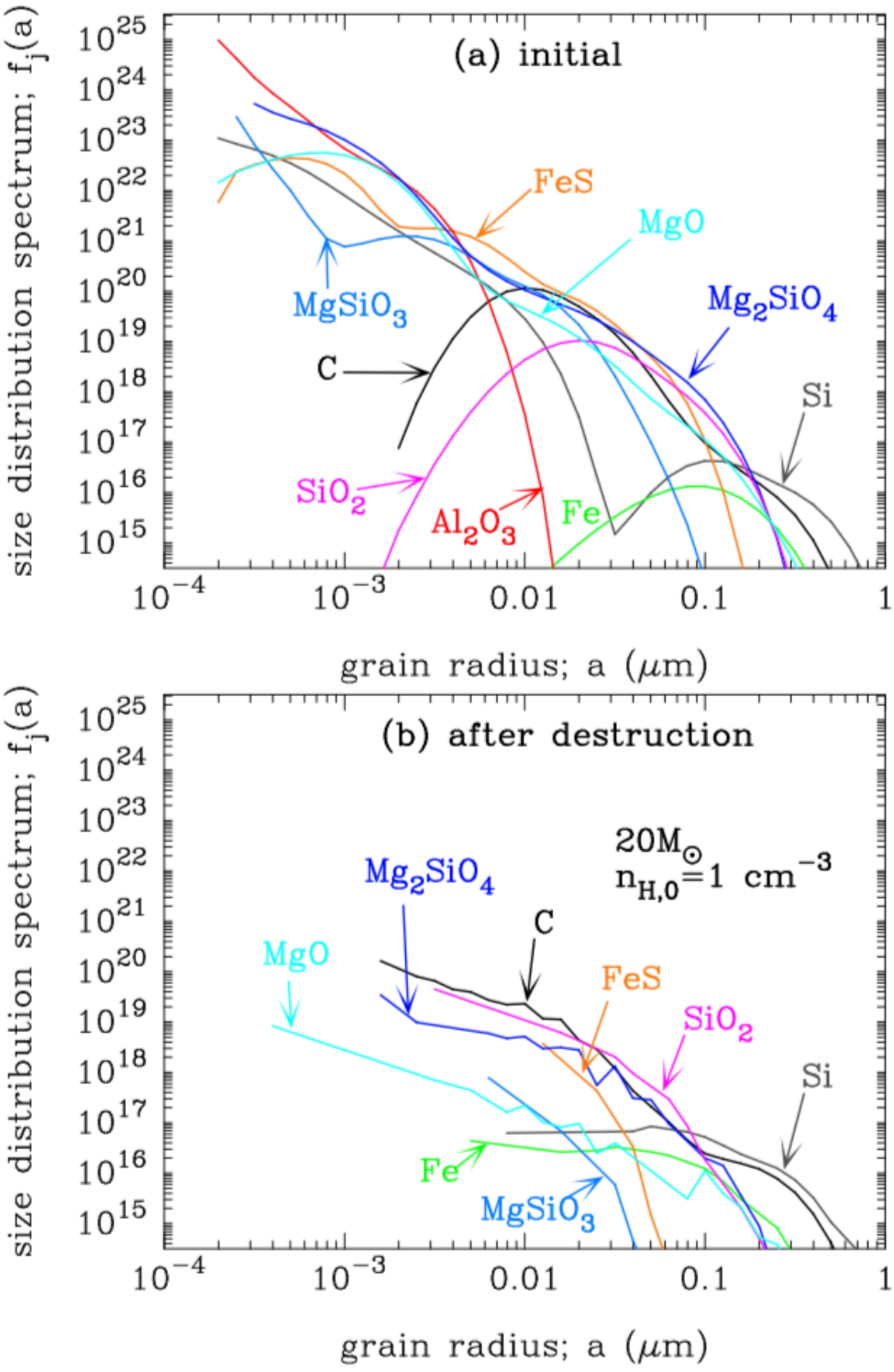

Figure 4.2: The size distribution of each dust species. (a) The initial size distribution. (b) The survived dust size distribution after destruction by reverse shock. The progenitor stellar mass is 20 $M_{\odot}$ and the hydrogen number density of the ISM is 1.0 cm^{-3}. Credit:Nozawa et al. (2007).

size (> 0.01 μm). The considering progenitor mass in Nozawa et al. (2007) is 13–30 $M_\odot$ and we adopt the data from Nozawa et al. (2007) for dust grain size distribution produced by SNe II. They consider only dust production in SNe II from zero-metallicity stars, but it has been suggested that the size distribution and composition of dust produced by the SNe II are less dependent on the metallicity of the progenitor stars (e.g., Todini & Ferrara, 2001; Kozasa et al., 2009). It is also suggested that the effect of metallicity on destruction by reverse shock is not so high at $Z = 0$ and $Z = Z_\odot$, which is 15 % (Nozawa et al., 2007).

There are two models that the core of progenitor stars are mixed and unmixed model, and both models are considered in Nozawa et al. (2007). According to Hirashita et al. (2005), the unmixed model is better fitted with the observed attenuation curve of young galaxies than the mixed model, so we adopt the unmixed model in this thesis.

The remnant mass $\omega(m, Z)$ and the metal mass $M_Z(m, Z)$ from SNe II with progenitor stellar mass range 13–40 $M_\odot$ and metallicity $Z = (0.0, 0.05, 0.2, 1.0)$ $Z_\odot$ are quoted from Kobayashi et al. (2006).

4.3 Dust destruction by SN Shock

The destruction process of dust grains in the ISM is mainly caused by SN shocks. The SN shocks not only destroy dust grains but also change the dust grain size (Nozawa et al., 2006). Yamasawa et al. (2011) introduce the formulae of this destruction,

$$f'_{\rm X}(a){\rm d}a = \int_a^\infty \eta_{\rm X}(a, a') f_{\rm X}(a'){\rm d}a' \tag{4.15}$$

where the subscripts 'X' represents the dust species, $f_{\rm X}(a){\rm d}a$ is the number density of dust grain with radii $[a, a + {\rm d}a]$ and $\eta_{\rm X}(a, a')$ is the conversion efficiency o SN sputtering defined as the ratio of number of dust grains conversion from radii $[a, a + {\rm d}a]$ to $[a', a' + {\rm d}a']$. Note that $\eta_{\rm X}(a, a') = 0$ for $a > a'$ because dust grain size dose not grow by this process. The change of number density of grain with radii $[a, a + {\rm d}a]$ after destroyed by SN shock is represented as

$${\rm d}N_{\rm d,X}(a) = \int_0^\infty \eta_{\rm X}(a, a'){\rm d}a f_{\rm X}(a'){\rm d}a' - f_{\rm X}(a){\rm d}a. \tag{4.16}$$

The dust mass density conversion ${\rm d}\rho_{\rm d,X}(a)$ is described as

$$\begin{aligned} {\rm d}\rho_{\rm d,X}(a) &= \frac{4}{3}\pi a^3 \rho {\rm d}N_{\rm d,X}(a) \\ &= \int_0^\infty \frac{4}{3}\pi a^3 \rho \eta_{\rm X}(a, a')_{\rm X}(a'){\rm d}a' - \mathcal{M}_{\rm d,X}(a){\rm d}a, \end{aligned} \tag{4.17}$$

where

$$\mathcal{M}_{\rm d,X}(a){\rm d}a = \frac{4}{3}\pi a^3 \rho f_{\rm X}(a){\rm d}a = \rho_{\rm d,X}(a), \tag{4.18}$$

is the total dust mass with radii $[a, a+\mathrm{d}a]$ before passage SN shock. The equation of the dust grain mass conversion by SN shock is expressed as

$$\frac{\mathrm{d}\rho_{\mathrm{d,X}}(a,t)}{\mathrm{d}t} = -\frac{m_{\mathrm{swept}}}{M_{\mathrm{ISM}}(t)}\gamma_{\mathrm{SN}}(t)\left[\rho_{\mathrm{d,X}}(a,t) - m(a)\int_0^\infty \eta_{\mathrm{X}}(a,a')\mathrm{d}a f_{\mathrm{X}}(a',t)\mathrm{d}a'\right], \tag{4.19}$$

where $\gamma_{\mathrm{SN}}(t)$ is the SN rate, it is calculated by (McKee, 1989b; Nozawa et al., 2006),

$$\gamma_{\mathrm{SN}}(t) = \int_{m_{\mathrm{cut}}(t)>8M_\odot}^{40M_\odot} \phi(m)\mathrm{SFR}(t-\tau_m)\mathrm{d}m. \tag{4.20}$$

The integration range is determined by the SNe can occur (Heger et al., 2003). m_{swept} is the swept mass of the ISM by SN shock, it depends on the density and metallicity of the ISM (Nozawa et al., 2006; Yamasawa et al., 2011). We use the following formulae fitted by Yamasawa et al. (2011),

$$m_{\mathrm{swept}} = 1535 n_{\mathrm{SN}}^{-0.202}\left[(Z/Z_\odot) + 0.039\right]^{-0.289}\ M_\odot. \tag{4.21}$$

4.4 Grain growth by metal accretion

The dust grains mass increase not only produced by AGB stars and SNe II but also accreted the metals in ISM onto dust grain surface in the CNM and MC phases (Inoue, 2003; Draine, 2009). For occurring this process, it needs producing adequate amount of dust grains and metals in the ISM by stellar. Thus, grain growth is not efficient process in the early galaxy, it becomes efficiently process at about 1 Gyr in general galaxies. Hirashita & Kuo (2011) formulates this process with only refractory dust grains. If dust grains evolution process is only grain growth, following equation holds,

$$\frac{\partial f_{\mathrm{X}}(a,t)}{\partial t} + \frac{\partial}{\partial a}[f_{\mathrm{X}}(a,t)\dot{a}] = 0. \tag{4.22}$$

Where $\dot{a} \equiv \mathrm{d}a/\mathrm{d}t$ is the growth rate of the grain radius and it is explained following. This rate is determined by the collision rate between the grain and the metal in ISM. We assume that the cross-section is calculated by the geometric one, do not consider the effect of the Coulomb interaction. In CNM and MC, the grains and the atoms are neutral, the ionization degree in that clouds is 10^{-6} by Yan et al. (2004). The collision rate $\mathcal{R}$ with radius a is represented as (Evans, 1993),

$$\mathcal{R} = 4\pi a^2 n_{\mathrm{X}}(t)\left(\frac{kT_{\mathrm{gas}}}{2\pi m_{\mathrm{X}}}\right)^{1/2} \tag{4.23}$$

Where $n_{\mathrm{X}}(t)$ is the number density of X in CNM or MC, T_{gas} is the gas temperature and m_{X} is the atomic mass of X listed in Table 4.1. The increasing of a grain mass with radius a is

$$\frac{\mathrm{d}m(a)}{\mathrm{d}t} = g_{\mathrm{X}}^{-1} m_{\mathrm{X}} \alpha_{\mathrm{acc}} \mathcal{R}, \tag{4.24}$$

where $g_{\rm X}$ is the mass fraction of the key element X listed in Table 4.1, $\alpha_{\rm acc}$ is the sticking coefficient of X. We assume $\alpha_{\rm acc} = 1$ for simplicity. $n_{\rm X}(t)$ is estimated as

$$n_{\rm X}(t) = \mathcal{D}\frac{\rho_{\rm ISM}^{\rm eff}}{m_{\rm X}}\left[1 - g_{\rm X}\frac{\rho_{\rm d,X}(t)}{\rho_{\rm X}(t)}\right], \tag{4.25}$$

where $\rho_{\rm ISM}^{\rm eff}$ is the average mass density of the ISM when grain growth occurs and $\mathcal{D} = M_{\rm X}(t)/M_{\rm ISM}(t)$ is the dust-to-gas-mass ratio. From the Equation (4.23)–(4.25),

$$\dot{a} \equiv \frac{{\rm d}a}{{\rm d}t} = D\frac{\alpha_{\rm acc}\rho_{\rm ISM}^{\rm eff}}{g_{\rm X}\rho}\left(\frac{kT_{\rm gas}N_{\rm A}}{2\pi m_{\rm X}}\right)^{1/2}\left[1 - g_{\rm X}\frac{\rho_{\rm d,X}(t)}{\rho_{\rm X}(t)}\right]. \tag{4.26}$$

4.5 Grain-grain collision

The dust grains in ISM have various velocity by turbulence (Koyama & Inutsuka, 2002). We consider two types of grain-grain collisions, shattering and coagulation, they are not increasing nor decreasing total grain mass in the galaxy. The processes are only change the grain size distributions. When the relative velocity between two grains is faster than the threshold velocity, shattering which is a disruption and fragmentation process occurs. On the other hand, when they have a slow relative velocity, the coagulation which is a sticking process tends to occur. We adopt the grain velocity calculated by Yan et al. (2004) in this thesis. We consider silicate and graphite as grain species while shattering and coagulation processes. And we adopt the collision which is only the same grain species each other. Furthermore, we assume that the shapes of the grain are spherical with a constant density. Here, we explain each process following subsections.

4.5.1 Shattering

Hirashita & Yan (2009) suggested that the shattering is significantly affecting the grain size distribution in ISM. The shattering process depends on the relative velocity of grains. In this thesis, we use the same parameter in Hirashita & Yan (2009), whose formulation is based on Jones et al. (1996).

The mass of grains with radii $[a, a + {\rm d}a]$ in a unit volume is defined as

$$\rho_{\rm X}(a,t){\rm d}a = m(a)f_{\rm X}(a,t){\rm d}a. \tag{4.27}$$

Considering the shattering process between two grains with radii a_1 and a_2, which are called grain 1 and 2, respectively. The time evolution of $\rho_{\rm X}(a,t){\rm d}a$ is represented as

$$\begin{aligned}\left[\frac{{\rm d}\rho_{\rm X}(a,t){\rm d}a}{{\rm d}t}\right]_{\rm shat} &= -m(a)\rho_{\rm X}(a,t){\rm d}a\int_{a_{\rm min}}^{a_{\rm max}}\alpha[m(a),m(a_1)]\rho_{\rm X}(a_1,t){\rm d}a_1{\rm d}a_1 \\ &\quad + \int_{a_{\rm min}}^{a_{\rm max}}\int_{a_{\rm min}}^{a_{\rm max}}\alpha[m(a_1),m(a_2)]\rho_{\rm X}(a_1,t){\rm d}a_1\rho_{\rm X}(a_2,t){\rm d}a_2 \\ &\quad m_{\rm shat}^{1,2}(a){\rm d}a_1{\rm d}a_2,\end{aligned} \tag{4.28}$$

and

$$\alpha[m(a_1), m(a_2)] = \begin{cases} 0 & (v_{1,2} < v_{\rm shat}) \\ \frac{\sigma_{1,2} v_{1,2}}{m(a_1) m(a_2)} & (v_{1,2} > v_{\rm shat}), \end{cases} \tag{4.29}$$

where $m^{1,2}_{\rm shat}(a)$ is the total mass of the shattered fragments of a grain 1 that the entry in size bin $[a, a + {\rm d}a]$. We assume the fragments size distribution is proportional to $a^{-3.3}$ (Hellyer, 1970; Jones et al., 1996). We assume the collisional cross-section between grain 1 and 2 is $\sigma_{1,2} = \pi(a_1 + a_2)^2$. $v_{\rm shat}$ is the threshold of shattering occurring or not, it assumed 1.2 $\mathrm{km\,s^{-1}}$ and 2.7 $\mathrm{km\,s^{-1}}$ for silicate and graphite, respectively (Jones et al., 1996). $a_{\rm min}$ and $a_{\rm max}$ are minimum and maximum radius, respectively, we assume $a_{\rm min} = 0.001$ μm and $a_{\rm max} = 0.25$ μm to reproduce the MW extinction curve Hirashita & Yan (2009).

We consider four types the directions of the grain-grain collision, thus the relative velocity is divided into four types, this treatment is the same as Jones et al. (1994) and Hirashita & Yan (2009). The relative velocities are following,

1. front collision ($v_{1,2} = v_1 + v_2$)
2. back-end collision ($v_{1,2} = |v_1 - v_2|$)
3. side collision ($v_{1,2} = v_1$)
4. another side collision ($v_{1,2} = v_2$)

where v_1 and v_2 are the velocity of grain with radii a_1 and a_2, respectively. We assume theses collisions occur in the same probability.

4.5.2 Coagulation

The coagulation tends to occur in low-temperature and high density regions. This process is The following formulae of the coagulation are also same as Hirashita & Yan (2009), whose basic ingredients are taken from Chokshi et al. (1993).

The time evolution of $\rho_{\rm X}(a,t){\rm d}a$ for coagulation is expressed as a similar form to equation (4.28),

$$\begin{aligned} \left[\frac{{\rm d}\rho_{\rm X}(a,t){\rm d}a}{{\rm d}t}\right]_{\rm coag} &= -m(a)\rho_{\rm X}(a,t){\rm d}a \int_{a_{\rm min}}^{a_{\rm max}} \alpha[m(a), m(a_1)]\rho_{\rm X}(a_1,t){\rm d}a_1 {\rm d}a_1 \\ &\quad + \int_{a_{\rm min}}^{a_{\rm max}} \int_{a_{\rm min}}^{a_{\rm max}} \alpha[m(a_1), m(a_2)]\rho_{\rm X}(a_1,t){\rm d}a_1 \rho_{\rm X}(a_2,t){\rm d}a_2 \\ &\quad m^{1,2}_{\rm coag}(a){\rm d}a_1{\rm d}a_2, \end{aligned} \tag{4.30}$$

and

$$\alpha[m(a_1), m(a_2)] = \begin{cases} 0 & (v_{1,2} > v_{\rm coag}) \\ \dfrac{\beta\sigma_{1,2} v_{1,2}}{m(a_1) m(a_2)} & (v_{1,2} < v_{\rm coag}), \end{cases} \tag{4.31}$$

where β is the sticking coefficient of dust grains and $m^{1,2}_{\rm coag}$ is the total mass of coagulated grains, and $m^{1,2}_{\rm coag}(a) = m(a)$ if $m(a - \frac{1}{2}{\rm d}a) < m_1 + m_2 < m(a + \frac{1}{2}{\rm d}a)$;

otherwise $m^{1,2}_{\rm coag}(a) = 0$. We consider the coagulation is not happened when the relative velocity is faster than the coagulation threshold relative velocity between grain 1 and 2 $v^{1,2}_{\rm coag}$. The relative velocity $v^{1,2}_{\rm coag}$ is expressed as Chokshi et al. (1993); Dominik & Tielens (1997); Yan et al. (2004); Hirashita & Yan (2009),

$$v^{1,2}_{\rm coag} = 2.14 F_{\rm stick} \left[\frac{a_1^3 + a_2^3}{(a_1+a_2)^3}\right]^{1/2} \frac{\gamma^{5/6}}{E^{1/3} R_{1,2}^{5/6} \rho^{1/2}}. \tag{4.32}$$

where a factor $F_{\rm stick} = 10$ is determined by Yan et al. (2004), $R_{1,2} \equiv a_1 a_2/(a_1+a_2)$ is the reduced radius of the grains, and γ and E are the surface energy per unit area and Young's modulus which are listed in table 4.1.

In this thesis, we consider that coagulation occur in all velocity collisions ($v_{\rm coag}$ to ∞). Because, if the threshold is not set to ∞, the size distribution does not shift to large which is adequate to reproducing the MW extinction curve.

4.6 Grain size distribution formula

In this section, we show the formula of the summary of the grain size evolution model which is discussed in this chapter. The grain mass density of the dust species d with key element X in the radius bin $[a, a+{\rm d}a]$ is defined as,

$$\rho_{\rm d,X}(a,t) \equiv m(a) f(a,t) {\rm d}a. \tag{4.33}$$

The time evolution of $\rho_{\rm d,X}$ at the age of t is formulated as

$$\begin{aligned}
\frac{{\rm d}\rho_{\rm d,X}(a,t)}{{\rm d}t} &= -\frac{\rho_{\rm d,X}(a,t)}{M_{\rm ISM}(t)} + {\rm d}Y_{\rm d,X}(a,t) \\
&- \frac{m_{\rm swept}}{M_{\rm ISM}(t)} \gamma_{\rm SN}(t) \left[\rho_{\rm d,X}(a,t) - m(a) \int_{a'} \eta(a,a') {\rm d}a f(a',t) {\rm d}a'\right] \\
&+ \eta_{\rm CNM} \left[m(a) {\rm d}a \frac{\partial f(a,t)}{\partial t}\right]_{\rm CNM} + \eta_{\rm MC} \left[m(a) {\rm d}a \frac{\partial f(a,t)}{\partial t}\right]_{\rm MC} \\
&+ \eta_{\rm WNM} \left[\frac{{\rm d}\rho_{\rm X}(a,t)}{{\rm d}t}\right]_{\rm shat,WNM} + \eta_{\rm CNM} \left[\frac{{\rm d}\rho_{\rm X}(a,t)}{{\rm d}t}\right]_{\rm shat,CNM} \\
&+ \eta_{\rm MC} \left[\frac{{\rm d}\rho_{\rm X}(a,t)}{{\rm d}t}\right]_{\rm shat,MC} + \eta_{\rm WNM} \left[\frac{{\rm d}\rho_{\rm X}(a,t)}{{\rm d}t}\right]_{\rm coag,WNM} \\
&+ \eta_{\rm CNM} \left[\frac{{\rm d}\rho_{\rm X}(a,t)}{{\rm d}t}\right]_{\rm coag,CNM} + \eta_{\rm MC} \left[\frac{{\rm d}\rho_{\rm X}(a,t)}{{\rm d}t}\right]_{\rm coag,MC}
\end{aligned} \tag{4.34}$$

where $\eta_{\rm WNM}$, $\eta_{\rm CNM}$ and $\eta_{\rm MC}$ are the mass fraction of WNM, CNM, and MC in the ISM, respectively. In right-hand size, the first term represents the reduction by astration, the second term is the ejection of dust from stellar sources. The ejection ${\rm d}Y_{\rm d,X}(a,t)$ is expressed,

$${\rm d}Y_{\rm d,X}(a,t) = \int_{m_{\rm star}=m_{\rm cu}(t)}^{100 M_\odot} m_{\rm d}[m_{\rm star}, Z(t-\tau_m), a] \phi(m_{\rm star}) {\rm SFR}(t-\tau_m) {\rm d}m_{\rm star} \tag{4.35}$$

where $\mathrm{d}m_{\mathrm{d,X}}(m_{\mathrm{star}}, Z, a)$ is the mass of grain in the radius bin $[a, a + \mathrm{d}a]$.

The third term of right-hand size in Equation (4.34) means the dust destruction by SN shocks and others represent shattering and coagulation effects each ISM phase, respectively. $\rho_{\mathrm{X}}(a, t)$ means the total mass density in radius bin $[a, a + \mathrm{d}a]$ according to the key element X. It is used in shattering and coagulation formulas because we consider the dust species are separate in silicate and graphite during the grain-grain collisions. As you can see from Equation (4.34), our model has a strong dependency on the ratio of the ISMs.

4.7 The result of dust model

Our dust model mainly have the four free parameters, star formation timescale τ_{SF}, the initial gas mass $m_{\mathrm{gas}}(t = 0)$ and the ratio of the ISM phases η_{WNM}, η_{CNM} and η_{MC}, where $\eta_{\mathrm{WNM}} + \eta_{\mathrm{WNM}} + \eta_{\mathrm{WNM}} = 1$.

We show the result of the dust model calculated with star formation timescale $\tau_{\mathrm{SF}} = 3$ Gyr and the ratio of $\eta_{\mathrm{WNM}} = 0.5$, $\eta_{\mathrm{CNM}} = 0.3$, and $\eta_{\mathrm{MC}} = 0.2$ in Figure 4.3. we determine the ratios of the ISM the same as Nozawa et al. (2007) which select

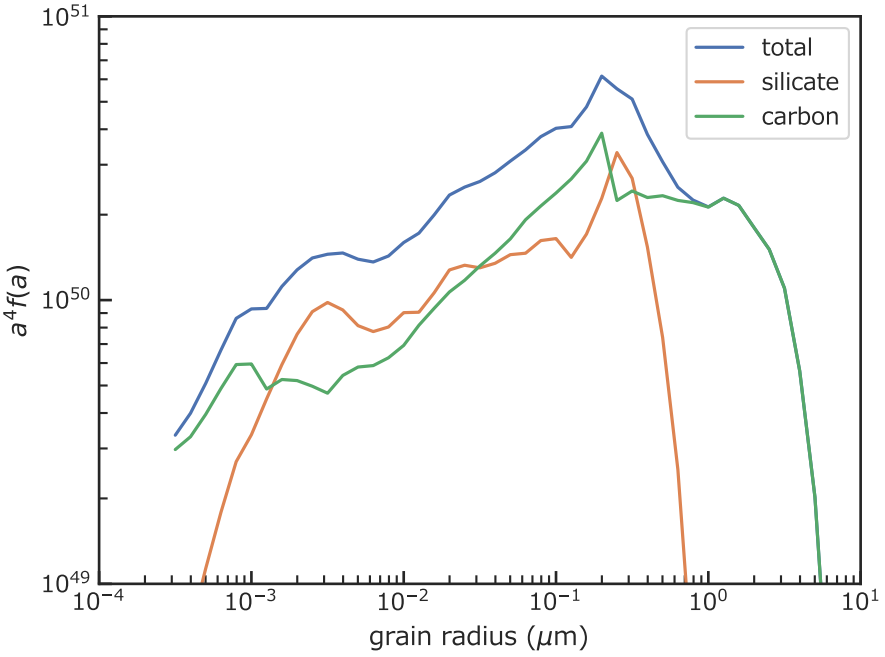

Figure 4.3: The result of dust grains mass distribution at MW model in the age of 13 Gyr. $\tau_{\mathrm{SF}} = 3$ Gyr, $\eta_{\mathrm{WNM}} = 0.5$, $\eta_{\mathrm{CNM}} = 0.3$, and $\eta_{\mathrm{MC}} = 0.2$.

the ratios reproduce to MW extinction. The perpendicular axis represents the mass distribution in the logarithmic grain radius bin. The blue curve shows total grains mass, and orange and green curves are represented silicate and carbon grains, respectively. Carbon grains exist in the range of very large radius ($a > 1\ \mu$m), and small size gains are dominated by silicate grains.

The time evolution of total grain mass distribution shows in Figure 4.4. The

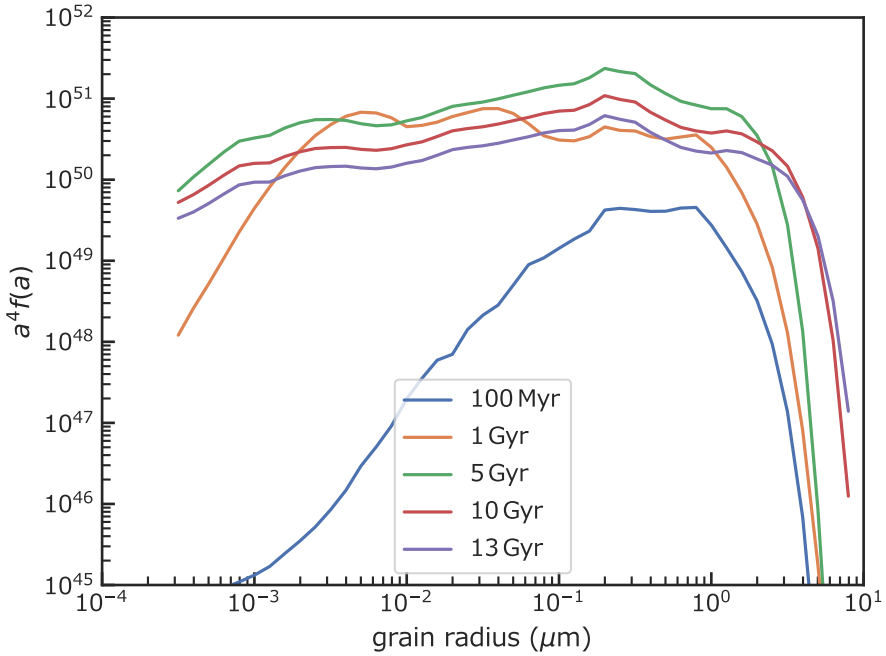

Figure 4.4: The time evolution of dust grains distribution calculated in MW like the galaxy. The colors represent according to galaxy ages.

properties are the same as Figure 4.3. At the galaxy age of 100 Myr, few amounts of grains are produced by stars. Other processes are not efficient at this age. After that, the shattering process gradually generates small grains at the age of 1 Gyr. Furthermore, accretion is an important process to increase total mass. The timescale of that process depends on metallicity Asano et al. (2013a) and there is the critical metallicity which is the grain mass increasing point. Figure 4.5 shows the time evolution of the dust-to-gas mass ratio calculated with MW properties, the switching time is at the age of 1 Gyr.

In 5 Gyr, total dust mass reaches the peak value because the star formation timescale is set to 3 Gyr; thus the star-forming decrease with the age after this 3 Gyr. The existence of this switching time is the reason for the following problem; the empirical dust model based on the observation of nearby galaxies for calculating galaxy SED would be misleading. For example, if we extrapolate the grain mass by nearby galaxy amounts in Figure 4.5, we might overestimate the grain mass. Consequently, we are quite required to establish a SED model based on the theory of dust evolution. In this thesis, we adopt this result of grains size distribution (showed in Figure 4.3 and 4.4) for our SED model.

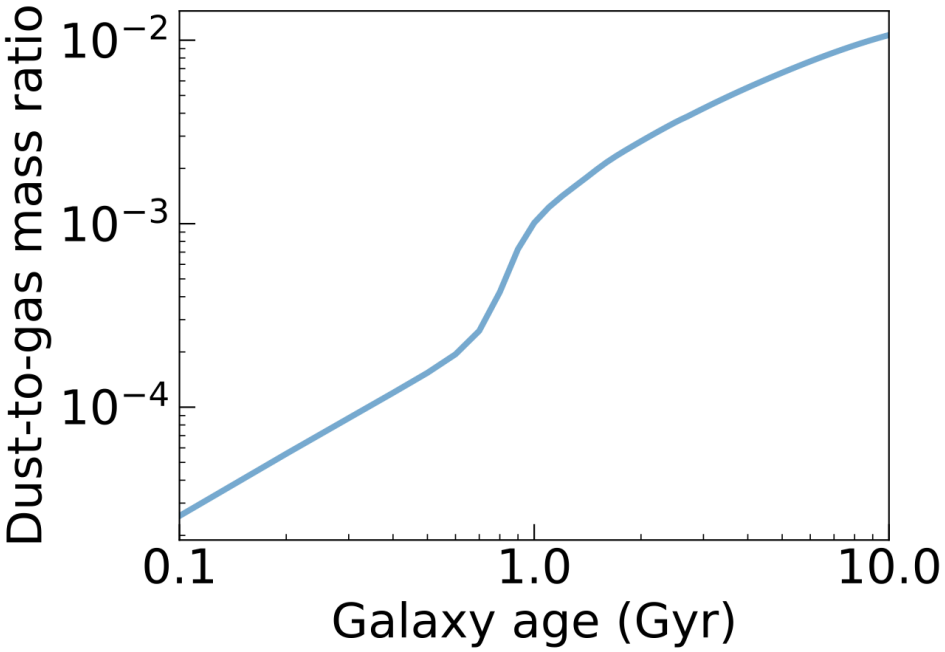

Figure 4.5: Time evolution of dust-to-gas mass ratio with the properties of MW like galaxy.

Chapter 5

Construction of galaxy spectral energy distribution

The spectral energy source in the galaxy is divided into three-component (stellar, gas, and dust). Figure 5.1 is an overview of the construction of spectral energy distribution by synthesis technique. In our model, the wavelength range is 10 Å-99.2 cm divided by logarithmic bins into 2700 equal parts. However, in the range below 912 Å, the radiation is set to zero due to the Lyman break. The galaxy SED is construct following process. Firstly, Spectrum emitted by stars is calculated by simple stellar population (SSP) method. Secondary, the dust size distribution is determined by several method (in most model use the MRN distribution of Equation (3.30), and our model use chemical evolution model mentioned in §4) and calculate the dust properties. Thirdly, the dust attenuation of stellar radiation by radiative transfer method with the dust properties calculated in second step. Fourthly, the dust emission is calculated by stochastic heating method. Lastly, the stellar SED, the attenuation curve, and the dust emission which are calculated above steps, are combined to the galaxy SED. In this chapter, we explain how we treat each component in our SED model.

5.1 Stellar SED model

The emitting energy from star is the most dominant component in galaxy. Stellar emission dose not only detected directly but also becomes the source of the heating dust grain. Thus, when we want to get galaxy SED, we need to get stellar SED. In our SED model, we use the method same as PÉGASE (Fioc & Rocca-Volmerange, 1999, 2019) for stellar SED. PÉGASE is the SED code based on a SSP developed by Fioc & Rocca-Volmerange (1999). As of 2019, PÉGASE are released three versions. The newest version PÉGASE.3 (Fioc & Rocca-Volmerange, 2019) can calculate the dust stochastic heating, in this thesis, we use the result of this version for comparison with our SED model. PÉGASE.2 (Fioc & Rocca-Volmerange, 1999) can calculate the galaxy SED with the simple setting of star formation history, we adopt the result of that with no-dust attenuation mode as stellar SEDs.

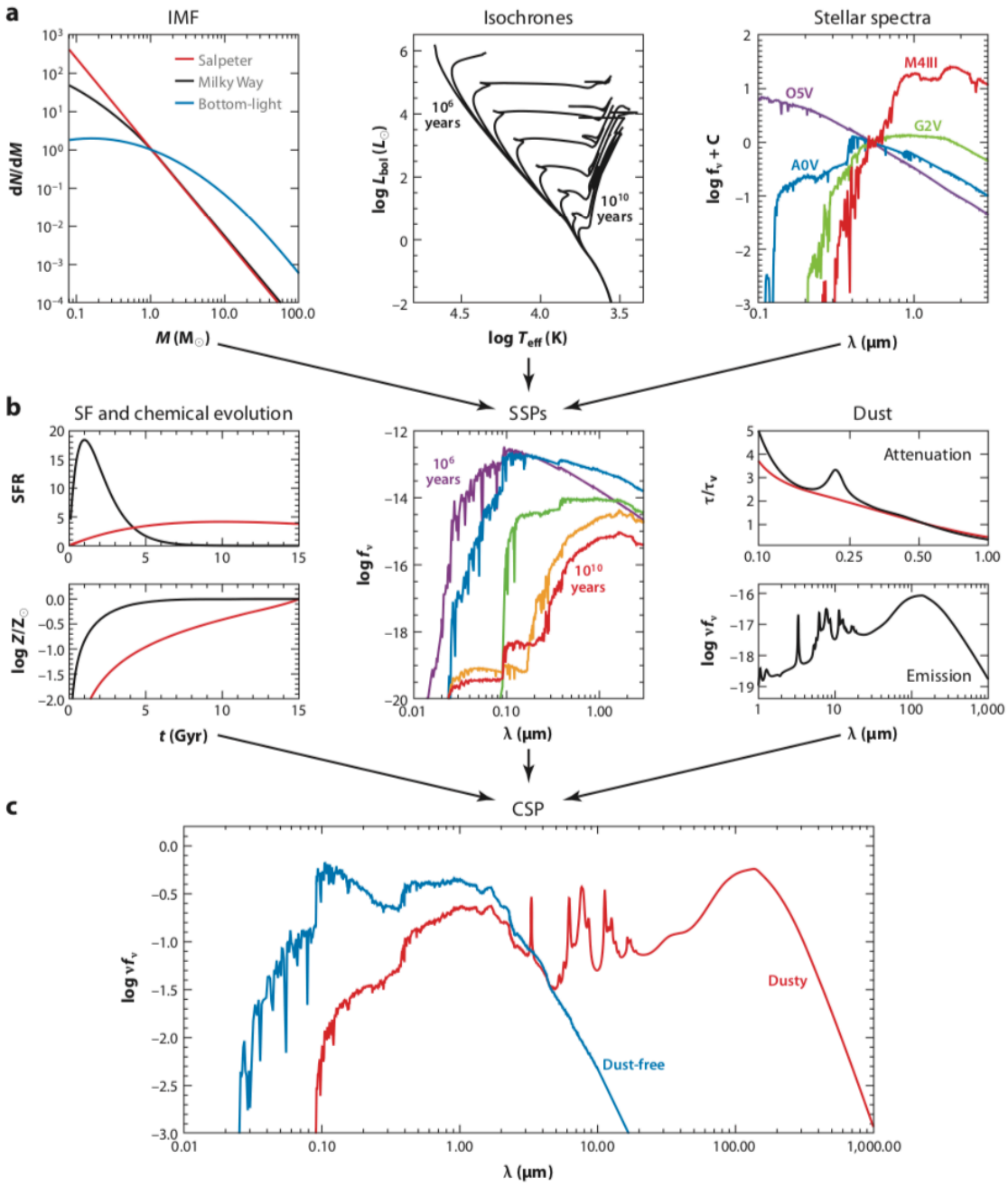

Figure 5.1: The overview of generating SED from the simple stellar population. The upper three panels are ingredients of the emission of SSPs. Credit: Conroy (2013)

5.1.1 Simple stellar populations

PÉGASE estimates the stellar emission by SSP method. The SSP consists of the stars which have the same initial chemical composition and created by an instantaneous star-forming. Considering the SSP with the initial chemical composition $\{\chi_0\} := \{\chi_0(\mathrm{H}), \chi_0(\mathrm{He})\}$, the monochromatic luminosity per unit wavelength is represented as

$$L_\lambda^{\mathrm{SSP}}(t, \{\chi_0\}) = \int_{m_{\min}}^{m_{\max}(t)} L_\lambda^{\mathrm{star}}(T_{\mathrm{eff}}(t,m), \log g(t,m), \{\chi_0\})\phi(m)\mathrm{d}(\ln m), \quad (5.1)$$

where t is the age, λ is the wavelength and $L_\lambda^{\mathrm{star}}(m, t, \chi_0)$ is the monochromatic luminosity of stellar with the mass in the interval $[m, m + \mathrm{d}m]$. The lower limit of integration $m_{\min}$ is determined for the hydrogen burning limit (we uses 0.1 $M_\odot$), and $m_{\max}(t)$ is the upper limit of stellar mass at an age of t. T_{eff} is the effective temperature and g is the surface gravity of stellar with mass of m. The luminosity of stellar $L_\lambda^{\mathrm{star}}$ is computed by multiplying stellar spectra with isochrons.

Isochrons

The isochrons are written in the Hertzsprung-Russell (HR) diagram and determined the relation between effective T_{eff}, surface gravity $\log g$, and stellar mass m for a given time t and metallicity Z from the hydrogen burning limit (0.1 $M_\odot$) to the maximum stellar mass limit (100 $M_\odot$). It is showed in upper middle panel of Figure 5.1. A lot of major isochron tables cover a wide range of age, chemical composition, and evolutionary phases, e.g., the Padova (Bressan et al., 1993; Fagotto et al., 1994b,c,a; Girardi et al., 1996) and the BaSTI (Pietrinferni et al., 2004; Cordier et al., 2007). The Geneva models (Schaller et al., 1992; Meynet & Maeder, 2000) include the Wolf-Rayet (WR) phase but do not include low-mass stars. Because of emission of low-mass stars is a few ratio ($\sim 1\%$) to the light of the stellar population, contribution of low-mass stars are negligible. Default PÉGASE setting uses basically classical Padova tracks (Bressan et al., 1993; Fagotto et al., 1994b,c,a; Girardi et al., 1996), from $Z = 0.0001$ up to $Z = 0.1$.

Stellar spectra

To calculate SSPs by Equation (5.1), PÉGASE uses the stellar spectrum libraries. In the case that an effective temperature is $T_{\mathrm{eff}} < 50,000$ K, they use BaSeL's spectra which is based on the theoretical model (Kurucz, 1979) and corrected by Lejeune et al. (1997). For the high effective temperature stellar ($T_{\mathrm{eff}} > 50,000$ K), they use Clegg & Middlemass (1987).

Stellar spectrum contains SSP luminosity with various metallicities and ages. It is represented as

$$L_\lambda(t) = \int_{t'=0}^{t'=t} \int_{Z=0}^{Z=Z\max} \mathrm{SFR}(t-t')P(t-t', Z)L_\lambda^{\mathrm{SSP}}(t', Z[t-t'])\ \mathrm{d}t'\mathrm{d}Z, \quad (5.2)$$

where $\mathrm{SFR}(t-t')$ is star formation rate (SFR), $P(t-t', Z)$ is the time-dependent metallicity distribution function. PÉGASE.2 can select several SFR and initial

mass function (IMF), we select the star formation rate which is proportional to a power of the mass of gas (§2.1.1),

$$\mathrm{SFR}(t) = \frac{M^p_{\mathrm{gas}}(t)}{\tau_{\mathrm{SF}}}. \tag{5.3}$$

where τ_{SF} is the star formation timescale (In the MW model, we adopt $\tau_{\mathrm{SF}} = 3\ \mathrm{Myr}/M_\odot$, and we assume $p = 1$ for simplicity). We use the Salpeter IMF expressed as Equation (2.5).

We show stellar spectrum of Milky Way like galaxy calculated by above method in Figure 5.2, $< 5\ \mu$m range emission is calculated by extrapolation. The stellar spectra mainly dominate UV region, IR region light emitted by stars is very weak and so swamped in the dust emission. For SED model, the stellar spectrum is attenuated by dust grains, and combined with dust grains radiation.

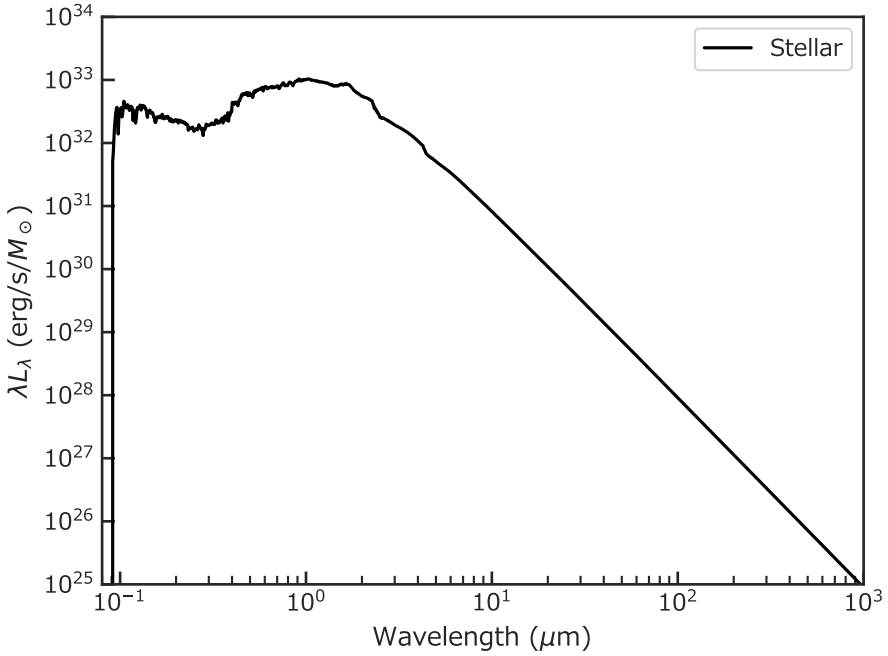

Figure 5.2: Stellar spectrum calculated by PÉGASE.2 method with Milky Way model.

5.2 Dust properties

5.2.1 Mega grain approximation

Three-dimensional radiative transfer is typically calculated for treating the attenuation by dust grains, but it needs substantial computing costs. Neufeld (1991); Hobson & Padman (1993) introduce the method that solves the radiative transfer

with mega grain approximation (MGA) in a one-dimensional plain parallel galaxy (Varosi & Dwek, 1999; Inoue, 2005). In MGA, we treat the dusty region as a kpc scale a huge grain called mega grain and considered absorption and scattering the same as typical grains by effective optical properties.

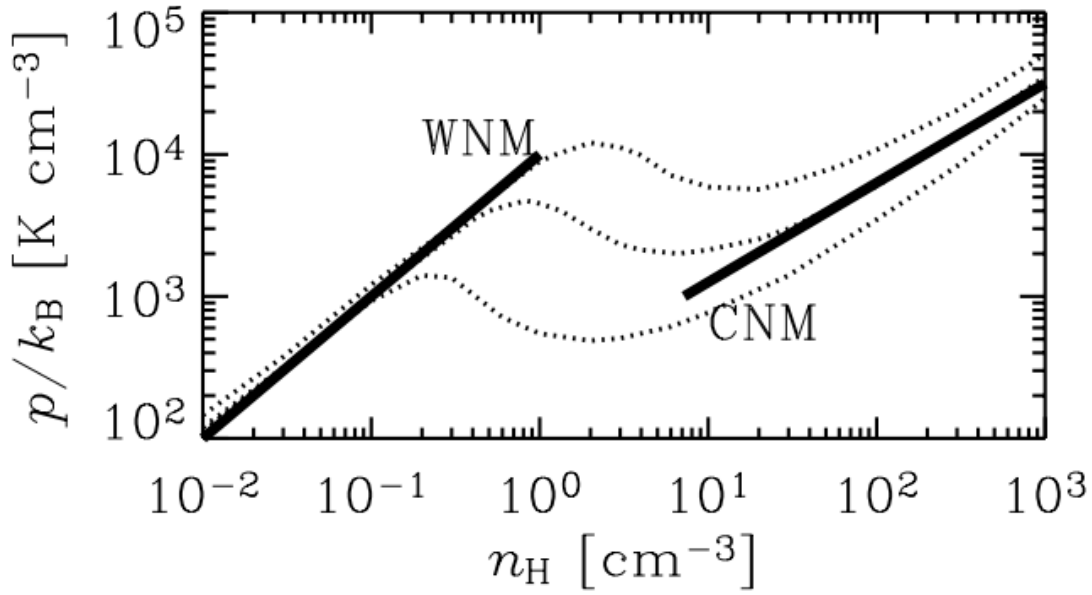

Figure 5.3: The relation of thermal pressure and hydrogen number density by Inoue 2005. The dotted curve shows the equilibrium points in the ISM of the MW. The difference of three-line is the distance from the galactic center, the top is 3 kpc, the middle is 8.5 kpc and bottom is 15 kpc. The solid lines are approximate relations of two stable phases (WNM and CNM). Credit: Inoue (2005)

Assuming the thermal and chemical equilibrium with temperature $T < 10^4\,\mathrm{K}$, the ISM is represented by two phases like Figure 5.3 (e.g., Wolfire et al., 2003a; Koyama & Inutsuka, 2000). The high temperature and low-density phase are called warm neutral medium (WNM), and low temperature and dense phase are called cold neutral medium (CNM). The relation of the thermal pressure with hydrogen density is expressed by fitting the phase diagram as (Inoue, 2005),

$$\frac{p/k_\mathrm{B}}{10^4\,\mathrm{K\,cm^{-3}}} = \frac{n_\mathrm{H,wnm}}{1\,\mathrm{cm^{-3}}} \quad \text{(WNM)}, \tag{5.4}$$

$$\frac{p/k_\mathrm{B}}{10^{4.5}\,\mathrm{K\,cm^{-3}}} = \left(\frac{n_\mathrm{H,cnm}}{10^3\,\mathrm{cm^{-3}}}\right)^{0.7} \quad \text{(CNM)}. \tag{5.5}$$

Where, p is pressure, k_B is Boltzmann constant and $n_\mathrm{H,wnm}$ and $n_\mathrm{H,cnm}$ are hydrogen number density of WNM and CNM respectively. In this paper, WNM and CNM are regarded as the interclump medium (ICM) and clumps, respectively. The clumps are assumed the core of molecular clouds and the birth clouds of young stellar. The size of clumps can be calculated by assuming to be self gravitation

$$r_\mathrm{cl} = \frac{1}{\rho_\mathrm{cl}}\sqrt{\frac{15p}{4\pi G}} = \frac{1}{\mu m_\mathrm{p} n_\mathrm{H,cnm}}\sqrt{\frac{15p}{4\pi G}} \sim 10.4\ \mathrm{pc}, \tag{5.6}$$

where G is gravitational constant, $\rho_{\rm cl} = \mu m_{\rm p} n_{\rm H,cnm}$ is the density of clump, $\mu = 1.4$ is the mean atomic weight and $m_{\rm p} = 1.673 \times 10^{-24}$ g is the proton mass.

We assume all clumps in galaxy are sphere with the radius $r_{\rm cl}$ and the density $\rho_{\rm cl}$ given by Equation (5.6). In addition to this clumps exist into the WNM (interclump medium) with the gas density $\rho_{\rm icm} = \mu m_{\rm p} n_{\rm H,wnm}$. The relative optical depth of clump with interclump medium is

$$\tau_{\rm cl} = (\rho_{\rm cl} - \rho_{\rm icm}) k_{\rm d} D r_{\rm cl}. \tag{5.7}$$

Where $k_{\rm d}$ is the dust opacity and D is dust-to-gas mass ratio. The interaction (absorption and scattering) probability of the sphere with optical depth τ with parallel light is represented by

$$P_{\rm int}(\tau) = 1 - \frac{1}{2\tau^2} + \left(\frac{1}{\tau} + \frac{1}{2\tau^2} \right) e^{-2\tau}. \tag{5.8}$$

We can write the extinction coefficient per unit length of the medium by clump

$$\kappa_{\rm mg} = n_{\rm cl} \pi r_{\rm cl}^2 P_{\rm int}(\tau_{\rm cl}) = \frac{3 f_{\rm cl}}{4 r_{\rm cl}} P_{\rm int}(\tau_{\rm cl}), \tag{5.9}$$

were $n_{\rm cl}$ is the clump number density and $f_{\rm cl} = (n_{\rm H} - n_{\rm H,wnm})/(n_{\rm H,cnm} - n_{\rm H,wnm})$ is clump filling fraction. Thus, the effective extinction coefficient is represented by adding the extinction coefficient of interclump medium $\kappa_{\rm icm} = k_{\rm d} D \rho_{\rm icm}$ to $\kappa_{\rm mg}$

$$\kappa_{\rm eff} = \kappa_{\rm mg} + \kappa_{\rm icm}. \tag{5.10}$$

The scattering albedo of clump $\omega_{\rm cl}$ is represented by

$$\omega_{\rm cl} = \omega_{\rm d} P_{\rm esc}(\tau_{\rm cl}, \omega_{\rm d}), \tag{5.11}$$

where $\omega_{\rm d}$ is the scattering albedo of normal dust grain and

$$P_{\rm esc}(\tau, \omega) = \frac{\frac{3}{4\tau} P_{\rm int}(\tau)}{1 - \omega \left[1 - \frac{3}{4\tau} P_{\rm int}(\tau) \right]} \tag{5.12}$$

is the photon escape probability from a sphere grain. Thus, the effective albedo $\omega_{\rm eff}$ is written as

$$\omega_{\rm eff} = \frac{\omega_{\rm cl} \kappa_{\rm mg} + \omega_{\rm d} \kappa_{\rm icm}}{\kappa_{\rm eff}}. \tag{5.13}$$

The asymmetry parameter of clump $g_{\rm cl}$ is represented by

$$g_{\rm cl}(\tau_{\rm cl}, \omega_{\rm d}, g_{\rm d}) = g_{\rm d} - C \left(1 - \frac{1 + e^{-B/A}}{1 + e^{(\tau_{\rm cl} - B)/A}} \right) \tag{5.14}$$

where

$$A \equiv 1.5 + 4 g_{\rm d}^3 + 2 \omega_{\rm d} \sqrt{g_{\rm d}} \exp(-5 g_{\rm d}) \tag{5.15}$$

$$B \equiv 2 - g_{\rm d}(1 - g_{\rm d}) - 2 \omega_{\rm d} g_{\rm d} \tag{5.16}$$

$$C \equiv \frac{1}{3 - \sqrt{2 g_{\rm d}} - 2 \omega_{\rm d} g_{\rm d} (1 - g_{\rm g})}. \tag{5.17}$$

This equation is analytical fitting formula of Monte Carlo simulation results in Varosi & Dwek (1999). Thus, the effective asymmetry parameter is

$$g_{\rm eff} = \frac{g_{\rm cl} \kappa_{\rm mg} + g_{\rm d} \kappa_{\rm icm}}{\kappa_{\rm eff}}. \tag{5.18}$$

5.3 Radiative transfer in a one-dimensional plane parallel galaxy

We suppose following approximation for solving radiative transfer

1. We suppose a one-dimensional plane parallel galaxy (Inoue, 2005).
2. z axis is set to perpendicular direction of galaxy plane and $z = 0$ is the center of the galaxy. we assume mirror boundary.
3. Galaxy has two types of the disk (disk1 and disk2) set to be the same center. Disk 1 contains gas, dust and young stellar with the thickness $2h_{\rm d}$. Another contains only diffused old stellar with the scale height $h_{\rm s}$.
4. In disk1, the density of gas, dust and stellar is constant.

Figure 5.4 is schematic view of our galaxy geometry.

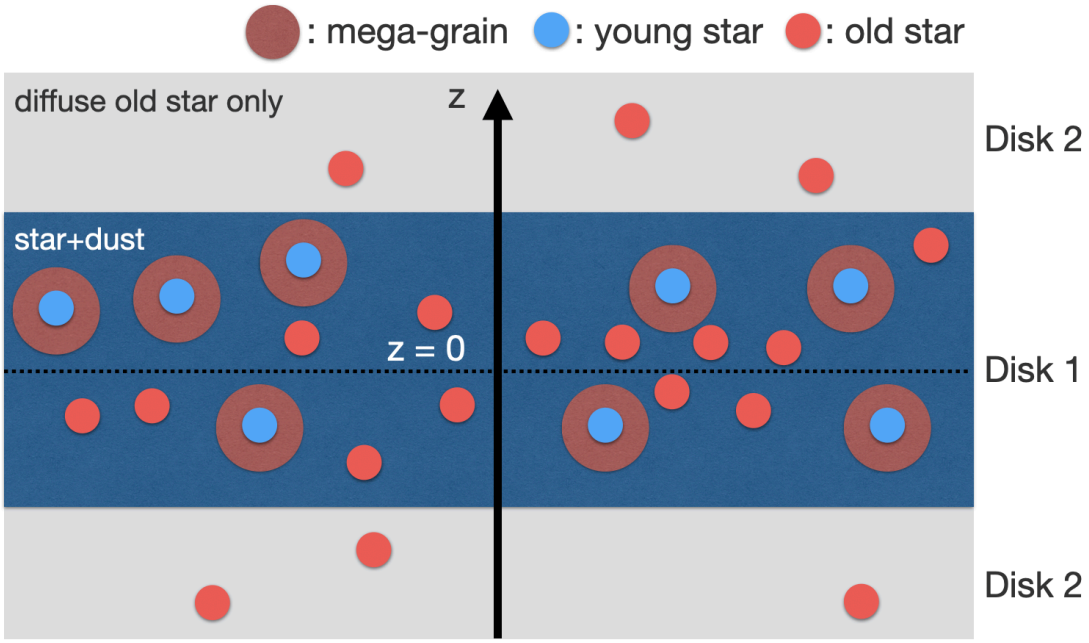

Figure 5.4: The schematic view of galaxy's geometry. The density of the gas, mega grain and stars do not depend on radial direction. Gas, mega grain and young star are contained only disk1 and independent to the z-axis. Disk2 contains an only diffuse old star.

Optical depth τ is defined as

$$\mathrm{d}\tau = -\kappa_{\rm eff}\mathrm{d}z \tag{5.19}$$

with $\tau = 0$ at $z = h_{\rm d}$ and $\tau = \kappa_{\rm eff}h_{\rm d}$ at $z = 0$. In above condition, radiative transfer equation is

$$\mu\frac{\mathrm{d}I(\tau,\mu)}{\mathrm{d}\tau} = -I(\tau,\mu) + S(\tau,\mu), \tag{5.20}$$

where I is the specific intensity, $mu \equiv 1/\cos\theta$ and θ is the angle between the ray and z axis. S is the source function

$$S(\tau, \mu) = \frac{\eta_*(\tau)}{\kappa_{\rm eff}} + \omega_{\rm eff} \int_{-1}^{1} I(\tau, \mu')\Phi(g_{\rm eff}, \mu, \mu')\mathrm{d}\mu'. \tag{5.21}$$

Where Φ is the scattering phase function, we assume the Henyey-Greenstein phase function (Henyey & Greenstein, 1941)

$$\Phi_{\rm HG} = \frac{1}{2}\frac{1-g^2}{(1+g^2-2g\cos\theta)^{3/2}}. \tag{5.22}$$

η_* is the stellar emissivity, it is discussed in following section.

The boundary condition is

$$I(\tau = \kappa_{\rm eff} h_{\rm d}, \mu) = I(\tau = \kappa_{\rm eff} h_{\rm d}, -\mu) \quad (\text{at } z = 0), \tag{5.23}$$

$$I(\tau = 0, \mu < 0) = -\frac{I_*}{\mu} \quad (\text{at } z = h_{\rm d}), \tag{5.24}$$

where

$$I_* \equiv \int_{h_{\rm d}}^{\infty} \eta_*(z)\mathrm{d}z \tag{5.25}$$

The density of the gas, mega grain and stars do not depend on radial direction. Gas, mega grain and young star are contained only disk1 and independent to the z-axis. Disk2 contains an only diffuse old star.

5.3.1 Stellar emissivity

We separate the emissivity region into two types. One is containing the young star and the mega grain and the other is containing only diffused old stellar. Because the stellar is formed in only the molecular cloud. According to Inoue (2005), the attenuation of the result of radiative transfer depends on the threshold of young age $t_{\rm y}$ and the attenuation at 100 Myr is most fitted to Milky Way attenuation. Thus, in this paper, we use $t_{\rm y} = 100$ Myr.

We normalize the intrinsic emissivity as

$$\int_{-\infty}^{\infty} \eta_*(z)\mathrm{d}z = 1. \tag{5.26}$$

Young stellar emissivity

We suppose that the young star and the dust grains are distributed uniformly in the disk1 region. Disk2 region does not have young stars and dust grains, they contains only old stars.

The intrinsic emissivity of young stellar is $1/2h_{\rm d}$ for $|z| < h_{\rm d}$ and 0 for $|z| > h_{\rm d}$. After the photon emitted by young stellar, it is absorbed and scattered by dust grains around them. The photons escape from isotropic dust grain by the

probability of Equation (5.12). We consider the above reasons and define stellar emissivity as

$$\eta_*(z) = \begin{cases} \frac{P_{\rm esc}(\tau_{\rm cl},\omega_{\rm cl})}{2h_{\rm d}} & (\text{for } |z| < h_{\rm d}) \\ 0 & (\text{for } |z| > h_{\rm d}). \end{cases} \tag{5.27}$$

In this case, $I_* = 0$.

Old stellar emissivity

Old stars are assumed that be exponential diffused distribution along the z-axis. The scale hight is $h_{\rm s} = h_{\rm d}/\xi$. Where ξ is a fraction of the disk2 to disk1. Thus, emissivity of old stellar is

$$\eta_*(z) = \frac{\xi e^{-\xi|z|/h_{\rm d}}}{2h_{\rm d}}. \tag{5.28}$$

In this case, $I_* = e^{-\xi}/2$

5.4 Dust radiation

Dust grains absorb and scatter UV photon and re-emit photon at IR, the energy of the emitted photon is dependent on the temperature of the dust grain. Large size dust grains have equilibrium temperature. On the other hand, very small dust grains are stochastically heated, and they can not have equilibrium temperature (Draine & Anderson, 1985; Guhathakurta & Draine, 1989; Li & Draine, 2001; Draine & Li, 2001; Takeuchi et al., 2003; Krugel, 2003; Draine & Li, 2007; Horn et al., 2007).There are two reasons,

1. the specific heat capacity of small dust is very small.
2. the interval time of photon collision to dust is very long.

5.4.1 Dust stochastic heating

The rate of a dust grain absorbs photon with energy $E \sim E+{\rm d}E$ and time $t \sim t+{\rm d}t$ is

$${\rm d}p(a,\lambda) = \pi a^2 Q_{\rm abs}(a,\lambda) u_\lambda \frac{\lambda^3}{h_{\rm p}^2 c} {\rm d}E{\rm d}t. \tag{5.29}$$

Where, a is the dust grain radius, u_λ is the mean energy density per wavelength in the galaxy, $h_{\rm p}$ is the Plank constant and c is the light velocity. In Equation (5.29), when the time interval ${\rm d}t$ is adequately small, ${\rm d}p$ becomes photon absorbed probability per unit time. For simplicity, we consider that the energy of the absorbed photon is used to instantaneously heat the grain, it represented by

$$E(T+\Delta T) = E(T) + \frac{h_{\rm p} c}{\lambda}. \tag{5.30}$$

where $E(T)$ is the internal energy of dust grain at temperature T and ΔT is the increment of temperature.

Table 5.1: Physical quantities relating to N

Dust species	ρ [g/cm^3]*	M [g/mol]†
Graphite	2.26‡	12.0
Silicate	3.50§	172.25

* mass density
† molar mass
‡ Draine & Lee (1984)
§ Li & Draine (2001)

Internal energy

The internal energy of dust is calculated by the Debye model in Li & Draine (2001). The internal energy of silicate grains and graphite grains are represented by

$$E_{\rm sil}(T) = (N_{\rm atom}-2)k_{\rm B}\left[2f_2\left(\frac{T}{500\,{\rm K}}\right)+f_3\left(\frac{T}{1500\,{\rm K}}\right)\right], \tag{5.31}$$

$$E_{\rm gra}(T) = (N_{\rm C}-2)k_{\rm B}\left[f_2\left(\frac{T}{863\,{\rm K}}\right)+2f_2\left(\frac{T}{2504\,{\rm K}}\right)\right], \tag{5.32}$$

where

$$f_n(x) \equiv n\int_0^1 \frac{y^n {\rm d}y}{\exp(y/x)-1}, \tag{5.33}$$

$$\tag{5.34}$$

the subscripts 'sil' and 'gra' represent the silicate and graphite grains, respectively. Equation (5.34) is n dimensional Debye function. According to Draine & Li (2001), internal energy of silicate is reproduced by 2/3 of the vibrational modes are distributed according to a Debye model with $n = 2$ and Debye temperature $\Theta = 500\,{\rm K}$, and 1/3 of the modes are described by a Debye model with $n = 3$ and $\Theta = 1500\,{\rm K}$. The internal energy of graphite grains is represented by $N_{\rm gra}-2$ out-of-plane modes and $2(N_{\rm gra}-2)$ in-plane modes.

$N_{\rm atom}$ and $N_{\rm gra}$ are the number of atoms and carbon atoms in a dust grain, respectively. The number of atoms N calculated by

$$N = \frac{\frac{4}{3}\pi a^3 \rho N_{\rm A}}{M} \tag{5.35}$$

where ρ is the mass density, M is the mass number and $N_{\rm A}$ is the Avogadoro constant. These values are listed in table 5.1.

You can see from Figure 5.5, the value of internal energy depend on the dust grain radius, but the shape of that is independent of dust radius. The difference in the internal energy of silicate and graphite grains is shown in Figure 5.6. In low and middle-temperature region ($T < 1,000$ K), silicate grains have large internal energy than graphite grains, thus graphite tend to spread broad temperature range in the stochastic heating situation.

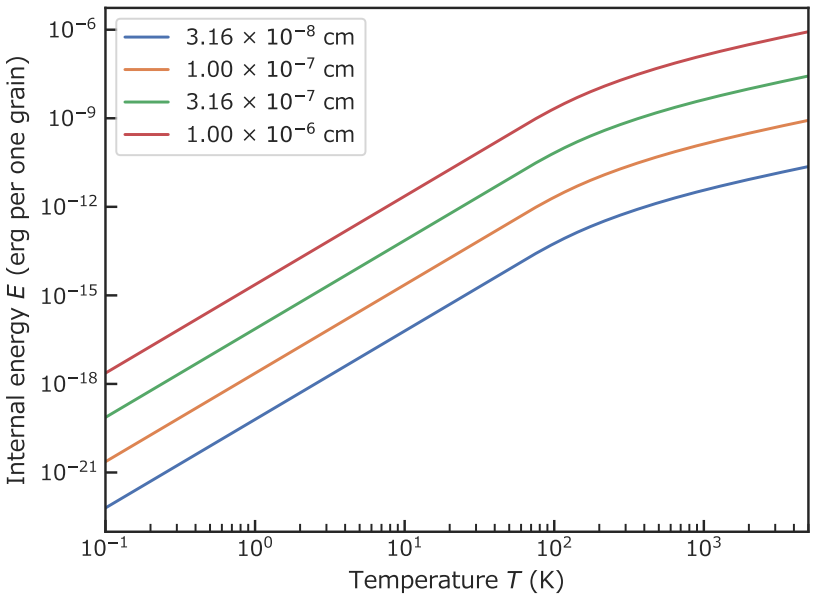

Figure 5.5: The internal energy of one silicate dust grain. The blue, orange, green and red curve shows $3.16 \times 10^{-8}, 1.00 \times 10^{-7}, 3.16 \times 10^{-7}, 1.00 \times 10^{-6}$ cm dust grains, respectively.

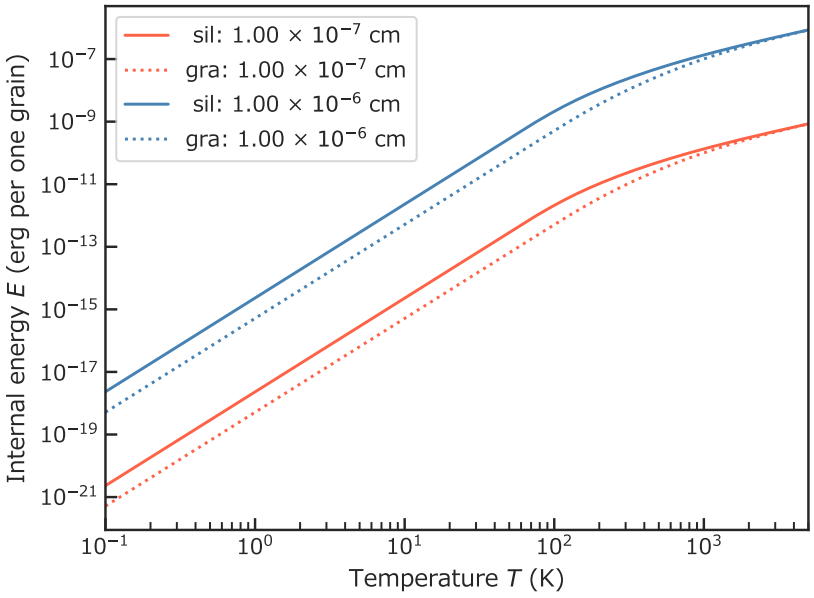

Figure 5.6: The internal energy of silicate and graphite one grain. Solid curves are silicate grains and dotted curves are graphite grain, and the difference of color represent dust grain radius (orange: 1.00×10^{-7} cm and blue: 1.00×10^{-6} cm).

In PAH grains case, we consider C-C bond modes is same as graphite and C-H bond modes component is added to Equation (5.32),

$$E_{\rm pah}(T) = E_{\rm gra} + \frac{\rm H}{\rm C} N_{\rm C} \sum_{j=1}^{3} \left(\frac{h_{\rm p}\nu_j}{\exp(h_{\rm p}\nu_j/k_{\rm B}T) - 1} \right) \tag{5.36}$$

the index j represent the C-H out-of-plane bending modes ($\nu_1/c = 886\,{\rm cm}^{-1}$), in-plane bending modes ($\nu_2/c = 1161\,{\rm cm}^{-1}$) and stretching modes ($\nu_3/c = 3030\,{\rm cm}^{-1}$), respectively. H/C is the hydrogen to carbon ratio, and we assume it following empirical value (Li & Draine, 2001).

$$\frac{\rm H}{\rm C} = \begin{cases} 0.5 & (N_{\rm C} < 25) \\ \frac{0.5}{\sqrt{N_{\rm C}/25}} & (25 < N_{\rm C} < 100) \\ 0.25 & (N_{\rm C} > 100) \end{cases} \tag{5.37}$$

The specific heat capacity of silicate $C_{\rm sil}$, graphite $C_{\rm gra}$ and PAH $C_{\rm pah}$ are

$$C_{\rm sil}(T) = (N_{\rm atom} - 2)k_{\rm B} \left[2f_2' \left(\frac{T}{500\,{\rm K}} \right) + f_3' \left(\frac{T}{1500\,{\rm K}} \right) \right], \tag{5.38}$$

$$C_{\rm gra}(T) = (N_{\rm C} - 2)k_{\rm B} \left[f_2' \left(\frac{T}{863\,{\rm K}} \right) + 2f_2' \left(\frac{T}{2504\,{\rm K}} \right) \right], \tag{5.39}$$

$$C_{\rm pah}(T) = C_{\rm gra} + \frac{\rm H}{\rm C} N_{\rm C} \sum_{j=1}^{3} \frac{\rm d}{{\rm d}T} \left(\frac{h_{\rm p}\nu_j}{\exp(h_{\rm p}\nu_j/k_{\rm B}T) - 1} \right), \tag{5.40}$$

where

$$f_n'(x) \equiv \frac{\rm d}{{\rm d}x} f_n(x). \tag{5.41}$$

5.4.2 Dust cooling

Dust grains are cooling by thermal emission. When a sphere dust grain of radius a, absorption coefficient $Q_{\rm abs}(\lambda)$ and temperature T, the power emitted by one grain is

$$4\pi\epsilon(T,a) = 4\pi \int \epsilon_\lambda(T,a){\rm d}\lambda = 4\pi \cdot \pi a^2 \int Q_{\rm abs}(\lambda) \frac{2h_{\rm p}c^2}{\lambda^5} \frac{{\rm d}\lambda}{\exp\left(\frac{h_{\rm p}c}{\lambda k_{\rm B}T}\right) - 1}, \tag{5.42}$$

and the cooling time $t_{\rm cool}$ is

$$t_{\rm cool}(T,a) = \frac{E(T,a)}{4\pi\epsilon(T,a)} \tag{5.43}$$

$E(T,a)$ is the internal energy of a dust grain. If energy is not input to dust grain, Equation (5.42) is equivalent with the time variance of dust grain internal energy represented as

$$C(T,a)\frac{{\rm d}T}{{\rm d}t} = -4\pi\epsilon(T,a). \tag{5.44}$$

This formulation is not solved analytically, but we can get the temperature variation by numerical calculation. For assuming sphere dust grain, the absorption coefficient $Q_{\rm abs}$ can be calculated exactly. We adopt Laor & Draine (1993) to graphite and silicate and Li & Draine (2001) to PAH absorption coefficient. We do not consider other effects of losing energy (e.g. sublimation from dust surface) in our model.

5.4.3 Calculation of dust temperature distribution by Monte Carlo simulation

We use Monte-Carlo (MC) simulation for calculating stochastic temperature distribution. MC is the numerical calculation method or simulation that depends on a random sampling number. In this subsection, we explain how to calculate the temperature distribution.

Firstly, we calculate the photon absorbed probability $\mathrm{d}p(a,\lambda)$ by a dust grain by Equation (5.29). We adopt a weighted absorption coefficient by the result of our dust evolution model (§4.7). and the mean energy density from PEGASÉ result. The probability depends on dust radius a and wavelength λ. But we fix a each MC because we want to calculate temperature distribution per a. Time interval $\mathrm{d}t(a)$ is defined as the most heigh probability becomes 10^{-3} each dust radius a.

Secondly, we generate N_λth (the number of discrete wavelength) random number $x_{\rm i}$ and differ with each $\mathrm{d}p(\lambda_{\rm i})$. When $\mathrm{d}p(\lambda_{\rm i}) > x_{\rm i}$, add photon energy $h_{\rm p}c/\lambda_{\rm i}$ to internal energy $E(a)$. And then, the temperature after heating is calculated by equation (5.31), (5.32), and (5.36). Actually, we do not calculate temperature each repeated, but also we use the table of internal energy-discrete temperature for fast calculation.

Third, we calculate dust cooling during interval time $\mathrm{d}t$ by Equation (5.44).

And, we repeat step two and three when more than 10,000 photons absorbed by a dust grain.

5.4.4 Dust temperature distribution

The temperature distribution of various grain sizes of silicate grains is shown in Figure 5.7. These are calculated by the Monte Carlo simulation which is introduced in §5.4.3, the PÉGASE.2 result of the Milky Way galaxy is used as a dust grains heating source. From Figure 5.7, the temperature of small grains spread very broad range, from under 1 K to 4,000 K. When grain size becomes bigger, the temperature range becomes narrow and approach to the equilibrium temperature. The equilibrium temperature is represented by Draine & Lee (1984); Takeuchi et al. (2003) as

$$T_{\rm eq} \simeq \left(\frac{h_{\rm p}c}{\pi k_{\rm B}}\right)\left[\frac{945u}{960\pi(2\pi Aa)h_{\rm p}c}\right]^{1/6}, \tag{5.45}$$

and

$$u \equiv \int_0^\infty u_\lambda \mathrm{d}\lambda, \tag{5.46}$$

where we adopt $A_{\rm sil} = 1.34 \times 10^{-3}\,{\rm cm}$ for silicate grains (Drapatz & Michel, 1977) and $A_{\rm C} = 3.20\times^{-3}\,{\rm cm}$ for carbonaceous grains (Draine & Lee, 1984). When grain size is 3.98×10^{-5} cm, the equilibrium temperature of that grain is about 19 K by Equation (5.45) and it is equal to calculated by MC simulation. For decreasing calculating time, I use Equation (5.45) for calculating temperature in 3.98×10^{-5} cm or more larger radius dust grains.

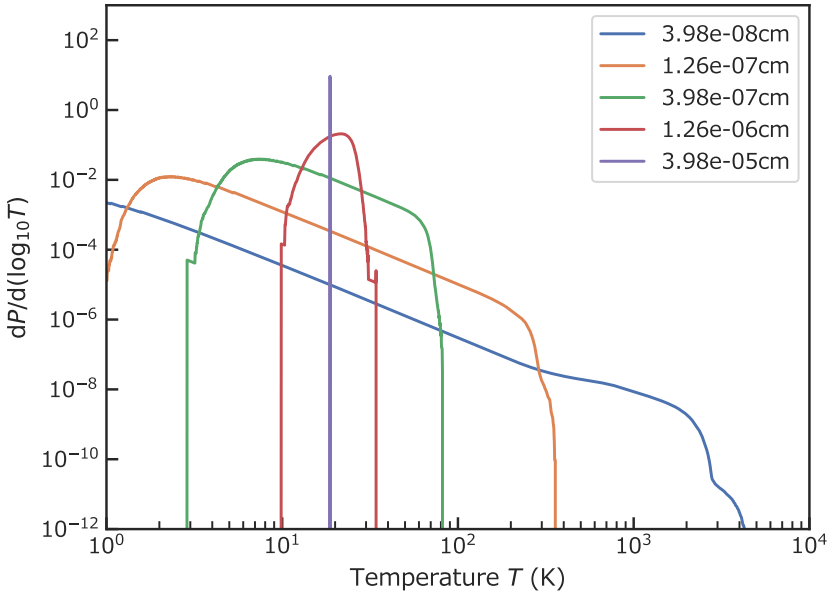

Figure 5.7: Temperature distribution of the several grain size of the silicate grains calculated by Monte Carlo simulation discussed in §5.4.3. The blue, orange, green, red and purple curves represent $3.98 \times 10^{-8}, 1.26 \times 10^{-7}, 3.98 \times 10^{-7}, 1.26 \times 10^{-6}, 3.98 \times 10^{-5}$ cm grains, respectively. the mean energy density per wavelength in galaxy is calculated by PÉGASE.2 in Milky Way like star formation scenarios with the age of 13 Gyr.

I show you temperature distribution of graphite in Figure 5.8, graphite grains have broad temperature compered with silicate grains in Figure 5.7, the difference comes from differences of internal energy between graphite and silicate (see: Figure 5.6).

Figure 5.9 is the temperature distribution of ionized and neutral PAHs. Comparing ionized PAHs temperature distribution with graphite's, PAHs stay a narrow temperature range because PAHs have an additional term in the equation of internal energy (5.36). In PAHs, there is almost no difference.

5.4.5 Dust radiation by temperature distribution

In this section, we calculate the dust emission spectrum, for very small dust grains using the dust temperature distribution computed by Monte Carlo simulation (§5.4.3). On the other hand, large grains have equilibrium temperature $T_{\rm eq}$ and it

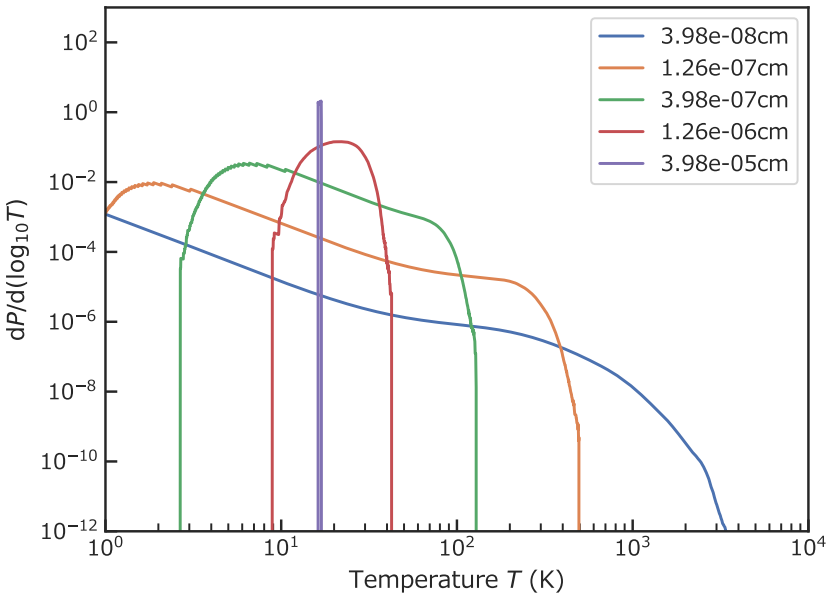

Figure 5.8: Temperature distribution of the several grain size of the graphite grains.

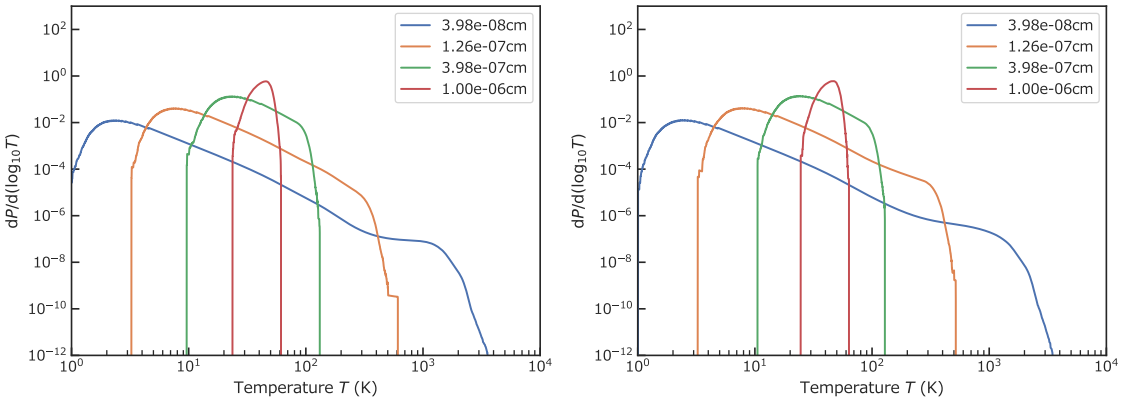

Figure 5.9: Temperature distribution of the several grain size of the neutral PAH grains. The Left panel is ionized PAH and the right panel is neutral PAH.

is calculated by equilibrium hearting and cooling in Draine & Lee (1984); Takeuchi et al. (2003),

The monochromatic luminosity of a dust grain with radius a is represented as

$$L_i^{\rm grain}(a,\lambda) = 4\pi a^2 \pi \int Q^i_{\rm abs}(\lambda) B_\lambda(T) \frac{{\rm d}P_i(a)}{{\rm d}T} {\rm d}T. \tag{5.47}$$

Where i represents dust species (we consider silicate, graphite, ionized PAH and neutral PAH) and ${\rm d}P_i(a)/{\rm d}T$ is the temperature probability density function from MC or Equation (5.45). If the dust is at equilibrium temperature T, the monochromatic luminosity by a dust grain at grain radius a is simply expressed as

$$L_i^{\rm grain}(a,\lambda,T) = 4\pi a^2 \pi Q^i_{\rm abs}(\lambda) B_\lambda(T). \tag{5.48}$$

Total luminosity at wavelength λ is given by

$$\begin{aligned} L(\lambda) &= \sum_i \int L_i^{\rm grain}(a,\lambda) \frac{{\rm d}n_i(a)}{{\rm d}a} {\rm d}a {\rm d}T & (5.49) \\ &= 4\pi^2 \sum_i \int {\rm d}a\, a^2 \frac{{\rm d}n_i(a)}{{\rm d}a} \int {\rm d}T\, Q^i_{\rm abs}(\lambda) B_\lambda(T) \frac{{\rm d}P_i(a)}{{\rm d}T}. & (5.50) \end{aligned}$$

${\rm d}n_i(a)/{\rm d}a$ is grain number density function from the dust evolution model (see §4).

Figure 5.10 is the result of luminosity for dust grains of different radius and various species (graphite: top left, silicate: top right, neutral PAH: bottom left, and ionized PAH: bottom right) heated by the interstellar galactic energy density of MW-like galaxy at an age of 13 Gyr with closed-box model. This figure plot only typical size of grain. The colors represent 3.98 (blue), 7.94 (orange) $\times 10^{-4}$, 1.26 (green), 3.98 (red), 7.94 (purple) $\times 10^{-3}$, 1.00 (brawn), and 1.26 (pink) $\times 10^{-2}$ μm, respectively. The temperature probability distribution of these grains are same as Figure 5.8, 5.7, and 5.9. These luminosities are weighted by dust size distribution calculated in same condition as the Figure 4.3. Large dust grain (> 0.01 μm) is responsible for radiation in the wavelength range greater than 10 μm. Large dust grain is at equilibrium temperature, and luminosity is expressed by Equation 5.48. Since the wavelength peak depends on the equilibrium temperature and the temperature depends on the radius of the dust, the larger the dust, the longer the wavelength peaks. The absorption coefficient $Q_{\rm abs}$ depends only on the wavelength, not on the radius and temperature of the dust, and is approximated in the form of $Q_{\rm abs} \propto \lambda^{-\beta}$. The radiation in the form of Equation 5.48 is called the modified black body (MBB) and grey body, and the observed dust radiation can be similar. We assume that the radiation is represented by a single size, composition, and temperature for fitting the radiation. Fits may be made assuming that the radiation is represented by a single size, composition, and temperature, and $1 < \beta < 2$ is suggested as the beta of MBB (e.g., Boselli et al., 2012; Auld et al., 2013). Graphite is the dominant component of dust emitting light in large wavelength region (> 10 μm), and silicate is dominant only in the larger wavelength range.

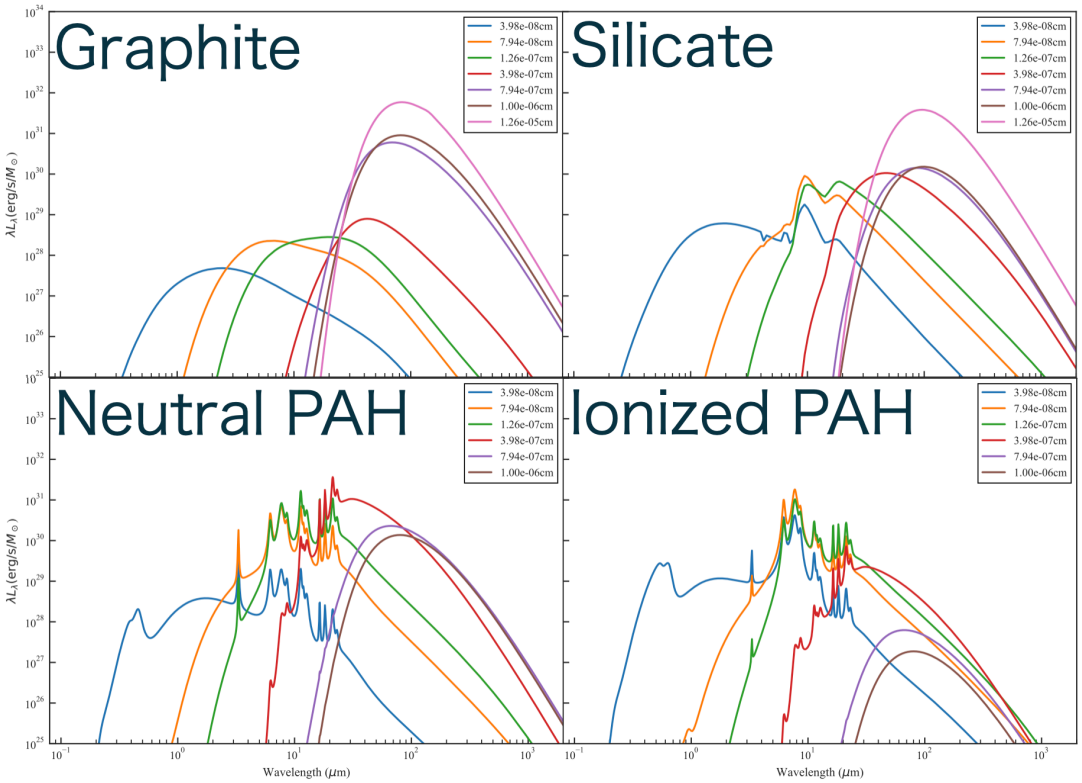

Figure 5.10: The infrared SED emitted by dust grains heated by energy density of MW-like galaxy at 13 Gyr. Top left panel shows graphite, top right panel shows silicate, bottom left panel shows neutral PAH, and bottom right panel shows ionized PAH. Color coordination represent various radius and written on each plots.

In the short wavelength range (< 10 μm), small dust emission is dominant, and the dust temperature has not reached the equilibrium temperature and is stochastic temperature, so the radiation seems to be wider than the blackbody radiation. Most of the radiation for each size is emitted by the high temperature part at the right end of the temperature probability distribution, and the peak shifts to the long wavelength side as the size increases. PAHs have characteristic features in this wavelength range, which are generated by the stretching or bending modes. The feature is found in a fixed wavelength, and independent of the grain radius. In this region, the graphite and silicate radiation is swamped in the PAH radiation. Neutrals dominate this MIR region, but ionized PAHs dominate in some of the short wavelength regions.

5.5 Summary of our SED model

Before showing the results, we give a summary of our model.

Wavelength 10 Å–99.2 cm divided into 2700 logarithmic bins. The range below 912 Å is considered to be zero radiation due to Lyman break. Our model do not include radio light emitted by synchrotron radiation and free-free emission.

Stellar emission Calculated by PÉGASE.2 (Varosi & Dwek, 1999). The stellar population is calculated by Padova groups SSP with Salpeter's IMF (Equation (2.5); Salpeter, 1955) and Schmidt's SFR (Equation (5.3); Schmidt, 1959). Our model do not include nebular line emissions. See §5.1.

Dust radius 3.16 Å–7.94 μm divided into 45 logarithmic bins.

Dust species 9 species [C, Si, SiO_2, Fe, FeS, Al_2O_3, MgO, $MgSiO_3$, and Mg_2SiO_4] for stellar production and accretion, 4 species [Graphite, neutral PAH, ionized PAH, and Silicate] for other processes.

Dust properties Draine & Lee (1984) and Laor & Draine (1993) for graphite and silicate, and Li & Draine (2001) for PAH. Dust mass and size distributions are calculated by the dust evolution model (see §4).

Geometry One-dimensional plane parallel galaxy (Varosi & Dwek, 1999; Inoue, 2005). See §5.3.

Attenuation Radiative transfer in the geometry with mega-grain approximation.

Dust emission Calculate by stochastic heating with Monte Carlo simulation. It consider the balance between energy of absorption and emission by dust grains (see §5.4).

Free parameters 3 or 4 with SFH (closed-box case: $t_{\rm gal}$, $tau_{\rm SF}$, $M_{\rm gal}$, infall model case: addition of $\tau_{\rm infall}$), and 2 with geometry ($R_{\rm gal}$, $h_{\rm d}$). Basically they are 5 or 6 in total. We can also consider two additional degrees of freedom for the

ISM phase in dust evolution model ($\eta_{\rm WNM}$, $\eta_{\rm CNM}$, $\eta_{\rm MC}$, with $\eta_{\rm WNM} + \eta_{\rm CNM} + \eta_{\rm MC} = 1$).

Thanks to the consideration of dust evolution, there are no parameters related to attenuation, and there are few free parameters, which is a feature of our model. These are a summary of the parameters used in this thesis, and the user can change the SFH at will.

Chapter 6

Result

Our model can generate various galaxy SED by the methods which are discussed above chapters. In this chapter, we present some output of our model.

6.1 SED of a Milky Way like galaxy

Our SED model returns a set of separate SEDs of several components (star, silicate, graphite, ionized PAH, and neutral PAH). The SED of each components of the MW-like galaxy at the age of galaxy $t_{\rm gal} = 13$ Gyr is presented in Figure 6.1 with parameters listed in Table 6.1 (we call it "MW-like galaxy model"). The SED is calculated based on the closed-box model. The perpendicular axis represents the emitted energy per unit time per solar mass. The black curve expresses the overall emission (i.e., the sum of attenuated stellar SED and the SED from each dust grain species). At wavelength of 912 Å, there is a cut-off of emission due to the Lyman break. Green, red, blue, and orange lines represent the luminosity emitted by silicate, graphite, ionized PAH, and neutral PAH, respectively. The SED in UV to NIR wavelength region is dominated by the attenuated stellar emission. The PAH features stand out in the MIR range. The emission of graphite grain dominates the longer IR wavelengths, while silicate emission dominates only submillimeter wavelength regime.

For a comparison, an SED obtained from PÉGASE.3 (Fioc & Rocca-Volmerange, 2019) is plotted in Figure 6.2. Their SED is also referred to as the "MW-like galaxy model" at the age of 13 Gyr with open-model (infall model). We observe a difference between their SED and ours. They adopt an infall timescale $\tau_{\rm infall} = 6$ Gyr, SF time scale $\tau_{\rm SF} = 6$ Gyr, and the IMF is from Kroupa et al. (1993). Their overall emission (Figure 6.2) is almost the same with our result (Figure 6.1), but our graphite emission is weaker than that from PÉGASE. There can be several reasons for this difference. First, the dust size distribution and the relative masses

Table 6.1: MW model properties

$M_{\rm gal}$ $[M_\odot]$	$\tau_{\rm SF}$ [Gyr]	$R_{\rm gal}$ [kpc]	$h_{\rm s}$ [pc]	$\eta_{\rm WNM}$	$\eta_{\rm CNM}$	$\eta_{\rm MC}$
10^{11}	3.0	10	150	0.5	0.3	0.2

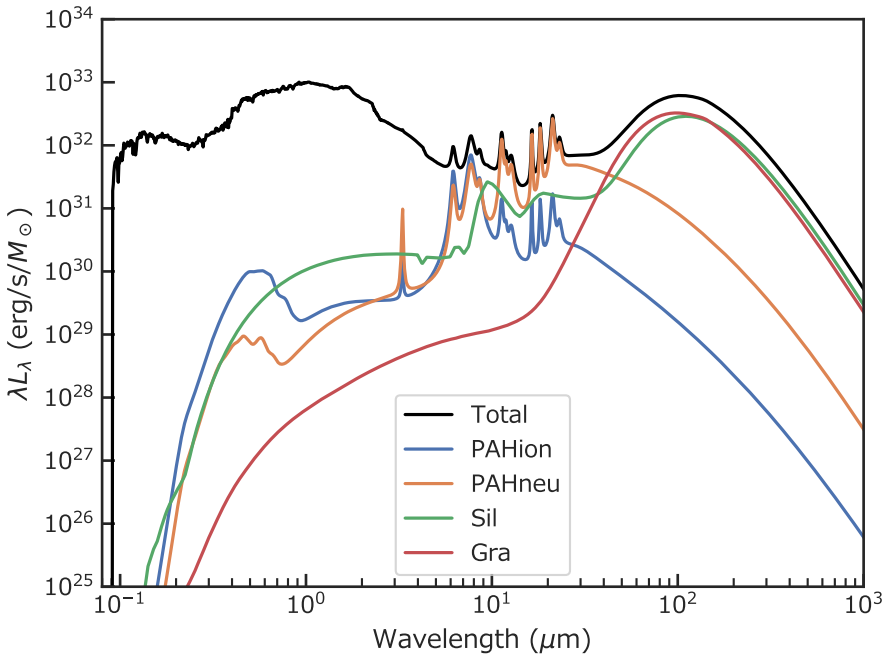

Figure 6.1: The SED of Milky Way like galaxy model at galaxy age 13 Gyr. The inclination angle is 0 degree ($\mu = 1/\cos\theta = 1$; face-on). The black, blue, orange, green and red lines represent total (stellar SED + dust grains SEDs), ionized PAH, neutral PAH, silicate and graphite SED, respectively.

of three carbonaceous grains in PÉGASE.3 are assumed to be constant, and the overall mass in the ISM only evolves with the age of a model galaxy. In contrast, the grain size distribution of our model evolves with the galaxy age.

Second reason may be the assumed SFH in our model is different from Fioc & Rocca-Volmerange (2019). We assumed the closed-box model, but Fioc & Rocca-Volmerange (2019) used infall model (see §6.1.1 about the precise difference between closed-box and infall model). Adopting infall model makes the evolution of dust mass slower and increases dust mass and IR emission at the end. Further, the adopted IMF between our model and PÉGASE is different. We adopted the Salpeter IMF (Salpeter, 1955) while PÉGASE adopted the Kroupa IMF (Kroupa, 2001). Since the ratio between massive and less-massive stars is different between the two models, it would be the main cause of the discrepancy.

6.1.1 Comparison between closed-box and infall model

The comparison between closed-box and infall model is showed in Figure 6.3. For the infall model, the initial mass in a galaxy is set to be zero, and primordial gas fall in galaxy at exponentially decreasing rate, with a timescale 6 Gyr (This is the same value as Fioc & Rocca-Volmerange (2019)). The time evolution of SFR and dust mass is plotted in Figure 6.4. The SFH is very different between the two scenarios.

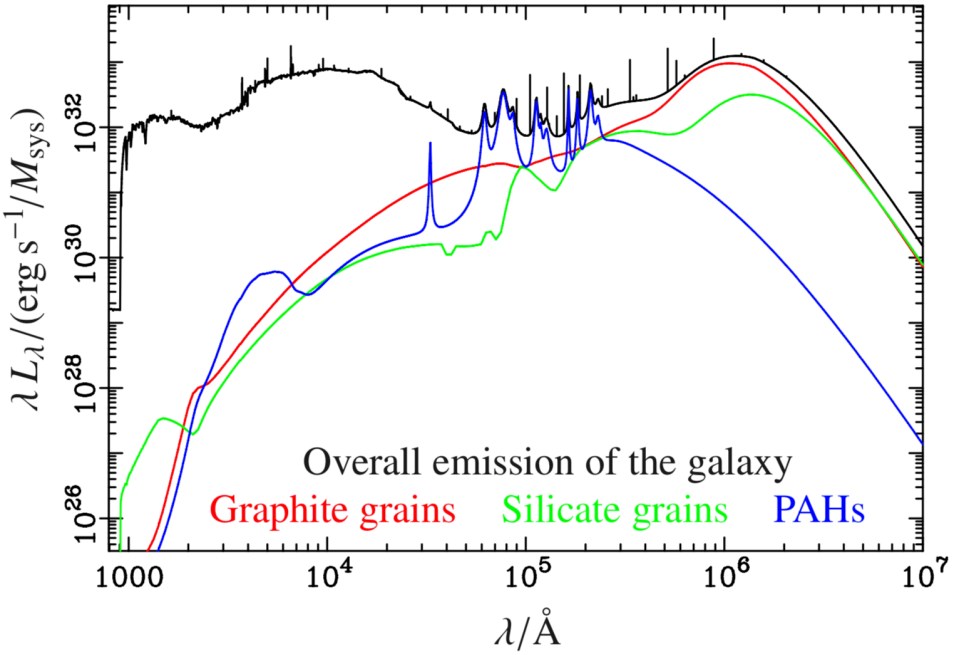

Figure 6.2: The SED sample of MW like a galaxy with the age of 13 Gyr calculated by PÉGASE.3. The perpendicular axis expresses the emitted energy per unit sec per solar mass. The color of curves represents according to species emission (black: overall emission, red: graphite grains, green: silicate, and blue: PAHs). Credit: Fioc & Rocca-Volmerange (2019)

Whereas the SFR of the closed-box model monotonically decreases, the SFR of the infall model first gradually increases and it reaches a peak at $t_{\mathrm{gal}} = 5$ Gyr (close to infall timescale $t_{\mathrm{infall}} = 6$ Gyr), and decreases. Since the SFR at 13 Gyr of the infall model is higher than that of closed-box model, the ratio of younger stars is increased in infall model, and then the luminosity of UV region becomes stronger than the closed-box result. In contrast, the near-UV region emitted by old stars is weakened due to a smaller mass of old stars at the same age. In the infall model, the dust mass peaks later than the closed-box, because of the difference in the SFH. It leads to the increase of the IR luminosity from dust grains, and the resulting SED would become more similar to the SED of PÉGASE (Figure 6.2). In general, the infall model tends to slow down the evolution of galaxy.

6.2 Time evolution of galaxy SED

Our model can calculate a galaxy SED at any age of a galaxy. Figure 6.5 represents the time evolution of SED calculated with the properties of the closed-box MW-like model listed in Table 6.1. The purple curve represents the same SED as Figure 6.1. Other color curves (blue, orange, green, and red) represent the MW-like model's SED at age 100 Myr, 1, 5, and 10 Gyr, respectively. The figure shows that UV luminosity monotonically decreases with the evolution of a galaxy. The reason for

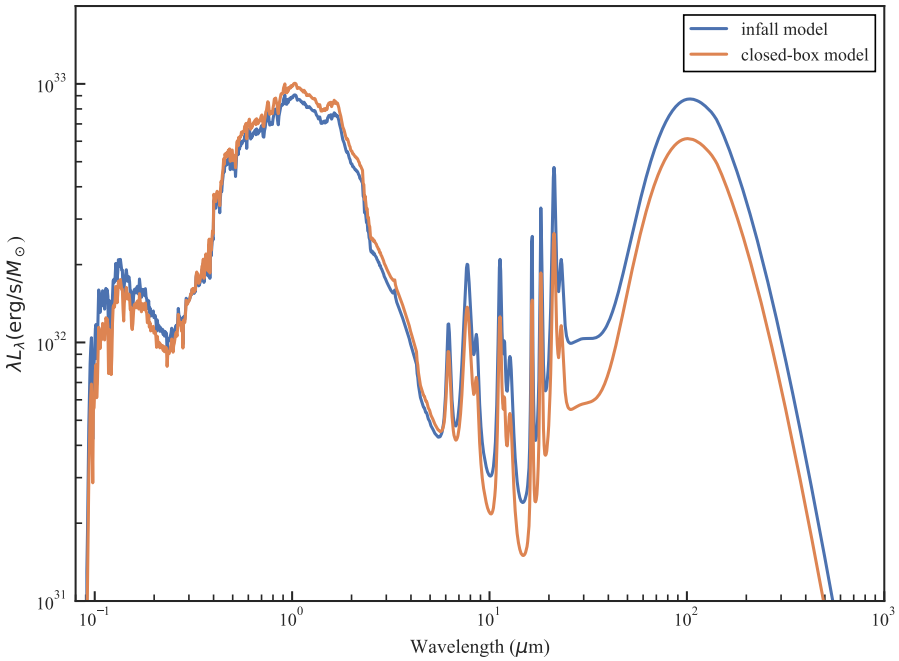

Figure 6.3: The comparison of MW-like model galaxy SED at age $t_{\rm gal} = 13$ Gyr with infall and closed-box model. The orange line represents closed-box model (same as Figure 6.1), the blue line represents infall model with infall time scale $\tau_{\rm infall} = 6$ Gyr.

this is as follows: We assume that the galaxy initially has primordial gas (zero-metallicity), the galaxy is a closed box model, and the SFR is proportional to the total gas mass with timescale $\tau_{SF} = 3$ Gyr. Therefore, the galaxy has a peak of the SFR at the beginning of galaxy evolution. Gas is only consumed by star forming and dust construction, and so the SFR only decrease (see red solid line in Figure 6.4). This is lead to the monotonically decreasing the UV emission.

At 100 Myr, the stellar radiation is not attenuated and the dust radiation is very weak, because only a little amount dust has been generated. Particularly, PAHs are not produced in such an early stage of a galaxy, and MIR radiation would be too weak to be detected. In such a young galaxy, SNe II are the unique source of dust grain production, since their lifetime is short (10^6–10^7 yr) (Maiolino et al., 2004; Hiraki & Hirak, 2008). The galaxy age is not yet long enough for star to grow to AGB phase (life time is 10^8–10^9 yr) (Morgan & Edmunds, 2003; Marchenko, 2006), though there are some suggestions that AGB stars dominate the dust supply in relatively young galaxies (> 100 Myr) with very high star formation rates (e.g., Valiante et al., 2009). Very small dust such as PAHs are supplied in small quantities from stars (e.g., Nozawa et al., 2007). In addition, to explain the observed amount of dust in nearby galaxies, significant fraction of metals must be turned to form dust grains and further the grains have to get more mass via dust growth (Inoue, 2011; Asano et al., 2013a). These facts are consistent with the result of our model. If a dust model estimated from observations of nearby galaxies is used without taking into account the evolution of dust size distribution,

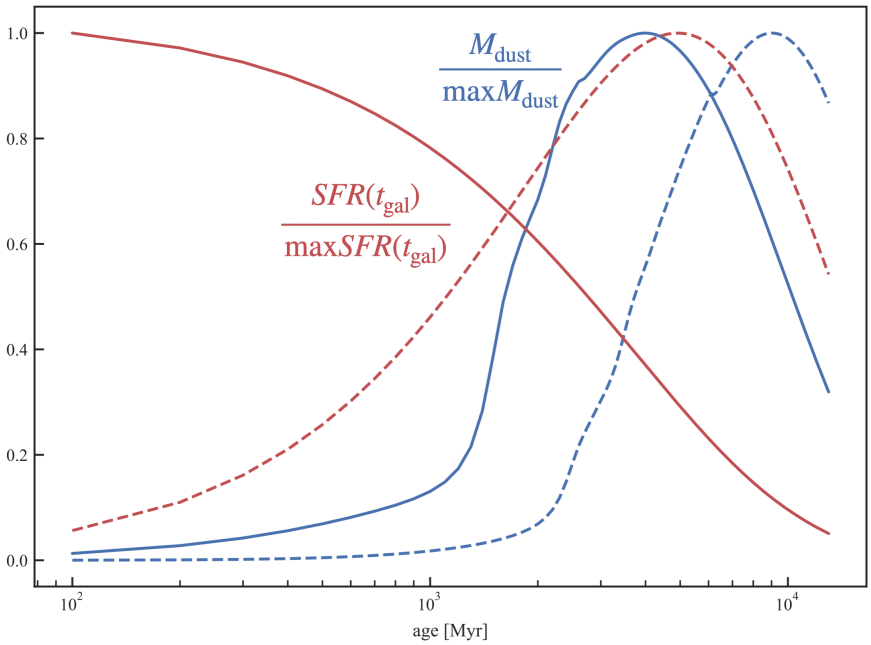

Figure 6.4: The time evolution of dust mass and SFR in closed-box and infall model galaxy (same galaxies as Figure 6.3). Colors represent the difference of quantities: the ratio of $SFR(t_{\rm gal})$ and maximum value of it (red), and the ratio of dust mass $M_{\rm dust}$ and maximum value of it (blue). The solid and dashed lines represent closed-box and infall model, respectively.

we would overestimate the dust mass in such distant galaxies from the theoretical side. This is the most striking prediction of our SED model.

We plot the evolution of metallicity and dust mass with MW-like galaxy model in Figure 6.6. The metallicity and dust mass are normalized by solar metallicity $Z_\odot$ and maximum dust mass $\max(M_{\rm dust})$, respectively. Here we adopt $Z_\odot = 0.2$ (Anders & Grevesse, 1989). It is suggested that in a MW-like galaxy, when the metallicity exceeds 0.1 $Z_\odot$ (Asano et al., 2013a), the accretion process becomes effective. After that, the grain-grain collisions also become effective and the mass of dust begins to increase, since the total surface area of grains becomes larger because of shattering. At MIR, in Figure 6.5, we see characteristic PAH band features gradually appearing after ~ 1 Gyr, as dust growth becomes more effective. Contrary to the UV light, the IR light emitted by dust grain continues to increases until 3 Gyr. The dust emission peaks at 3 Gyr in Figure 6.5, but this age depends on star formation timescale $\tau_{\rm SF} = 3$ Gyr.

After 3 Gyr, dust becomes weaker, because of two reasons. First, dust mass gradually decreases, because of the decline of the formation of young stars, which produce dust. Second, the stellar radiation is the heating source of dust grains, and thus dust radiations also become weaker with diminishing stellar radiation.

Another feature of the evolution of the galaxy is the shift of an IR peak, the peak shift from 60 μm at an age of 100 Myr to more than 100 μm at 13 Gyr. This shift is caused by the decrease of the formation rate of young stars. Young star is surrounded by molecular cloud containing high density dust grains. Young star

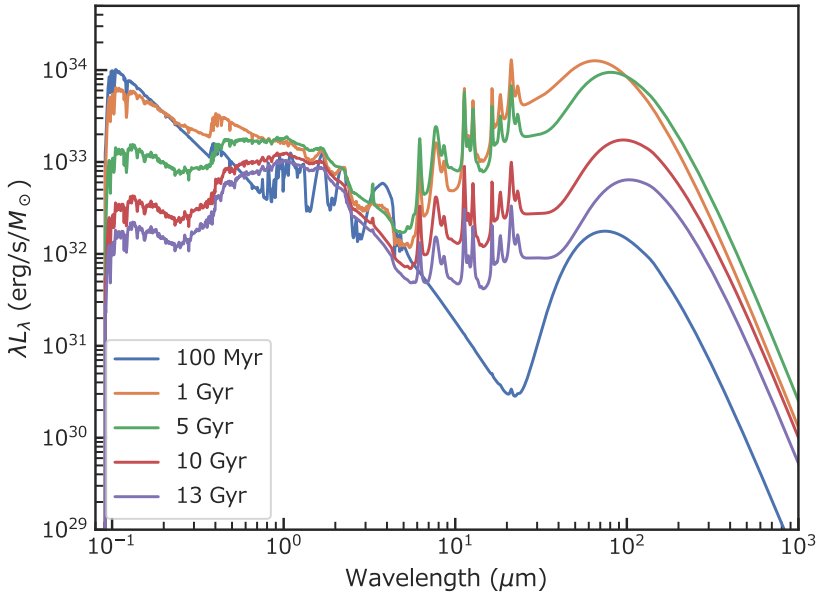

Figure 6.5: The time evolution of overall SED. The MW model parameter is same as Figure 6.1. The blue, orange, green, red and purple curve represents the galaxy age of 100 Myr, 1 Gyr, 10 Gyr, and 13 Gyr, respectively.

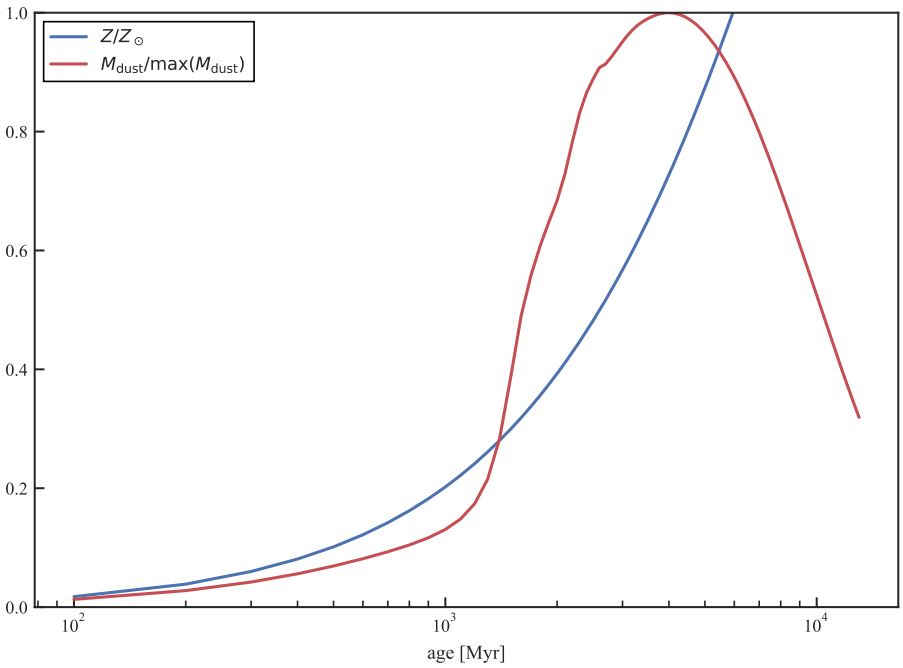

Figure 6.6: The time evolution of normalized metallicity (blue curve) and dust mass (red curve). The MW model parameter is same as Figure 6.1.

emits high energy photon, the star is main source of heating dust grain to high temperature. In late age of galaxy, diffuse old stellar fraction increase and the average temperature of dust grain becomes low temperature.

The time evolution of bolometric luminosities each component of galaxy are plotted in Figure 6.7. This figure presents the ratios between luminosities at different wavelengths as a function of the galaxy age: ratios of the emitted by star $L_{\rm star}$, dust $L_{\rm dust}$, silicate $L_{\rm silicate}$, graphite $L_{\rm graphite}$, ionized PAH $L_{\rm PAHion}$, and $L_{\rm PAHneu}$, to the overall bolometric luminosity $L_{\rm total}$.

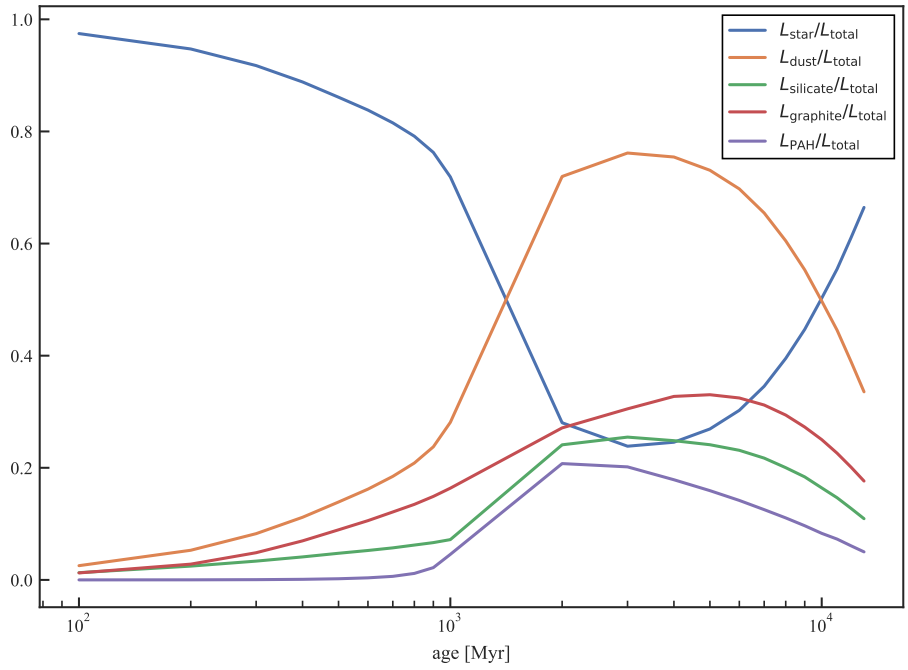

Figure 6.7: The time evolution of each component of the SED of MW-like galaxy. The blue, orange, green, red and purple curve represent ratio of the bolometric luminosity emitted by star $L_{\rm star}$, total dust $L_{\rm dust}$, silicate $L_{\rm silicate}$, graphite $L_{\rm graphite}$, and PAH $L_{\rm PAH}$, to the overall bolometric luminosity $L_{\rm total}$, respectively.

The UV light dominates the overall bolometric luminosity until 1 Gyr. After an age of 1 Gyr, the SED becomes redder due to the dust attenuation, that transports energy from stellar emission (UV) to the dust emission (IR). In parallel, the dust emission rapidly increase due to excess the critical metallicity in the ISM. In more than 10 Gyr old epoch, the dust emission gradually decrease as dust destruction by SN shock and suppression of production by stellar winds, the stellar emission will excess the dust emission.

Note the difference in evolution of each species of dust grain in Figure 6.7. The increase of graphite emission is more continuously than the increase of other dust components. The discontinuities of increasing of dust mass and emission are caused by the existence of the critical metallicity in metal accretion on dust surface (Asano et al., 2013a). Because of the increasing efficiency of accretion, shattering effect which increase small size of dust, also becomes easy to occur, and so dust emission rapidly increase. We, however, should note that we regard

almost all small carbonaceous dust grains as PAHs, hence the graphite grain mass do not show the discontinuous increase. The bolometric luminosity of dust grain is dominated by graphite in all epochs.

Chapter 7

Discussions

7.1 Dependence of the result on the model components

Our model contain some free parameters. The common five parameters are as follows:

1. three for SFH
   (a) galaxy age $t_{\rm gal}$,
   (b) star formation timescale $\tau_{\rm SF}$,
   (c) initial galaxy mass $M_{\rm gal,0}$,
2. two for geometry of galaxy
   (a) radius of galaxy $R_{\rm gal}$,
   (b) perpendicular scale height of dust $h_{\rm d}$.

In addition to these common parameters, we have some more parameters:

1. two parameters for infall model
   (a) total infall mass $M_{\rm infall}$
   (b) infall time scale $\tau_{\rm infall}$,
2. two degree of freedoms for ISM phase fraction
   (a) WNM $\eta_{\rm WNM}$,
   (b) CNM $\eta_{\rm CNM}$,
   (c) MC $\eta_{\rm MC}$).

In this section, we discuss about effect of variance of free parameters.

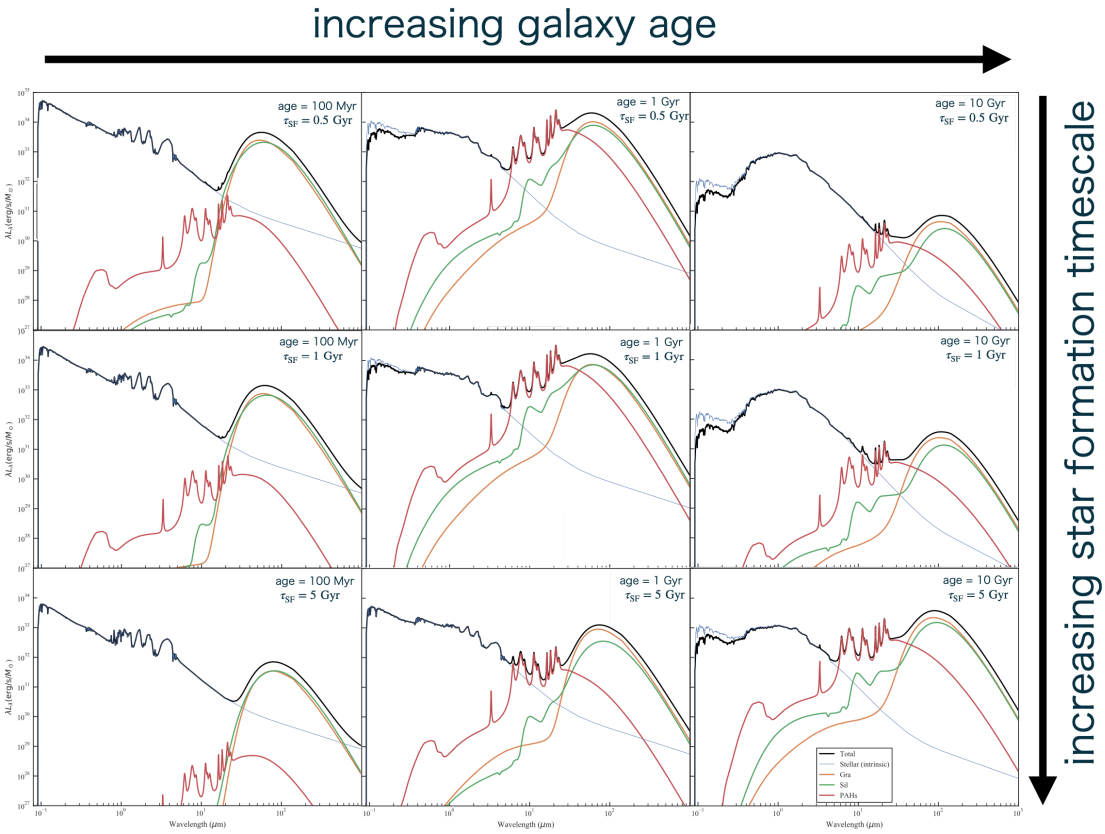

Figure 7.1: The effect of star formation timescale for our galaxy SED model. From left to right the panels show galaxies with various age (100 Myr, 1 Gyr, and 10 Gyr). From top to bottom the panels show galaxies with various star formation timescale ($\tau_{\rm SF}$ = 0.5, 1, and 5 Gyr). Color coding represents various component (black: total emission, blue: intrinsic stellar emission, orange: graphite, green: silicate, and red: PAHs).

7.1.1 Effect of star formation timescale

The effect of star formation timescale for our galaxy SED model is shown in Figure 7.1. Figure 7.1 is closed-box result and we only changed the SF timescale $\tau_{\rm SF}$ and age, and the geometrical parameters are the same as MW-like model (Table 6.1). The galaxy age increases from left to right the panels (100 Myr, 1, and 10 Gyr), and SF timescale increases from top to bottom the panels ($\tau_{\rm SF}$ = 0.5, 1, 5 Gyr). Three trends are clear from Figure 7.1.

First, at the age of 100 yr, both the UV luminosity from stars and the IR luminosity from graphite and silicate grains decrease with increasing SF timescale. In these young galaxies, PAHs are not yet produced and the PAHs emission do not appear. This indicates that the dust mass in early galaxy is dominated by production form stars instead of accretion, shattering, and coagulation processes.

Second, the overall bolometric luminosities tend to be stronger when the age of galaxy becomes equal to the SF timescale. In this epoch, the SFR is still large and significant amount of dust exist in the galaxy.

Third, when the age of a galaxy is larger than the SF timescale, the galaxy have very weak stellar emission due to consumption of most of the gas in the ISM. The dust emission also becomes very weak in the galaxy because both, decreasing dust mass and UV light which is the source of heating dust grains.

7.1.2 Effect of the geometry of the galaxy

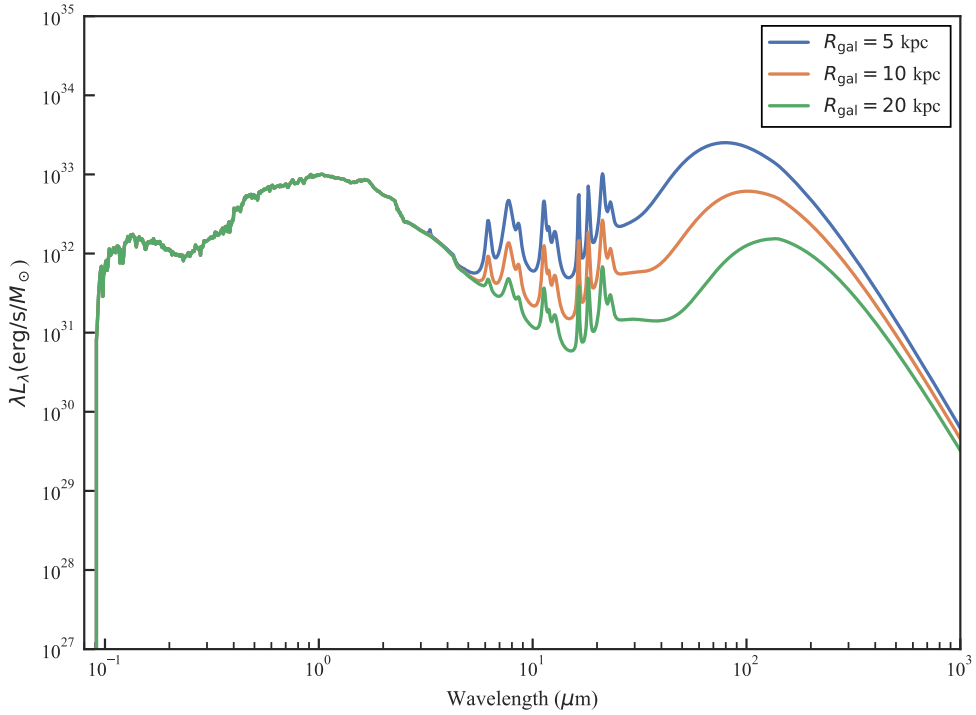

Figure 7.2: The galaxy SED with parameters listed in Table 6.1 and the various galaxy radius at an age of 13 Gyr. Blue, orange, and green curves represent the galaxy SED with radius 5, 10, and 20 kpc, respectively.

Figure 7.2 shows the effect of changing galaxy radius $R_{\rm gal}$ for our galaxy SED model at an age of 13 Gyr. Other parameters are same as Table 6.1. Blue, red, and green curves represent $R_{\rm gal}$ = 5, 10 (fiducial), and 20 kpc, respectively. The figure indicates that changing galaxy radius only affects the IR emission. Since our model assume the galaxy as one-dimensional plain parallel, the galaxy radius changes the energy density for the heating of dust grains. Consequently, dust emission increase with decreasing the galaxy radius. However, in reality, changes in galaxy radius vary the density of dust in the star-forming region and the ratio of WNM and CNM, so it is possible that the effective extinction coefficient $\kappa_{\rm eff}$ would change. Therefore, when considering a galaxy with a geometry that is significantly different from the MW ($R_{\rm gal}$ = 10 kpc, $h_{\rm d}$ = 150 pc), it may be necessary to tune the density of WNM ($n_{\rm H,WNM}$) and CNM ($n_{\rm H,CNM}$) in Equation (5.5), (5.4) and the radius of the clump ($r_{\rm cl}$) in Equation (5.6).

We plot the galaxy SED with the various dust scale height of galaxy at an age of 13 Gyr in Figure 7.3. The larger the scale height of dust in the galaxy is,

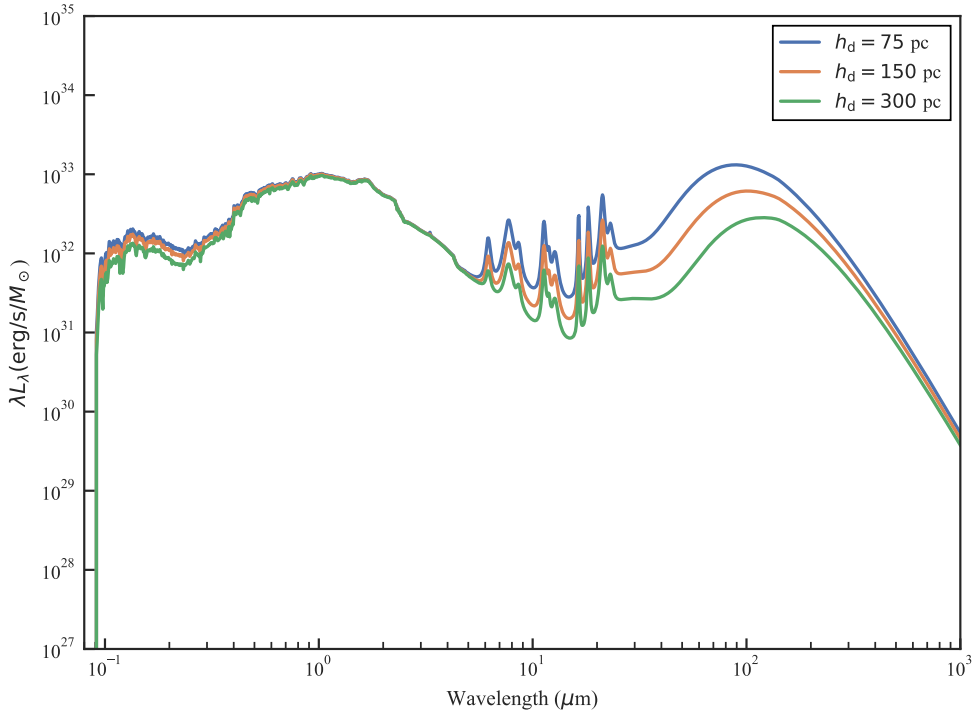

Figure 7.3: The effect of scale height of dust in the galaxy with the parameters listed in Table 6.1 at an age of 13 Gyr. Blue, orange, and green curves represent the galaxy SED with scale height $h_\mathrm{d} = 75$, 150, and 300 pc, respectively.

the weaker the radiation of both star and dust grain become. The intrinsic stellar radiation does not depend on the scale height. As the attenuated length increases, observed emission in UV region becomes weaker. For the IR emission, the energy density is affected by the volume of the galaxy, and a galaxy with a large scale height emits weaker IR radiation than those with smaller scale height.

To summarize the effects of geometry, the UV from the stellar population depends only the radius of the galaxy, and the IR region emitted by dust grain is inversely proportional to the volume of the galaxy.

7.1.3 Effect of ISM phase fraction

Effect of the ISM phase fraction to MW-like galaxy model at an age of 13 Gyr

We show the three extreme cases $(\eta_\mathrm{WNM}, \eta_\mathrm{CNM}, \eta_\mathrm{MC}) = (1.0, 0.0, 0.0)$, $(0.0, 1.0, 0.0)$, and $(0.0, 0.0, 1.0)$ in Figure 7.4. Other properties are fixed to the MW-like galaxy model (Table 6.1). First, we compare the case of CNM only and the case of MC only (middle and bottom panels in Figure 7.4). We assume all the dust-size related processes except destruction (accretion, shattering, and coagulation) occur in both phases. In the MIR wavelength, the CNM only case has a higher PAH luminosity than the MC only case, and the size distributions show the CNM only case have also larger amounts of small carbon grains than that of the MC only case. This

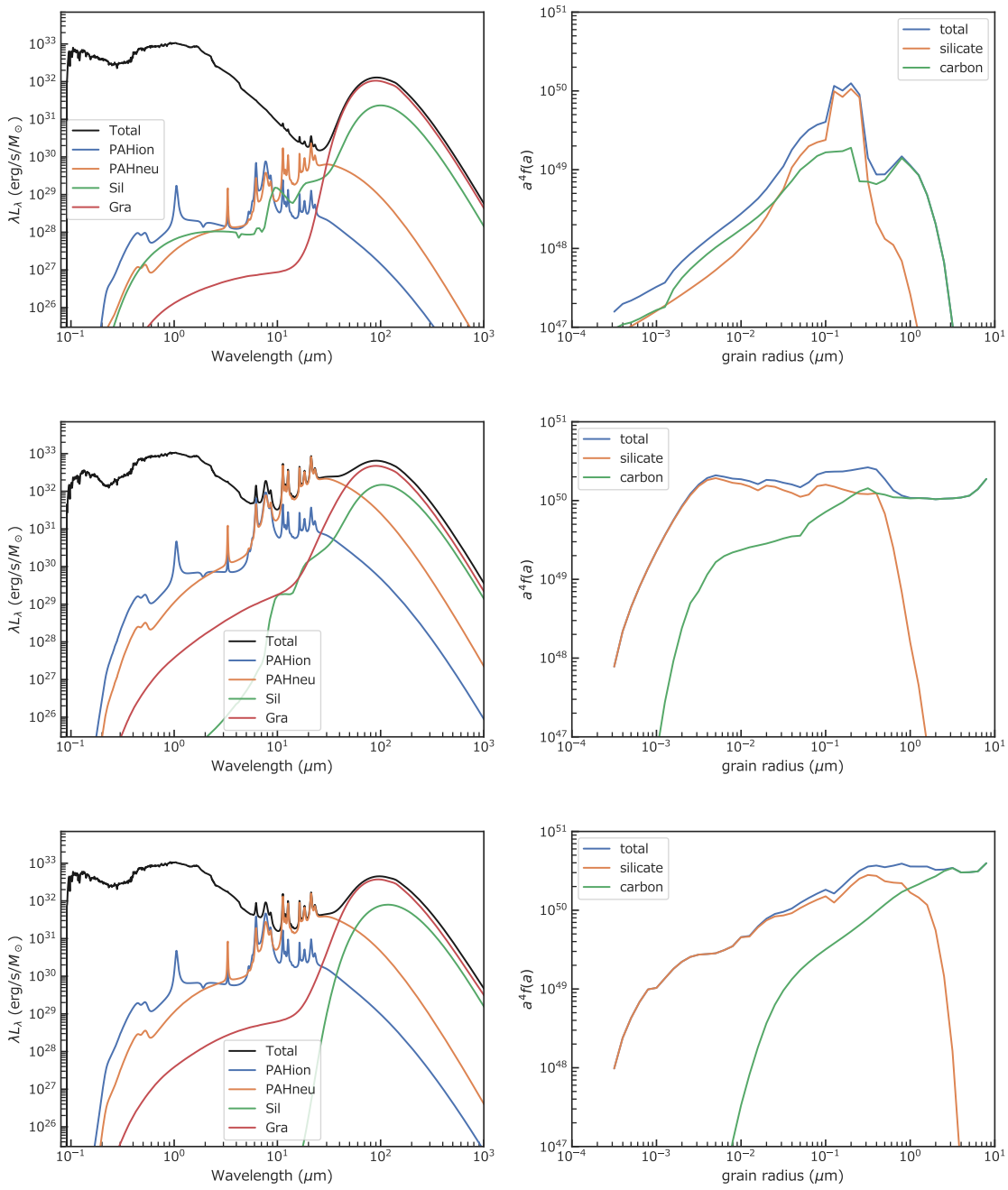

Figure 7.4: The result of galaxy SEDs (left side panels) and grain distributions (right side panels) with $(\eta_{\rm WNM}, \eta_{\rm CNM}, \eta_{\rm MC}) = (1.0, 0.0, 0.0)$ (upper panels), (0.0, 1.0, 0.0) (middle panels) and (0.0, 0.0, 0.1) (bottom panels).

difference comes from the shattering process, shattering easily to occur in the high-temperature phase because the grain velocity depends on the temperature, and the CNM temperature is higher than the MCs. The difference between large size grain distributions is thought to be the same reason.

The result of WNM only case is significantly different from the other cases. Very little small size grains are produced in the WNM only case because we assume grain growth does not occur in the WNM phase. This indicates that accretion process is very important for evolution the dust grains. Particularly, PAH features cannot appear in the WNM only case. If such an SED without PAH features (but otherwise normal) is observed, the ISM of the observed galaxy might have high temperature ISM.

Effect of ISM phase to time evolution of SED

We show the time evolution of the SEDs and dust size distributions with the ISM fraction $(\eta_{\rm WNM}, \eta_{\rm CNM}, \eta_{\rm MC}) = (1.0, 0.0, 0.0)$, $(0.0, 1.0, 0.0)$, and $(0.0, 0.0, 0.1)$ in Figure 7.5. Colors expressed according to the age of the galaxy. At the age of 100 Myr, all panels in Figure 7.5 seem almost all the same shapes. Because, in such early galaxy, dust grains are not produced yet, and the SEDs are dominated by stellar light and a few amounts of large grains.

In the upper panels (WNM only cases), dust radiations reach to peak at 5 Gyr, when the features of PAHs can seem in the MIR. But after that, the features are vanished, since destruction by SN shocks and decreasing the stellar light which is the source of grain heating. After that, the PAH features disappear due to the destruction by the SN shock and the decrease in the light of the star, which is the heating source of the grain. The small grains are difficult to be produced in any age of this galaxy because of nothing of the accretion process.

In bottom panels (MC only cases), from MIR to FIR wavelength region have a peek at the age of 1 Gyr. This is the same trend with the MW in Figure 6.5, and there are two reasons. First, it is owning to decreasing the grain heating source of stellar lights. Second, the rapid grain evolution by the coagulation, since the MC has very low temperature and high number density. On the contrary, in the CNM only cases (middle panels), it has the peak of the FIR wavelength at the age of 5 Gyr, it is because the dust size distribution at the age of 1 Gyr has the bump at $a \sim 0.001$ μm. This is thought to the shattering effect (Asano et al., 2013b).

7.2 Comparison with observed photometry and GRASIL fitting result

Present version of our code does not yet have the ability to fit to the observed data, so we need to manually fluctuate the parameters (e.g., the SF timescale, the radius of galaxy, the scale height of galaxy, the total mass of galaxy, and the age of galaxy) to get closer to the observed data. Of the three codes introduced in §3.5, GRASIL is the only one that has geometry as parameters. So here we compare the observed data with our model while referring to the GRASIL fit results. In

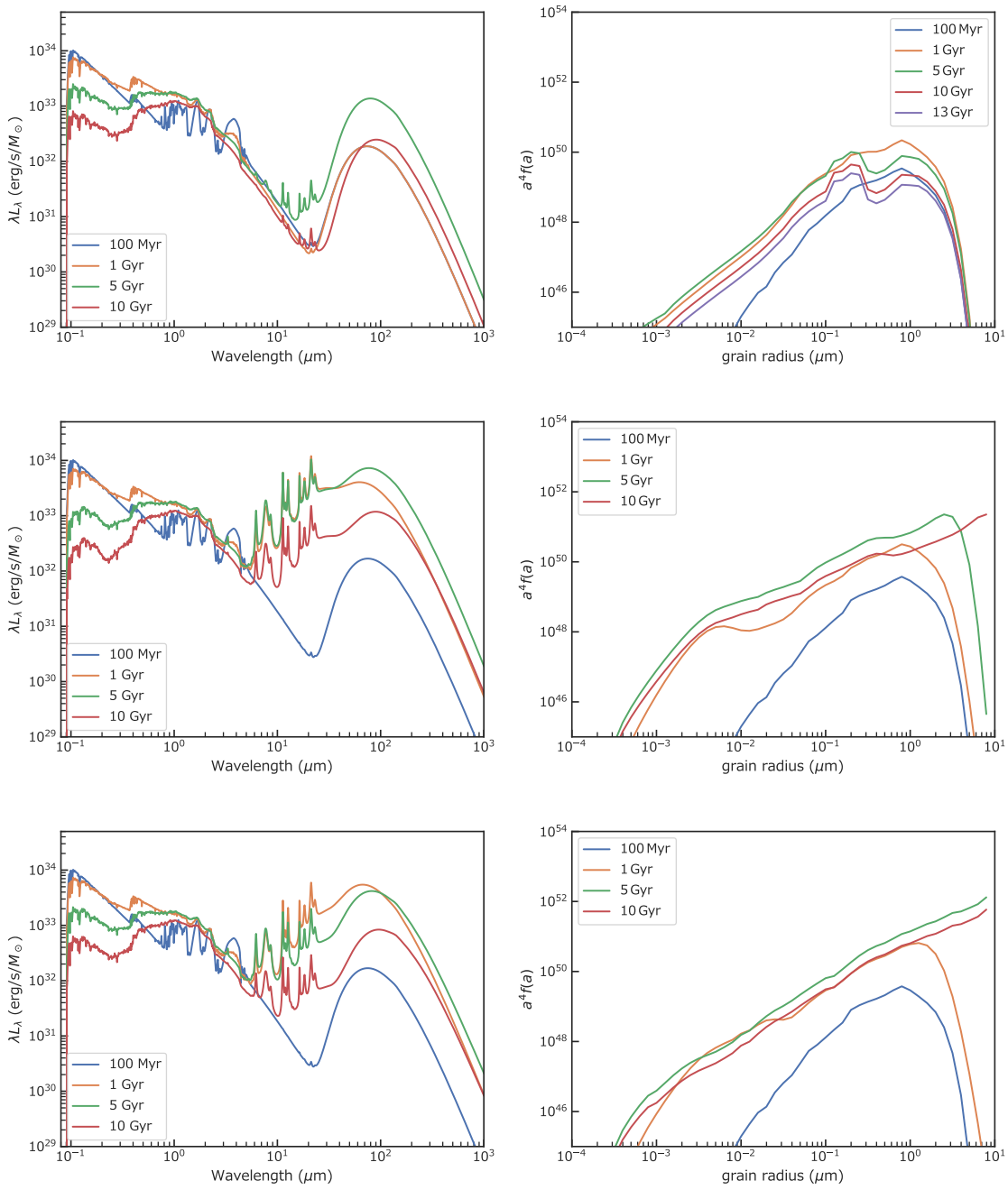

Figure 7.5: The time evolution of galaxy SEDs (left side panels) and grain size distributions (right side panels) with $(\eta_{\rm WNM}, \eta_{\rm CNM}, \eta_{\rm MC}) = (1.0, 0.0, 0.0)$ (upper panels), (0.0, 1.0, 0.0) (middle panels) and (0.0, 0.0, 1.0) (bottom panels).

this subsection, we compare our model with late-type spiral galaxy same as Silva et al. (1998). Silva et al. (1998) fits three spiral galaxies data which are observed by Infrared Astronomical Satellite (*IRAS*) and Infrared Space Observatory (*ISO*).

M51 (NGC 5194)

M51 (NGC 5194) is the nearly face-on ($i = 20°$; Tully, 1974) Sbc galaxy. The distance is $D = 9.6$ Mpc (Sandage & Tammann, 1975). Figure 7.6 shows the fitting result of *IRAS* observation data at galaxy age of 13 Gyr by GRASIL (Silva et al., 1998) and the modeling result of our model with parameters listed in Table 7.1.

Table 7.1: Modeling parameters of M51

Model	$M_{\rm gal}$ [$M_\odot$]	$\tau_{\rm SF}$ [Gyr]	$\tau_{\rm inf}$ [Gyr]	$R_{\rm gal}$ [kpc]	$h_{\rm d}$ [pc]
GRASIL	1.55×10^{11}	1.67	4	4.7	400
Our model	1.60×10^{11}	1.90	3	5.0	600

Our modeling parameters in Table 7.1 are determined by hand, so as to reproduce the observed SED. Thus, discussion of the precision of modeling parameter is meaningless, because these parameters do not be derived from the result of best-fitting. The discordance of $M_{\rm gal}$ and $\tau_{\rm SF}$ are caused from the difference of synthesis of stellar emission. In this result, I consider open (infall) model.

Our model reproduce the SED with almost the same physical properties. Our and GRASIL result of the gas fractions are 0.051 and 0.067, the dust masses are 6.7 and 10.4 $\times 10^7$ $M_\odot$, and the SFRs are 4 and 6 $M_\odot$/yr, respectively. Our galaxy volume is larger than GRASIL's one, these values are consistent with estimated value by Beckman et al. (1996). GRASIL consider the radio region emission but our model dose not include that region.

M100

M100 (NGC 4321) is the largest spiral galaxy in the Virgo Cluster, and it is one of the first observed galaxy. The distant is $D = 17.1 \pm 1.8$ Mpc (Freedman et al., 1994) and the inclination angle is $i = 27°$ (Gnedin et al., 1995). The modeling result and parameters are shown in Figure 7.7 and Table 7.2, respectively. Silva et al. (1998) assume the age of the galaxy to be 13 Gyr. Our model and GRAIL calculate the baryonic mass in same value 2.0×10^{11} $M_\odot$, and the gas fraction 0.040 and 0.048, and Young et al. (1989) and Devereux & Young (1990) estimate the fraction in ~ 0.1. Our model and GRASIL derive the SFR 6.5 and 16 $M_\odot$/yr, the radial scale length 6 and 5 kpc, and the vertical scale length is same value

Table 7.2: Modeling parameters of M100

Model	$M_{\rm gal}$ [$M_\odot$]	$\tau_{\rm SF}$ [Gyr]	$\tau_{\rm inf}$ [Gyr]	$R_{\rm gal}$ [kpc]	$h_{\rm d}$ [pc]
GRASIL	2.0×10^{11}	1.3	4	5	400
Our model	2.0×10^{11}	1.1	5	6	400

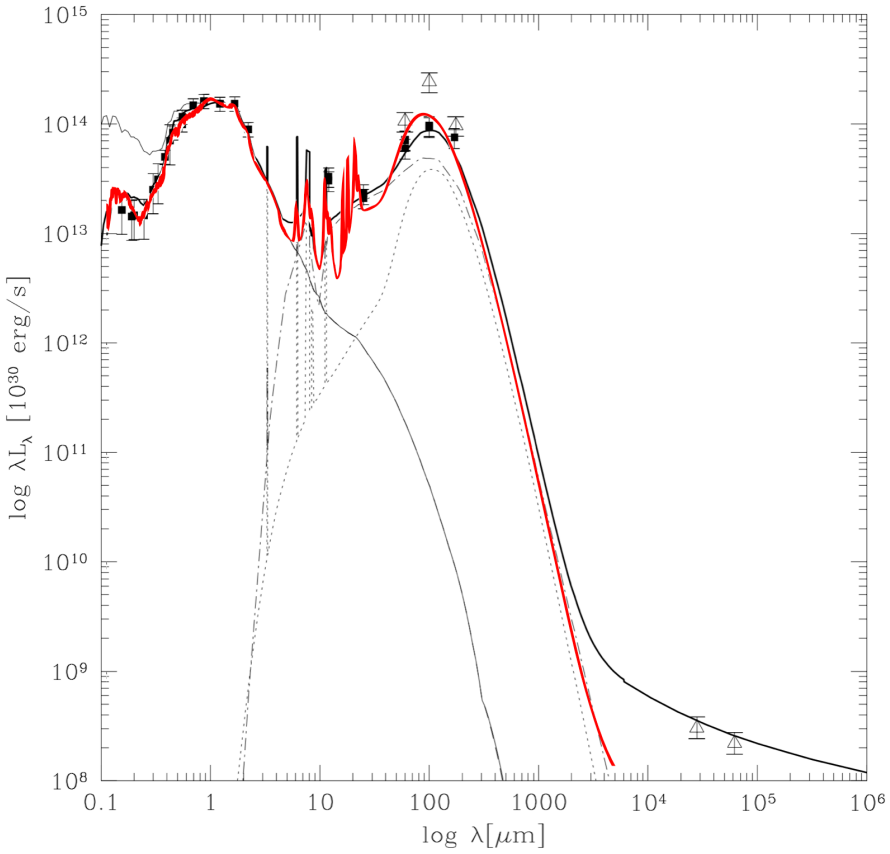

Figure 7.6: The SED of the Sbc galaxy M51 at age of 13 Gyr. The black lines represent fitting result of GRASIL (Silva et al., 1998). The red line shows our model result with parameters listed in Table 7.1. Thin and Thick lines represent unattenuated and attenuated luminosity, respectively. Square symbols are data from Buat et al. (1989), Evans (1995), de Vaucouleurs et al. (1991), Code & Welch (1982), Young et al. (1989), Rice et al. (1988), Devereux & Young (1990), Devereux & Young (1992), and Smith (1982). Triangle symbols represent *ISO* data (Hippelein et al., 1996). Credit: Silva et al. (1998).

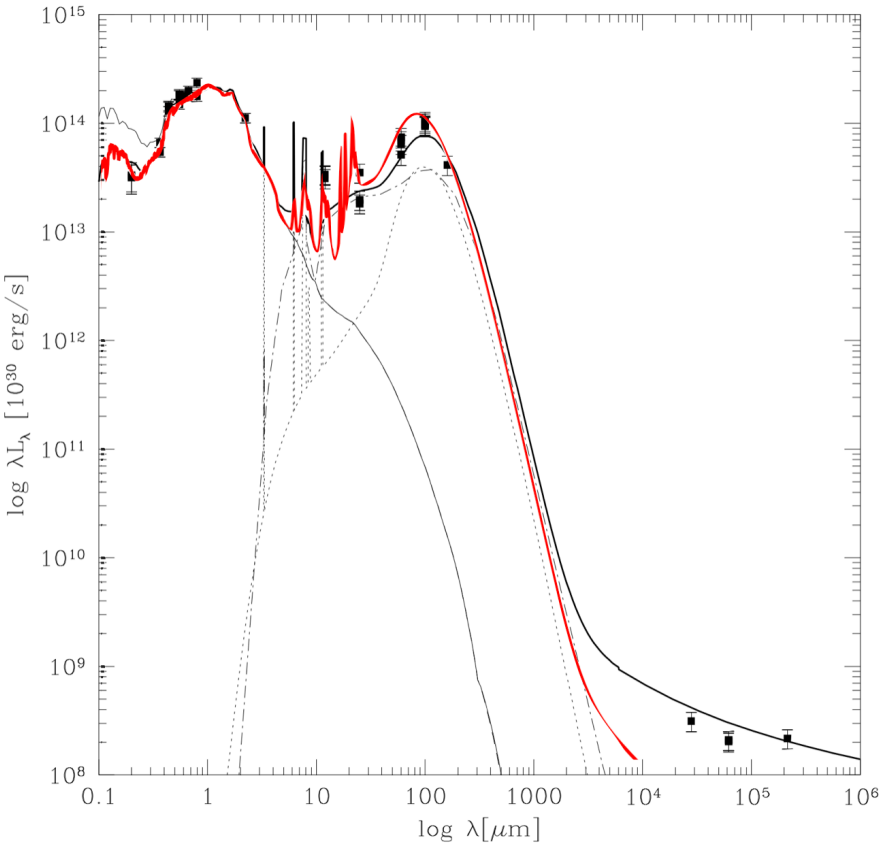

Figure 7.7: The SED of spiral galaxy M100. The black lines represent fitting result of GRASIL (Silva et al., 1998) at the age of 13 Gyr. The red line shows our model result with parameters listed in Table 7.2 at the age of 13 Gyr. Thin and Thick lines represent unattenuated and attenuated luminosity, respectively. Square symbols are data from Buat et al. (1989), Donas et al. (1987), de Jong & van der Kruit (1994), Stark et al. (1989), Devereux & Young (1990), Young et al. (1989), Helou et al. (1988), and Knapp et al. (1987). Credit: Silva et al. (1998).

Table 7.3: Modeling parameters of NGC 6946

Model	$M_{\rm gal}$ [$M_\odot$]	$\tau_{\rm SF}$ [Gyr]	$\tau_{\rm inf}$ [Gyr]	$R_{\rm gal}$ [kpc]	$h_{\rm d}$ [pc]
GRASIL	1.25×10^{11}	1.7	5	8	1000
Our model	1.35×10^{11}	2.0	7	6.5	800

400 pc. These scale lengths are agreement with the values estimated by Beckman et al. (1996).

NGC 6946

The distant of the NGC 6946 is $D = 6.72$ Mpc (Rice et al., 1988) and the inclination angle of the galaxy is $i = 34°$ (Considere & Athanassoula, 1988). The galaxy locate in the boundary between Cepheus and Cygnus. Figure 7.8 shows the GRASIL fitting and our modeling result with the parameters listed in Table 7.3. The

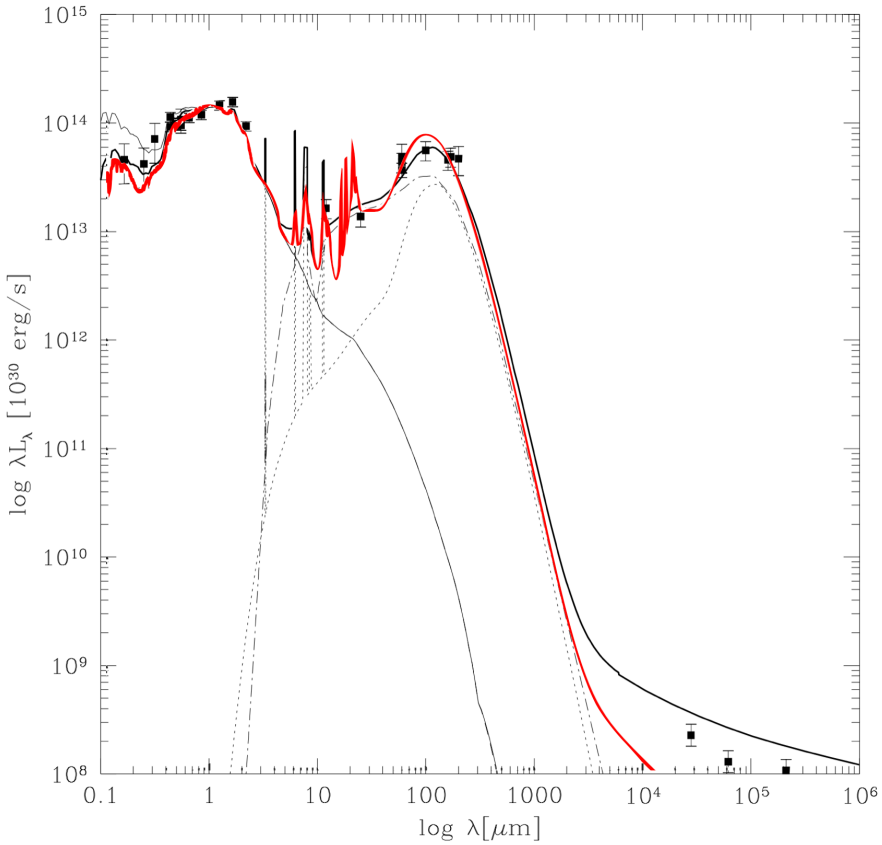

Figure 7.8: The SED of NGC 6946. The black lines represent fitting result of GRASIL (Silva et al., 1998) at the age of 13 Gyr. The red line shows our model result with parameters listed in Table 7.3 at the age of 13 Gyr. Thin and Thick lines represent unattenuated and attenuated luminosity, respectively. Square symbols are data from Rifatto et al. (1995), Engargiola (1991), Devereux & Young (1993), Rice et al. (1988), and Tuffs et al. (1996). Credit: Silva et al. (1998).

assumed ages of the galaxy by GRASIL and our model are 13 Gyr. Our model

calculate larger the baryonic mass than GRASIL. Our model and GRASIL result of the gas masses are 1.31×10^{10} and 1.04×10^{10} $M_{\odot}$, and the fractions of gas are 0.13 and 0.08, Young et al. (1989) and Devereux & Young (1990) estimate the fraction in the same value with us. The SFR of our model is 6.6 $M_{\odot}$/yr and GRASIL is 6 $M_{\odot}$/yr. The radial and vertical scale lengths of our model is smaller than the GRASIL's result, and these values consist with Tacconi et al. (2008).

Chapter 8

Conclusions and future prospects

8.1 Conclusions

In this thesis, we constructed a new galaxy spectral energy distribution (SED) model with the evolution of dust, consistent with the chemical evolution of galaxies, based on Asano et al. (2013a,b, 2014) and Nozawa et al. (2015). Several evolution processes are taken into account in this new model (§4). Dust grains are produced by AGB stars and SNe II, destroyed by SN shocks through sputtering in the ISM. Another process of increasing total dust grain mass is the accretion of metal to the grain surface. This process give a considerable effect on grain mass evolution (e.g., Dwek, 1998; Zhukovska et al., 2008; Draine, 2009; Inoue, 2011). Because of this, a prominent "switching point" of metallicity appears. At this point, the accretion process becomes very efficient. The corresponding galaxy age to the switching point depends on the star formation history as in Figure 4.5 (Asano et al., 2013a). Further, our model considered two types of grain-grain collisions, the shattering and coagulation. The efficiency of these processes are determined by temperature through the grain velocity. Since the high-temperature region easy to occur shattering, a lot of small size grains are produced such a region (§7.1.3).

We calculated the stellar emission by an open source code PÉGASE.2 (Fioc & Rocca-Volmerange, 1997) (§5.1). For fast computation, the radiative transfer is performed in the one-dimensional plain parallel galaxy with the mega-grain approximation (Varosi & Dwek, 1999; Inoue, 2005) (§5.2.1, 5.3). As for the dust emission, we took into account the stochastic heating, and calculated the dust grain temperature distribution function by Monte Carlo simulations (§5.4). The result of Monte Carlo calculation indicated that small grains ($a < 0.4\ \mu$m) have a large temperature dispersion, and large grains have approximately equilibrium temperatures (shown in Figure 5.7-5.9).

Finally, we can see that the galaxy SED (§6) by synthesizing stellar SED (§5.1), dust size distribution (§4), dust attenuation (§5.3), and dust radiation (§5.4). From Figure 6.1, our model could produce a Milky Way-like galaxy (e.g., Figure 6.2), as well as SEDs at any age of the galaxy. Our model indicates that very young galaxies ($\sim$ 100 Myr) produce only a little amount of dust (shown in Figure 6.5). Particularly, the PAH band emissions at MIR wavelengths do not exist in the very early phase of galaxy evolution. When the metallicity exceed 0.1 $Z_{\odot}$, the accre-

tion process becomes suddenly efficient, and an active dust growth is promoted. After that, the emission of the stars and dust grains are decreased with galaxy age. The rapid increase in dust at one age forms the dust attenuation of the MW and nearby galaxies as the galaxy evolution. Conversely, applying the dust distribution assumed from observations of nearby galaxies to distant galaxies without considering the evolution of the dust size distribution causes overestimation of the dust mass. It is expected that this will not happen with our SED model.

8.2 Future prospects

Our model do not include radio emission, because, in normal galaxy, the ratio of the bolometric luminosity in radio region is only $< 10^{-4}$ of the overall bolometric galaxy luminosity (Condon, 1992), and we are interested in the effect of dust grains. Above $\sim$1 mm, radio emission is swamped in dust emission for normal galaxies. Radio is emitted by synchrotron radiation from relativistic electrons accelerated in supernova remnants and free-free emission by HII region (Klein et al., 1988; Carlstrom & Kronberg, 1991). In particular, many galaxies with strong synchrotron radiation by the jet from AGN have been observed (e.g., Carilli et al., 1991; Laing & Bridle, 2002). If we adopt our model to such a radio loud galaxies, we need to include them.

In radiative transfer calculation, we fix the number density of hydrogen, CNM, and WNM. This value is calibrated for MW (Wolfire et al., 2003b). This assumption means the radius of mega-grain in Equation (5.6) is constant. When galaxy has very higher ISM density than the density of MW, our model may underestimate dust attenuation. On the contrary, in low ISM density galaxy case, our model may overestimate the attenuation. For preventing this problem, we will calibrate CNM and WNM density.

Of particular importance is that our model is not yet usable for fitting. This makes it difficult to compare with other models and observational data. All the models introduced in §3.5 can be fitted to the observed data by solving Bayesian parameter inference problem. Our model can calculate radiative transfer at low computational cost thanks to plain parallel galaxy with mega-grain approximation. We will first simply apply a least squares fitting to the code.

References

Abel T., Bryan G. L., Norman M. L., 2002, Science, 295, 93

Alongi M., Bertelli G., Bressan A., Chiosi C., Fagotto F., Greggio L., Nasi E., 1993, A&AS, 97, 851

Alves J., Combes F., Ferrara A., Forveille T., Shore S., 2016, A&A, 594

Anders E., Grevesse N., 1989, Geochim. Cosmochim. Acta, 53, 197

Arendt R. G., et al., 2010, ApJ, 725, 585

Asano R. S., Takeuchi T. T., Hirashita H., Inoue A. K., 2013a, Earth, Planets Sp., 65, 213

Asano R. S., Takeuchi T. T., Hirashita H., Nozawa T., 2013b, MNRAS, 432, 637

Asano R. S., Takeuchi T. T., Hirashita H., Nozawa T., 2014, MNRAS, 440, 134

Auld R., et al., 2013, MNRAS, 428, 1880

Baldry I. K., Glazebrook K., 2003, ApJ, 593, 258

Bastian N., Covey K. R., Meyer M. R., 2010, ARA&A, 48, 339

Beckman J. E., Peletier R. F., Knapen J. H., Corradi R. L. M., Gentet L. J., 1996, ApJ, 467, 175

Bertelli G., Bressan A., Chiosi C., Fagotto F., Nasi E., 1994, A&AS, 106, 275

Bianchi S., Schneider R., 2007, MNRAS, 378, 973

Boquien M., Burgarella D., Roehlly Y., Buat V., Ciesla L., Corre D., Inoue A. K., Salas H., 2019, A&A, 622, 1

Borkowski K. J., Lyerly W. J., Reynolds S. P., 2001, ApJ, 548, 820

Borkowski K. J., et al., 2006, ApJ, 642, L141

Boselli A., Lequeux J., Gavazzi G., 2004, A&A, 428, 409

Boselli A., et al., 2012, A&A, 540, A54

Bressan A., Fagotto F., Bertelli G., Chiosi C., 1993, A&AS, 100, 647

Bressan A., et al., 2006, Proc. IAU, 2, 395

Bromm V., Coppi P. S., Larson R. B., 1999, ApJ, 527, L5

Bromm V., Coppi P. S., Larson R. B., 2002, ApJ, 564, 23

Bronfman L., Cohen R. S., Alvarez H., May J., Thaddeus P., 1988, ApJ, 324, 248

Buat V., Deharveng J. M., Donas J., 1989, A&A, 223, 42

Burgarella D., Buat V., Iglesias-Páramo J., 2005, MNRAS, 360, 1413

Calzetti D., Kinney A. L., Storchi-Bergmann T., 1994, ApJ, 429, 582

Calzetti D., Armus L., Bohlin R. C., Kinney A. L., Koornneef J., Storchi-Bergmann T., 2000, ApJ, 533, 682

Cardillo M., et al., 2014, A&A, 565, 1

Carilli C. L., Perley R. A., Dreher J. W., Leahy J. P., 1991, ApJ, 383, 554

Carlstrom J. E., Kronberg P. P., 1991, ApJ, 366, 422

Cazaux S. M., Caselli P., Walmsley M., Tielens A. G., 2005, Proc. IAU, 1, 325

Chabrier G., 2001, ApJ, 554, 1274

Chabrier G., 2003, PASP, 115, 763

Charlot S., Fall S. M., 2000, ApJ, 539, 718

Chokshi A., Tielens A. G. G. M., Hollenbach D., 1993, ApJ, 407, 806

Ciesla L., et al., 2016, A&A, 585, 1

Clegg R. E. S., Middlemass D., 1987, MNRAS, 228, 759

Clemens D. P., Sanders D. B., Scoville N. Z., 1988, ApJ, 327, 139

Code A. D., Welch G. A., 1982, ApJ, 256, 1

Condon J. J., 1992, ARA&A, 30, 575

Conroy C., 2013, ARA&A, 51, 393

Conselice C. J., Wilkinson A., Duncan K., Mortlock A., 2016, ApJ, 830, 83

Considere S., Athanassoula E., 1988, A&AS, 76, 365

Cordier D., Pietrinferni A., Cassisi S., Salaris M., 2007, AJ, 133, 468

Da Cunha E., Charlot S., Elbaz D., 2008, MNRAS, 388, 1595

Dale D. A., et al., 2017, ApJ, 837, 90

Dame T. M., et al., 1987, ApJ, 322, 706

Davis Leverett J., Greenstein J. L., 1951, ApJ, 114, 206

Dermer C. D., et al., 2013, arXiv e-prints

Desert F. X., Boulanger F., Puget J. L., 1990, A&A, 500, 313

Devereux N. A., Young J. S., 1990, ApJ, 359, 42

Devereux N. A., Young J. S., 1992, AJ, 103, 1536

Devereux N. A., Young J. S., 1993, AJ, 106, 948

Diaz A. I., Terlevich E., Pagel B. E. J., Vilchez J. M., Edmunds M. G., 1987, MNRAS, 226, 19

Dominik C., Tielens A. G. G. M., 1997, ApJ, 480, 647

Donas J., Deharveng J. M., Laget M., Milliard B., Huguenin D., 1987, A&A, 180, 12

Draine B. T., 2003, ARA&A, 41, 241

Draine B. T., 2009, Space Sci. Rev., 143, 333

Draine B. T., Anderson N., 1985, ApJ, 292, 494

Draine B. T., Lee H. M., 1984, ApJ, 285, 89

Draine B. T., Li A., 2001, ApJ, 551, 807

Draine B. T., Li A., 2007, ApJ, 657, 810

Draine B. T., Salpeter E. E., 1977, J. Chem. Phys., 67, 2230

Draine B. T., et al., 2014, ApJ, 780, 172

Drapatz S., Michel K., 1977, A&A, 56, 353

Drude P., 1900a, Ann. Phys., 306, 566

Drude P., 1900b, Ann. Phys., 308, 369

Dwek E., 1998, ApJ, 501, 643

Dwek E., et al., 1997, ApJ, 475, 565

Dwek E., Galliano F., Jones A. P., 2007, ApJ, 662, 927

Engargiola G., 1991, ApJS, 76, 875

Evans A., 1993, The dusty universe. Ellis Horwood Ltd

Evans R., 1995, The Opacity of Spiral Disks. Kluwer Academic Publisher

Fabbiano G., 2006, ARA&A, 44, 323

Fagotto F., Bressan A., Bertelli G., Chiosi C., 1994a, A&AS, 104, 365

Fagotto F., Bressan A., Bertelli G., Chiosi C., 1994b, A&AS, 105, 29

Fagotto F., Bressan A., Bertelli G., Chiosi C., 1994c, A&AS, 105, 39

Ferrarotti A. S., Gail H. P., 2006, A&A, 447, 553

Ferrière K. M., 2001, Rev. Mod. Phys., 73, 1031

Field G. B., Goldsmith D. W., Habing H. J., 1969, ApJ, 155, L149

Fioc M., Rocca-Volmerange B., 1997, A&A, 500, 521

Fioc M., Rocca-Volmerange B., 1999, arXiv e-prints

Fioc M., Rocca-Volmerange B., 2019, A&A, 623, A143

Freedman W. L., et al., 1994, Nature, 371, 757

Fukui Y., Kawamura A., 2010, ARA&A, 48, 547

Gallerani S., et al., 2010, A&A, 523, A85

Gawiser E., et al., 2007, ApJ, 671, 278

Gehrz R. D., 1989, Symp. - Int. Astron. Union, 135, 445

Ginzburg V., Syrovatsky S., 1965, in Int. Cosm. Ray Conf.. p. 53

Girardi L., Bressan A., Chiosi C., Bertelli G., Nasi E., 1996, A&AS, 117, 113

Gnedin O. Y., Goodman J., Frei Z., 1995, AJ, 110, 1105

Granato G. L., Lacey C. G., Silva L., Bressan A., Baugh C. M., Cole S., Frenk C. S., 2000, ApJ, 542, 710

Guelin M., Zylka R., Mezger P. G., Haslam C. G. T., Kreysa E., 1995, A&A, 298, L29

Guhathakurta P., Draine B. T., 1989, ApJ, 345, 230

Guillet V., Pineau Des Forêts G., Jones A. P., 2011, A&A, 527, A123

Hagen A., et al., 2014, ApJ, 786

Hamilton A. J. S., Sarazin C. L., Chevalier R. A., 1983, ApJS, 51, 115

Hayashi C., 1961, PASJ, 13, 450

Hayashi C., 1966, ARA&A, 4, 171

Hayward C. C., Smith D. J. B., 2015, MNRAS, 446, 1512

Heger A., Fryer C. L., Woosley S. E., Langer N., Hartmann D. H., 2003, ApJ, 591, 288

Hellyer B., 1970, Obs., 90, 55

Helou G., Khan I. R., Malek L., Boehmer L., 1988, ApJS, 68, 151

Henyey L. C., Greenstein J. L., 1941, Nature, 147, 613

Henyey L. G., Lelevier R., Levée R. D., 1955, PASP, 67, 154

Hippelein H., et al., 1996, A&A, 315, L79

Hiraki A., Hirak H., 2008, Rev. Mex. Física, 54, 44

Hirashita H., Ferrara A., 2002, MNRAS, 337, 921

Hirashita H., Kuo T. M., 2011, MNRAS, 416, 1340

Hirashita H., Yan H., 2009, MNRAS, 394, 1061

Hirashita H., Nozawa T., Kozasa T., Ishii T. T., Takeuchi T. T., 2005, MNRAS, 357, 1077

Hirashita H., Nozawa T., Takeuchi T. T., Kozasa T., 2008, MNRAS, 384, 1725

Hjorth J., Vreeswijk P. M., Gall C., Watson D., 2013, ApJ, 768, 173

Hobson M. P., Padman R., 1993, MNRAS, 264, 161

Hollenbach D., McKee C. F., 1979, ApJS, 41, 555

Hollenbach D. J., Tielens A. G. G. M., 1997, ARA&A, 35, 179

Hollenbach D. J., Tielens A. G. G. M., 1999, Rev. Mod. Phys., 71, 173

Horn K., Perets H. B., Biham O., 2007, arXiv e-prints

Hu E. M., McMahon R. G., 1996, Nature, 382, 231

Hubble E., 1926, Contrib. from Mt. Wilson Obs. / Carnegie Inst. Washingt., 324, 1

Hunt L. K., et al., 2019, A&A, 621, A51

Iben I., 1985, QJRAS, 26, 1

Inoue A. K., 2003, PASJ, 55, 901

Inoue A. K., 2005, MNRAS, 359, 171

Inoue A. K., 2011, Earth, Planets Sp., 63, 1027

Jones A. P., Tielens A. G. G. M., Hollenbach D. J., McKee C. F., 1994, ApJ, 433, 797

Jones A. P., Tielens A. G. G. M., Hollenbach D. J., 1996, ApJ, 469, 740

Karakas A. I., 2010, MNRAS, 403, 1413

Kaufman M. J., Wolfire M. G., Hollenbach D. J., Luhman M. L., 1999, ApJ, 527, 795

Kennicutt R. C., 1998, ARA&A, 36, 189

Kennicutt R. C., et al., 2011, PASP, 123, 1347

King I. R., 1972, ApJ, 174, L123

Klein U., Wielebinski R., Morsi H. W., 1988, A&A, 190, 41

Knapp G. R., Helou G., Stark A. A., 1987, AJ, 94, 54

Kobayashi C., Umeda H., Nomoto K., Tominaga N., Ohkubo T., 2006, ApJ, 653, 1145

Koyama H., Inutsuka S., 2000, ApJ, 532, 980

Koyama H., Inutsuka S., 2002, in 8th Asian-Pacific Reg. Meet. Vol. II. pp 159–160

Kozasa T., Nozawa T., Tominaga N., Umeda H., Maeda K., Nomoto K., 2009, in Cosm. Dust - Near Far. p. 43

Kroupa P., 2001, MNRAS, 322, 231

Kroupa P., Tout C. A., Gilmore G., 1993, MNRAS, 262, 545

Krugel E., 2003, The physics of interstellar dust. Institute of Physics Publishing

Kuo T. M., Hirashita H., 2012, MNRAS. Lett., 424, 34

Kurucz R. L., 1979, ApJS, 40, 1

Laing R. A., Bridle A. H., 2002, MNRAS, 336, 1161

Laor A., Draine B. T., 1993, ApJ, 402, 441

Laporte N., et al., 2017, ApJ, 837, L21

Larsen S. S., Clausen J. V., Storm J., 2000, A&A, 364, 455

Leitherer C., Li I. H., Calzetti D., Heckman T. M., 2002, ApJS, 140, 303

Lejeune T., Cuisinier F., Buser R., 1997, A&AS, 125, 229

Li A., 2009, Lect. Notes Phys., 758, 167

Li A., Draine B. T., 2001, ApJ, 554, 778

Lisenfeld U., Ferrara A., 1998, ApJ, 496, 145

Maiolino R., Schneider R., Oliva E., Bianchi S., Ferrara A., Mannucci F., Pedani M., Roca Sogorb M., 2004, Nature, 431, 533

Marchenko S. V., 2006, in Stellar Evol. Low Met. Mass Loss, Explos. Cosmol.. p. 299

Mathis J. S., Rumpl W., Nordsieck K. H., 1977, ApJ, 217, 425

McKee C., 1989a, in Interstellar Dust. p. 431

McKee C. F., 1989b, Interstellar Dust, 135, 431

McKee C. F., Ostriker J. P., 1977, ApJ, 218, 148

Mckee C. F., 1974, ApJ, pp 335–339

Mewe R., Lemen J. R., van den Oord G. H. J., 1986, A&AS, 65, 511

Meynet G., Maeder A., 2000, A&A, 361, 101

Michałowski M. J., Murphy E. J., Hjorth J., Watson D., Gall C., Dunlop J. S., 2010a, A&A, 522, A15

Michałowski M. J., Watson D., Hjorth J., 2010b, ApJ, 712, 942

Miller G. E., Scalo J. M., 1979, ApJS, 41, 513

Mo H., van den Bosch F., White S., 2010, Galaxy Formation and Evolution. Cambridge University Press

Morgan H. L., Edmunds M. G., 2003, MNRAS, 343, 427

Myers P. C., 1978, ApJ, 225, 380

Neufeld D. A., 1991, ApJ, 370, L85

Noll S., Burgarella D., Giovannoli E., Buat V., Marcillac D., Muñoz-Mateos J. C., 2009, A&A, 507, 1793

Nomoto K., Tominaga N., Umeda H., Kobayashi C., Maeda K., 2006, Nucl. Phys. A, 777, 424

Nozawa T., Kozasa T., Umeda H., Maeda K., Nomoto K., 2003, ApJ, 598, 785

Nozawa T., Kozasa T., Habe A., 2006, ApJ, 648, 435

Nozawa T., Kozasa T., Habe A., Dwek E., Umeda H., Tominaga N., Maeda K., Nomoto K., 2007, ApJ, 666, 955

Nozawa T., Asano R. S., Hirashita H., Takeuchi T. T., 2015, MNRAS. Lett., 447, L16

Oesch P. A., et al., 2016, ApJ, 819, 129

Ohkubo T., Nomoto K., Umeda H., Yoshida N., Tsuruta S., 2009, ApJ, 706, 1184

Omukai K., Nishi R., 1998, ApJ, 508, 141

Omukai K., Hosokawa T., Yoshida N., 2010, ApJ, 722, 1793

Ostriker J., Silk J., 1973, ApJ, 184, L113

Ouchi M., et al., 2018, PASJ, 70, 1

Palla F., Stahler S. W., 1993, ApJ, 418, 414

Pappalardo C., et al., 2016, A&A, 589, A11

Pascarelle S. M., Windhorst R. A., Keel W. C., Odewahn S. C., 1996, Nature, 383, 45

Pietrinferni A., Cassisi S., Salaris M., Castelli F., 2004, ApJ, 612, 168

Pringle J. E., Rees M. J., Pacholczyk A. G., 1973, A&A, 29, 179

Raiteri C. M., Villata M., Navarro J. F., 1996, A&A, 315, 105

Rice W., Lonsdale C. J., Soifer B. T., Neugebauer G., Kopan E. L., Lloyd L. A., de Jong T., Habing H. J., 1988, ApJS, 68, 91

Rifatto A., Longo G., Capaccioli M., 1995, A&AS, 114, 527

Rubin V. C., Ford Jr. W. K., Thonnard N., 1980, ApJ, 238, 471

Russell H. N., 1914, Pop. Astron., 22, 331

Salpeter E. E., 1955, ApJ, 121, 161

Sandage A., Tammann G. A., 1975, ApJ, 196, 313

Scalo J. M., 1986, Fundam. Cosm. Phys., 11, 1

Scalo J., 1998, in Gilmore G., Howell D., eds, Astronomical Society of the Pacific Conference Series Vol. 142, Stellar Initial Mass Funct. 38th Herstmonceux Conf.. p. 201

Schaller G., Schaerer D., Meynet G., Maeder A., 1992, A&AS, 96, 269

Schmidt M., 1959, ApJ, 129, 243

Schneider R., Ferrara A., Salvaterra R., Omukai K., Bromm V., 2003, Nature, 422, 869

Schneider R., Ferrara A., Salvaterra R., 2004, MNRAS, 351, 1379

Schneider R., Omukai K., Inoue A. K., Ferrara A., 2006, MNRAS, 369, 1437

Schneider R., Omukai K., Bianchi S., Valiante R., 2012, MNRAS, 419, 1566

Shakura N. I., Sunyaev R. A., 1976, MNRAS, 175, 613

Silva L., 2009, in Rev. Mex. Astron. Astrofis. Conf. Ser.. pp 83–93

Silva L., Granato G. L., Bressan A., Danese L., 1998, ApJ, 509, 103

Smith J., 1982, ApJ, 261, 463

Stark A. A., Davidson J. A., Platt S., Harper D. A., Pernic R., Loewenstein R., Engargiola G., Casey S., 1989, ApJ, 337, 650

Tacconi L. J., et al., 2008, ApJ, 680, 246

Takeuchi T. T., Hirashita H., Ishii T. T., Hunt L. K., Ferrara A., 2003, MNRAS, 343, 839

Takeuchi T. T., Ishii T. T., Nozawa T., Kozasa T., Hirashita H., 2005, MNRAS, 362, 592

Tamura Y., et al., 2019, ApJ, 874, 27

Todini P., Ferrara A., 2001, MNRAS, 325, 726

Tuffs R. J., et al., 1996, A&A, 315, L149

Tully R. B., 1974, ApJS, 27, 437

Tumlinson J., Peeples M. S., Werk J. K., 2017, ARA&A, 55, 389

Valiante R., Schneider R., Bianchi S., Andersen A. C., 2009, MNRAS, 397, 1661

Varosi F., Dwek E., 1999, ApJ, 523, 265

Ward-Thompson D., Whitworth A. P., 2011, An Introduction to Star Formation. Cambridge University Press

Watson D., Christensen L., Knudsen K. K., Richard J., Gallazzi A., Michałowski M. J., 2015, Nature, 519, 327

Weingartner J., Draine B., 2001, ApJ, 548, 296

Whittet D. C. B., 2003, Dust Galact. Environ.

Whitworth A. P., Boffin H. M. J., Francis N., 1998, MNRAS, 299, 554

Wild W., Harris A. I., Eckart A., Genzel R., Graf U. U., Jackson J. M., Russell A. P. G., Stutzki J., 1992, A&A, 265, 447

Winters J. M., Fleischer A. J., Le Bertre T., Sedlmayr E., 1997, A&A, 326, 305

Wolfe A. M., Gawiser E., Prochaska J. X., 2005, ARA&A, 43, 861

Wolfire M. G., McKee C. F., Hollenbach D., Tielens A. G. G. M., 2003a, ApJ, 587, 278

Wolfire M. G., McKee C. F., Hollenbach D., Tielens A. G. G. M., 2003b, ApJ, 587, 278

Yamasawa D., Habe A., Kozasa T., Nozawa T., Hirashita H., Umeda H., Nomoto K., 2011, ApJ, 735

Yan H., Lazarian A., Draine B. T., 2004, ApJ, 616, 895

Yasuda Y., Kozasa T., 2012, ApJ, 745, 159

Yoshida N., Omukai K., Hernquist L., 2008, Science, 321, 669

Young J. S., Scoville N. Z., 1991, ARA&A, 29, 581

Young J. S., Xie S., Kenney J. D. P., Rice W. L., 1989, ApJS, 70, 699

Zhukovska S., Gail H. P., Trieloff M., 2008, A&A, 479, 453

Zibetti S., Charlot S., Rix H. W., 2009, MNRAS, 400, 1181

de Jong R. S., van der Kruit P. C., 1994, A&AS, 106, 451

de Vaucouleurs G., 1959, Handb. der Phys., 53, 275

de Vaucouleurs G., de Vaucouleurs A., Corwin Jr. H. G., Buta R. J., Paturel G., Fouque P., 1991, Third Reference Catalogue of Bright Galaxies. Springer